A Numerical Study of the Stefan Problem with an Application to the Growth of Crystalline Microstructure

Stuart J. Galloway

Doctor of Philosophy
University of Edinburgh
1998

To the memory of my father,
James S. Galloway
(1934 – 1984)

Abstract

The numerical solution of well-posed Stefan problems in a two-dimensional region are considered using a boundary integral technique. The numerical method is an extension of that used in previous work in that the boundary integral formulation takes account of heat flow both ahead of and behind the phase change front. This allows more realistic problems to be considered. Furthermore, it is found that when parameter values appropriate for water are used, the previously applied routine, based on Newton's method, for determining the location of the phase change front, is unstable. This is overcome by using a bisection based method for these parameter values. This numerical formulation is found to have a number of advantages over finite difference and finite element techniques. For example, complex boundaries can be easily considered and the discretisation of the Stefan condition is not required. Numerical solutions of the Stefan problem are found for different parameter values and, more specifically, the freezing of water is considered. Employing a model of crystal formation, the numerical method is applied to predict the size of the crystals in the crystalline microstructure that is formed when a material freezes. The predictions of this model are compared against experimental results and it is found that they are in good qualitative agreement.

To obtain a more accurate model of the freezing of a liquid, the numerical method is extended to include the fluid motion in the closed region ahead of the phase change front. A numerical procedure is outlined for dealing with genuine two-phase problems, using a different approach in each phase. The fluid flow problem in the liquid phase of the material is solved using a time dependent finite difference method on a non-uniform mesh, whereas the previously derived boundary integral method is used to determine the temperature distribution in the solid phase. The numerical scheme in the liquid phase is found to be second order in space and time. An examination of the freezing of water is again undertaken and the size of the crystals formed within the freezing liquid is predicted using the model for crystal growth. Comparison with previous calculations without fluid flow confirms that the fluid motion has a significant effect on the overall freezing process and upon the crystal size.

Acknowledgements

Firstly I would like to express my gratitude to my supervisor Dr. Noel F. Smyth for introducing me to Stefan problems and without whose advice and enthusiasm this work would not have been possible.

I also owe a great debt to my mother, Maureen, for her support and encouragement over the years and for her tolerance and patience over recent months.

I would like to thank Catriona Fisher for her continued moral support throughout the duration of this work and, of course, for the attempted proof read.

Thanks are due to the staff and students of the Mathematics and Statistics department for providing a stimulating and friendly working environment. In particular I would like to thank Gordon J. Darling and J. Stuart MacIntosh who I consider not only valued colleagues but firm friends.

The following people are owed my thanks and appreciation for reasons that are too diverse to mention: Sheila Adamson, Dr. Tobias Boettcher, Gordon Collins, Dr. Zhanfeng Cui, Andrew Door, John Galloway, David Gibson, Philip McCabe, Bob McCalister, Andrew Nex, Iris O'Brien, Prof. David F. Parker, Dr. Weidong Peng, Frank Plab, Robert Robertson and Jenny Rudd.

The financial support of the EPSRC for funding an earmarked studentship award is also acknowledged.

Table of Contents

Chapter 1

Introduction

1.1 The Boundary Integral Approach To Stefan Problems

Situations in which a material undergoes a change of phase are widespread in science, engineering and industry. Industrial applications range from the processing of metals to food processing to blood plasma storage. For example, solidification of steel, freezing and thawing of biological material and the production of ice all involve a moving boundary. Mathematically moving boundary problems which involve heat conduction are associated with Josef Stefan (1835-1893) and as such are often referred to as Stefan problems. Although such problems were certainly being considered by Gabriel Lamé (1795-1870) and Benoit Clapeyron (1799-1864) as early as 1831. In 1889 Stefan published four papers involving a moving boundary whose motion had to be determined. In the first of these papers [52] he considered a one-dimensional material lying in the semi-infinite half space $0 \leq x \leq \infty$ that can exist in either a solid or liquid phase. Initially the material was taken to be in the liquid phase at a known uniform temperature. At time $t = 0$ the surface $x = 0$ was cooled to a temperature below that of the fusion temperature of the liquid and maintained at this level thereafter. Instantaneously a moving boundary begins to propagate through the material from $x = 0$. Ahead of the moving boundary the material is in the liquid phase and behind is in the solid phase. At some time $t > 0$ the problem therefore is to determine the thickness of the solid region and to find the temperatures of both phases. The complete solution is discussed in detail by Carslaw & Jaeger [7]. Other questions can often arise about the properties of each phase but in general these are problem dependent e.g. segregation of species [13, 16].

At the phase change front there is a discontinuous jump in the heat flux. This jump is modelled by a conservation of energy relation, called the Stefan condition,

which in one-dimension is given by

$$K_s \frac{\partial T_s(\hat{x}(t),t)}{\partial x} - K_l \frac{\partial T_l(\hat{x}(t),t)}{\partial x} = \rho L \frac{d\hat{x}}{dt}. \tag{1.1}$$

Here T_s, T_l, K_s and K_l are the temperatures and thermal conductivities of the solid and liquid phases respectively. The phase change front at some time $t > 0$ is located at $x = \hat{x}(t)$ and the Stefan condition states that the phase change front moves in such a way that its velocity is proportional to the jump in heat flux across the front. This heat flux is due to the release of the latent heat which is liberated at the moving boundary upon freezing. While the equations governing the phase change of a material are well understood, namely the heat equation in the two phases plus an energy conservation condition at the phase change front, the so-called Stefan condition, there are very few exact solutions of these equations outside of one-dimensional situations (see for example Carslaw & Jaeger [7] and Crank [16]). The paucity of exact solutions is due to the position of the phase change front being both unknown and influenced by the temperature fields in the two phases. The details of a two- or three-dimensional material undergoing a phase change can, therefore, in general, only be calculated using numerical methods. Numerical schemes that are used to calculate solutions of Stefan problems must be chosen with care so that unphysical oscillations in the temperature field are not introduced at the phase change front. These oscillations are due to the discontinuous temperature derivative at the front.

Successful numerical methods used to solve phase change problems must therefore include a way to accommodate the discontinuous temperature derivative at the phase change front. A number of these numerical methods are discussed in Crank [16] and in the articles by Fox [26] and Voller *et al.* [55]. One such technique is the so-called front tracking method [16]. This method requires that for each time step the position of the moving boundary be calculated. The solution is computed on a fixed grid in space-time so that, in general, the moving boundary at some time $t > 0$ will lie between grid points. Therefore close to the moving boundary special formulations of the governing partial differential equations and Stefan condition are required. These formulations lead to formulae which allow for unequally spaced intervals on the grid. An alternative is to transform the grid itself in some way so that the moving boundary lies on a grid line or is fixed in the transformed domain.

The front tracking method can be modified to accommodate a variable time step and/or a variable space step; see Crank [16]. Variable space steps are used to avoid the increase in computational effort and loss of accuracy associated with unequal space intervals near the moving boundary. In methods which employ a

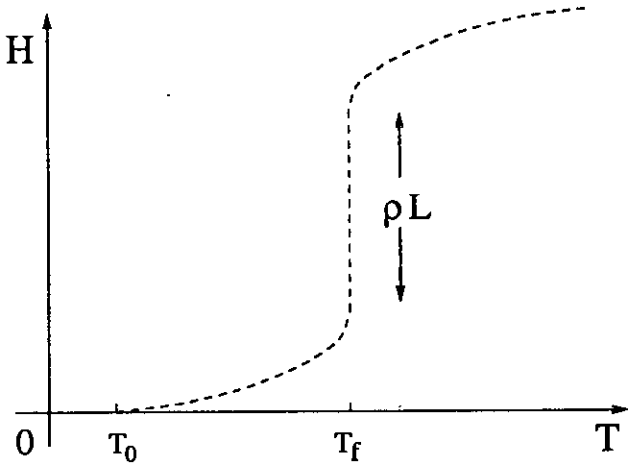

Figure 1.1: The enthalpy $H(T)$

variable time step, the time step at a given time is determined so that the moving boundary coincides with a grid line at each time. The variable space step method can also be used to keep the number of grid points in the region constant by redistributing the grid points each time the front is moved. Interpolation from the previous grid points is used to evaluate the temperature at the new grid points where necessary. An extensive survey of front tracking methods can be found in Crank [16].

Difficulties with the use of front tracking methods can arise when the moving boundary does not evolve regularly, for example if it were to double back on itself or disappear temporarily. This can lead to numerical difficulties in the discretisation of the Stefan condition and the governing partial differential equations at the phase change front. The possibility, therefore, of reformulating the problem in such a way that the Stefan condition is implicitly bound up in the new form of the equations which then apply over the whole region is attractive. The enthalpy method [16, 23, 24, 30, 31, 54, 55], which solves for the total heat content, avoids the difficulties of front tracking methods since the discontinuity in the temperature derivative is by-passed by solving for the enthalpy instead of the temperature. This is achieved by defining an enthalpy function $H(T)$, which is the total energy content, i.e. the sum of the specific and the latent heat required for a phase change to take place. The enthalpy is defined by

$$H(T) = \int_{T_0}^{T} \left[\rho(\theta)\, c(\theta) + L\, \rho(\theta)\, \delta(\theta - T_f)\right] d\theta, \tag{1.2}$$

where $\rho(T)$ is the density, $c(T)$ is the specific heat and $\delta(x)$ is the Dirac delta function. Furthermore T_0 is a reference temperature less than the freezing temperature T_f. The form of $H(T)$ is shown graphically in figure 1.1. The jump in heat content at the moving phase change front is incorporated in the defini-

tion of $H(T)$. The heat conduction problem can then be reformulated over the whole region containing the two phases, except where $T = T_f$, and is described in one-dimension by the single equation

$$\frac{\partial H(T)}{\partial t} = \frac{\partial}{\partial x}\left(K(T)\frac{\partial T}{\partial x}\right) \tag{1.3}$$

or in higher dimensions by

$$\frac{\partial H(T)}{\partial t} = \underline{\nabla}\cdot(K(T)\underline{\nabla}T) \tag{1.4}$$

together with associated boundary and initial conditions. The thermal conductivity $K(T)$ is a function of temperature and is given by

$$K(T) = \begin{cases} K_s & \text{if } T < T_f \\ K_l & \text{if } T > T_f \end{cases} . \tag{1.5}$$

The moving boundary is located by simple inspection of the solution across the computational mesh to locate the jump in enthalpy. The enthalpy method and its numerical implementation is discussed by Elliott *et al.* [23] and Crank [16], in the review article on finite element and finite volume methods for Stefan problems by Voller *et al.* [55] and in the book on the numerical solution of moving boundary problems by Finlayson [24].

Finite difference methods based on the enthalpy method work well for rectangular regions (see Voller [54]), but are difficult to apply when the domain is not rectangular. Finite element methods can be used to overcome this drawback, see Voller, Swaminathan and Thomas [55], Finlayson [24], Lynch [36] and Chow [9].

As an alternative to finite element methods, Coleman [12] used a boundary integral method to find numerical solutions for phase change problems for which the temperature ahead of the phase change front was kept constant at the fusion temperature. The integral equation describing the temperature distribution in the solid phase behind the phase change front,

$$\begin{aligned} -\lambda T_s(\mathbf{r},t) \;=\; & D_s\int_0^{t+0}\int_{B_f}\left(T_s'\frac{\partial G_s}{\partial n'} - G_s\frac{\partial T_s'}{\partial n'}\right)ds'dt' \\ & -D_s\int_{B_s} G_s(\mathbf{r},\mathbf{r}',t,f(x',y'))\,dx'\,dy' , \end{aligned} \tag{1.6}$$

was obtained from the governing equation of heat flow, the heat equation, by utilising a Green's function formulation of the problem; see Carslaw & Jaeger [7], Crank [16] and Hill and Dewynne [30]. Here D_s is the thermal diffusivity of the solid, G_s is an appropriate Green's function for the solid phase and $f(x,y)$ is the position of the phase change front. In the above equation we have assumed that the temperature on the phase change front is $T_s(x,y,t) = 0$ which by the implicit

function theorem has the unique solution $t = f(x, y)$. The boundaries B_f and B_s are the fixed and moving boundary respectively, with $\underline{n}$ the outward unit normal to the fixed boundary B_f. Full details for each of the terms and coefficients in the integral equation will be given in Chapter 3.

This method has the great advantage in that it can be easily applied to regions of any shape and, furthermore, the Stefan condition is fitted naturally into the numerical scheme without discretisation. The boundary integral method also results in a great reduction in computational effort as it reduces the problem of solving for the temperature field in the two phases to solving for unknowns on the boundary of the material and on the phase change front only. Thus a two-dimensional problem is reduced to a one-dimensional problem on two curves, with a resulting great saving in calculation.

Coleman [12] applied his boundary integral method to solving phase change problems on square and L-shaped regions and it was found to give fast, accurate results in good agreement with other methods. The boundary integral method does however have the drawback that it can only be applied to well-posed Stefan problems and not to supercooled situations, unlike the enthalpy method which can be applied in both cases [55].

In Chapter 2 of the present work we shall begin by considering the one-dimensional problem posed by Stefan [52], that of a plane phase change front propagating through a material that can exist in either a solid or liquid phase. For a fixed temperature boundary condition this relatively simple problem yields an exact solution in one-dimension [30] and provides a useful starting point for higher dimensional problems. Furthermore, the solution of the one-dimensional problem will be used as part of the start-up procedure for the numerical solution of two-dimensional problems.

In Chapter 3 the boundary integral method of Coleman [12] will be extended in two ways. Firstly the boundary integral formulation will be extended to include heat flow ahead of the phase change front, so that more general and realistic initial conditions can be used. Further, Coleman [12] used Newton's method to find the position of the phase change front. It is found that for the freezing of a liquid for which the ratio of the thermal diffusivity of the liquid phase to the thermal diffusivity of the solid phase is large, Newton's method converges slowly due to small temperature derivatives at the phase change front. The numerical method developed in the present work overcomes this by using a bisection method to determine the position of the phase change front when Newton's method converges slowly. By symmetry, Newton's method will also converge slowly for a melting problem for which the ratio of the thermal diffusivities of the liquid phase to the

solid phase is small.

Including the heat flow ahead of the phase change front means that the temperature in the liquid phase is no longer constant. Instead the temperature distributions in both the solid and liquid phases need to be calculated as part of the solution process. In the solid phase behind the phase change front the integral equation that needs to be solved to determine the temperature field has the same structure as the integral equation (1.6) of Coleman [12], with the final integral term on the right hand side replaced by

$$-D_s \int_{B_s} G_s(\mathbf{r}, \mathbf{r}', t, f(x', y'))\, \nabla' T_s' \cdot \nabla' f|_{t'=f(x',y')}\, dx'\, dy'\,. \tag{1.7}$$

This different term is due to the temperature gradient of the liquid, $\nabla' T_l'$, not being zero at the phase change front. In the liquid phase ahead of the phase change front, the integral equation for the temperature field

$$\begin{aligned} -\lambda T_l(\mathbf{r}, t) \;=\; & -\int_{S_0} T_l'(\mathbf{r}', 0)\, G_l(\mathbf{r}, \mathbf{r}', t, 0)\, dx'\, dy' \\ & + \int_{B_s} G_l(\mathbf{r}, \mathbf{r}', t, f(x', y'))\, \nabla' T_l' \cdot \nabla' f|_{t'=f(x',y')}\, dx'\, dy' \end{aligned} \tag{1.8}$$

is obtained by a similar application of the Green's function formulation of the governing equation of heat flow for the liquid phase. Here G_l is an appropriate Green's function for the liquid phase and the boundary S_0 is the initial position of the moving boundary at time $t = 0$. At the moving phase change front these integral equations are linked by the Stefan condition (1.1), from which the relationship

$$K\, \nabla' T_s' \cdot \nabla' f = S_t + \nabla' T_l' \cdot \nabla' f, \tag{1.9}$$

is obtained. Here S_t is the Stefan number – the ratio of latent heat to the sensible heat required for a phase change. These integral equations together with the Stefan condition, completely determine the temperature field within the material and the position of the phase change front.

A detailed derivation of the integral equations for genuine two-phase Stefan problems will be presented in Chapter 3. Furthermore, a full account of the numerical scheme used to solve the integral equations, together with its implementation, is given in that chapter. Results obtained using the numerical scheme will be compared with the results of Coleman [12] for single phase Stefan problems for the purpose of the validation of the numerical method presented here. The boundary integral method will be applied to a number of examples of the freezing of a rectangular region for which the temperature ahead of the phase change front is higher than the freezing temperature of the liquid. Emphasis will be placed on the freezing of water, with parameter values chosen to be those appropriate for water.

The growth of crystals formed when a material freezes can have a significant effect on the properties of the material once it is thawed; see Fletcher [25]. For example, in the freezing of protein solutions the control of crystal structure and size is of great importance as the formation of large crystals can lead to damage of the proteins at molecular level; see Miyawaki *et al.* [37]. Empirically it is known that slow freezing leads to large crystal sizes while rapid freezing produces a fine structure with small crystals. In general, the structure and sizes of the crystals formed are determined by the properties of the material to be frozen and the operating conditions at freezing. An application of the numerical method is made to predict the sizes of crystals formed when a material freezes, based on a simple model of crystal growth by Frank [27] and Coriell and McFadden [15]. The predictions of this model are compared with experimental results and good qualitative agreement is found.

The main results discussed in this section form Chapters 2 and 3 of this thesis and are presented in the paper by Galloway & Smyth [28].

1.2 Fluid Motion in Stefan Problems

In the second part of this thesis the fluid motion in the closed region ahead of the phase change front will be included to provide a more realistic and accurate model of the freezing of a liquid. This will further extend the work of Coleman [12] and that of Chapter 3 to include fluid motion in the numerical solution of two-phase Stefan problems. When fluid motion is included heat transport is not only driven by diffusion, but also by buoyancy induced thermal convection. The geometry and orientation with respect to gravity can also play an important roll in determining the heat transport in the fluid. However thermal convection is often the driving force and by its nature allows hot fluid to circulate to the phase change front, so that heat will be drawn out of the liquid phase more rapidly than if no fluid motion occurred. Thus including the fluid motion ahead of the phase change front, in the liquid phase, will provide a more realistic model of the freezing process.

The first quantitative experiments of thermally induced convection were made by Henri Bénard [4] in 1900. In these experiments he considered very thin layers of fluid lying on a metallic dish. The lower side of the dish was maintained at some uniform temperature with the upper surface free and at a lower temperature due to its exposure to air. The layer of fluid in these experiments was observed to form a cellular pattern; see figure 1.2. Lord Rayleigh explained this phenomena in terms of a buoyancy driven instability by a linear expansion of the equations

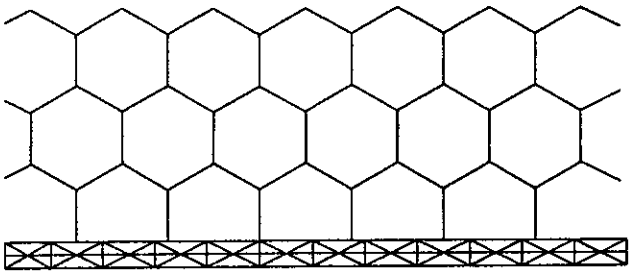

Figure 1.2: Hexagonal Bénard cells at equilibrium

written in terms of the fluid velocities about the rest state of no fluid motion [46]. It was later determined analytically and experimentally that in buoyancy driven convection the expected pattern would be stripes or convection rolls, rather than the cells observed by Bénard [22], which is a nonlinear phenomena. Pictures of stripes, rolls and cells for modern reproductions of Bénard's experiment are shown in Van Dyke [53].

The convective motion that leads to this pattern formation is explained by Drazin & Reid [22] in the following manner. Heating the lower side of the region creates a region of hotter and, in general, less dense fluid lying below a region of cooler, denser fluid. When the temperature difference across the layer is great enough, the stabilizing effects of viscosity and thermal conductivity are overcome by the destabilizing buoyancy and an overturning instability ensures thermal convection. In general problems involving convection in a fluid layer heated from below are called Bénard or Rayleigh-Bénard convection problems [22, 58].

In the present work we shall consider the motion of a fluid in a closed region that is bounded by a moving boundary. At some time $t > 0$ the region R, which includes both the solid and liquid phases, consists of two boundaries, one of which is fixed and the other of which is moving; see figure 1.3. Ahead of the moving boundary the fluid is taken to be at a temperature greater than its fusion temperature and consequently in the liquid phase. Behind the moving boundary the fluid is at a temperature less than the fusion temperature and so is in the solid phase. In the cases to be considered in the present work the fluid is cooled uniformly around its boundary, creating a layer of cooler more dense fluid which lies around a region of hotter, less dense fluid. In the same way as with the classical Bénard problem we have a denser fluid overlaying a less denser fluid. The less dense fluid in the centre of the region will then, if the temperature difference between this fluid and the fluid at the phase change front is great enough, rise to displace the layer of denser, colder fluid that lies on the inside of

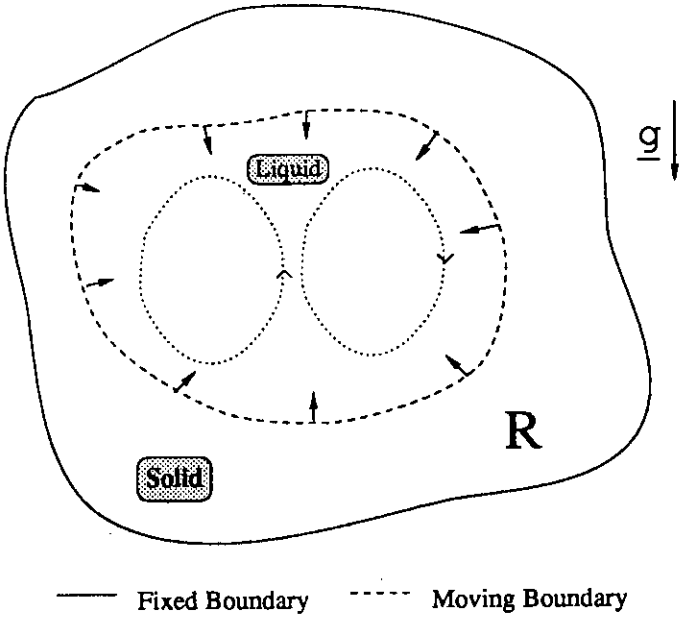

Figure 1.3: Region R with two convection cells in the liquid phase

the phase change front. As the less dense fluid rises and reaches the colder layer, close to the phase change front, it will be itself cooled to a denser fluid and begin to fall. In this way the fluid begins to circulate, leading to thermal convection occurring in the liquid phase ahead of the phase change front; see figure 1.3. In the present work we shall be specifically concerned with the freezing of water. For a detailed discussion of the physical and chemical properties of water see Fletcher [25] and Sienko & Plane [50]. Water has the unusual property that it attains its maximum density at about $4\,^{\circ}C$ and above $4\,^{\circ}C$ the density of water is a decreasing function of temperature. For initial temperatures greater than $4\,^{\circ}C$ the onset of thermal convection is attained by the process described above. In the range $0\,^{\circ}C$ to $4\,^{\circ}C$ however, the colder the water, the less dense it becomes. Hence for the classic Bénard convection problem the rest state will remain stable, with the hot fluid region unable to penetrate the region of colder fluid. For water temperatures between $0^{\circ}C$ and $4^{\circ}C$ the fluid in the internal region ahead of the phase change front will be more dense than the cooler fluid residing in the layer immediately ahead of the phase change front. With the existence of sufficiently large temperature differences between the centre and the phase change front, the density difference will cause circulation of the fluid due to buoyancy induced thermal convection. The cooler, less dense liquid at the bottom of the region will be forced upwards by the descent of hotter, more dense liquid above it. As in all induced thermal convection problems the fluid circulation will continue until temperature variations throughout the liquid phase are sufficiently small.

In Chapter 4 the governing equations of fluid motion are stated in the vorticity-streamfunction formulation of the Navier-Stokes equation together with the convection-diffusion equation; see Batchelor [3]. The fluid is assumed to a Boussinesq fluid. This approximation is valid when the temperature, and therefore density, variations are small and assumes that the density variations are only significant in the buoyancy terms of the Navier-Stokes equation. In terms of non-dimensional variables the governing equations of fluid flow are the convection-diffusion equation

$$\frac{\partial T_l}{\partial t} = -\nabla \cdot (T_l \underline{u}) + D_l \nabla^2 T_l, \tag{1.10}$$

the Helmholtz vorticity equation

$$\frac{\partial \omega}{\partial t} = -\nabla \cdot (\omega \underline{u}) - \frac{\partial T_l}{\partial x} + \nu_l \nabla^2 \omega \tag{1.11}$$

and the streamfunction equation

$$\nabla^2 \psi = -\omega. \tag{1.12}$$

In these equations, $\underline{u}$ is the fluid velocity, ω is the vorticity, T_l is the temperature of the liquid region and ψ is the streamfunction. Here the coefficient D_l is the thermal diffusivity and ν_l is the kinematic viscosity. A detailed derivation of these equations together with suitable non-dimensional scalings and appropriate boundary and initial conditions will be presented in Chapter 4. Also in that chapter the boundary integral method of Coleman [12] will be further extended to include the fluid motion in the liquid region ahead of the phase change front. A full account of the numerical scheme used to solve genuine two-phase Stefan problems with fluid motion in the liquid phase, together with its implementation, is given. In the solid phase behind the phase change front, the boundary integral method of Coleman [12] is used to solve for the temperature field. In the liquid phase the solution of the equations of fluid motion, namely (1.10) to (1.12), is required. As in Chapter 3 the Stefan condition provides a link between the two phase change regions in the form of the relationship

$$\nabla' T_s' \cdot \nabla' f = S_t + \nabla' T_l' \cdot \nabla' f, \tag{1.13}$$

where S_t is the non-dimensional Stefan number.

Due to the complexity of the fluid motion equations and the domain in which they are solved, a numerical method is required for their solution. A number of such methods are discussed in the book by Shyy *et al.* [49] and in the review articles by de Vahl Davis [20] and Ostrach [43]. The problem in this case, as well

as in the case of no fluid motion, is that any numerical procedure for solving the governing equations must also cope the location of the moving boundary as part of the solution process. Therefore many of the techniques used to solve fluid flow problems in the presence of a moving boundary overlap with the solution techniques for the moving boundary problems themselves [49]. For example, a moving grid can be utilised that travels with the moving boundary itself. The moving boundary is explicitly tracked at each time step, with the individual domain at each time step being obtained by some sort of front fitted coordinate system. The governing equations are transformed to this front fitted domain and are solved in the new coordinates by a standard solution technique e.g. finite differences [20, 21, 57] or finite elements [8, 19, 33, 42]. The mesh is then redistributed to conform with the new shape of the moving boundary and the solution procedure repeated. This solution technique is similar in construction to the front tracking methods described previously (Crank [16]). Yeoh *et al.* [57] and de Vahl Davis *et al.* [21] have used this technique to study natural convection in two- and three-dimensional regions. The governing equations are transformed into a square or cubical domain and then solved using a finite difference scheme. The authors have shown that this method gives good agreement with experimental results for the freezing of water. This technique can encounter difficulties if the moving boundary should become concave or if the moving boundary should become very distorted as extensive regridding can become costly computationally.

Similarly fixed grid methods provide another technique for convection problems with a moving boundary, see Shyy *et al.* [49]. In heat transfer terms, one of the most well known methods is the enthalpy method; see Crank [16]. In this approach the moving boundary is tracked implicitly and the governing equations are reformulated in terms of the total enthalpy. These transformed equations can then be solved by standard solution techniques without the need to transform the domain or manipulate the equations. The phase change front is located by searching for the change in enthalpy across the grid. Furthermore the enthalpy method can cope with problems where the transition between different phases takes place over a finite interval rather than at a discontinuity. Brent *et al.* [5] have successfully applied the enthalpy technique to a range of problems where the material, in this case gallium, changes phase over a finite interval. This interval is sometimes called the mushy zone. The authors have shown that their method gives good agreement with experimental results.

To accommodate the moving boundary with the governing equations of fluid flow we shall use a finite difference scheme that is applied on a non-uniform spatial mesh ahead of the phase change front in the liquid phase. The finite difference

scheme is based on the formulation given by Moore *et al.* [38]. In this work the equations were solved on a staggered mesh, which reduces the computation and storage requirements of the method. However this staggered mesh requires a uniform spacing of the mesh points which, due to the moving boundary, is not possible for the problems considered in Chapter 4. Instead the strategy employed is to retain mesh points which fall ahead of or on the moving boundary and discard the points that lie behind. The remaining mesh is then extended, if required, to include points on the phase change front. In this way the spatial grid is reduced at each time step, which provides a great computational saving as the phase change front advances. A validation of the finite difference scheme is obtained by a comparison with the solutions of the classical Bénard convection problem considered by Moore *et al.* [38]. The fluid equations are solved until steady convection is reached and this steady flow is found to compare favourably with the results of Moore *et al.* [38].

In the derivation of the above fluid equations (1.10) to (1.12) it was assumed that the fluid density depended linearly on temperature. For water however the relationship between density and temperature is approximately quadratic, with a maximum density at $3.98\,^{\circ}C$; see Sienko & Plane [50]. This results in a revised form of the equations governing the fluid flow. Under suitable scalings the Helmholtz vorticity equation is now

$$\frac{\partial \omega}{\partial t} = -\nabla \cdot (\omega\, \underline{u}) - \frac{\partial}{\partial x}\,(T_l - T_{l_r})^2 + \nu_l \nabla^2 \omega\,, \tag{1.14}$$

where the temperature T_{l_r} is the non-dimensional temperature at which the water density is at its maximum. The convection-diffusion equation (1.10) and the streamfunction equation (1.12) are the same as before. However the non-dimensional coefficients are changed to those appropriate for water.

In the present work a detailed study is made of two-phase Stefan problems for the freezing of water which includes convection in the liquid phase. A number of different initial temperatures above the fusion temperature ($\tilde{T}_{l_f} = 0\,^{\circ}C$) are treated, including an example with initial temperature close to $4\,^{\circ}C$, where water attains its maximum density. Furthermore the crystal size model of Chapter 3 is extended so that the effect of fluid flow on the size of ice crystals can be determined. The mean crystal sizes are then compared with the results for no convection considered in Chapter 3. The inclusion of convection in the liquid phase ahead of the phase change front is shown to have a significant effect on the size of the crystals produced when water is frozen, with crystal size being significantly reduced, as would be expected.

Finally in Chapter 5 some conclusions on the work are drawn. The choice of

numerical strategy employed is discussed and improvements, where necessary, are suggested. Some points are also raised on the limitations of the adopted numerical method in terms of its applicability to different geometries, well-posed and supercooled/superheated problems. Some aspects of the computer programming itself will also be raised, including a brief discussion on parallelisation.

Chapter 2

The One-Dimensional Problem

2.1 The Stefan Problem

Moving boundary problems can arise in a variety of physical and mathematical contexts. One such area is when a change of state or phase occurs. The phase change problem is an area of extensive research in applied mathematics. There are few exact solutions of moving boundary problems, and consequently much research has focused on approximate and numerical means of solution [16, 23, 24, 31]. In order to gain some insight into phase change problems, it is useful to consider a relatively simple one-dimensional problem, for which an exact solution exists. In addition, this one-dimensional solution will be employed as part of the numerical procedure for solving two-dimensional, two-phase moving boundary problems, presented in subsequent chapters.

Josef Stefan (1835-1893) [52] is recognised as being the first person to make a detailed mathematical study of heat conduction involving moving boundaries. In this work he considers a pure material which can exist in either liquid or solid phases on the semi-infinite half space $0 \leq x < \infty$. The material is taken to be in the liquid phase initially, with some known uniform temperature distribution. At some initial time $t = 0$ say the temperature at $x = 0$ is dropped below the freezing temperature of the material and kept at that temperature thereafter. Stefan then posed the problem : at a given point t in time, what is the position of the solid/liquid interface, $x = \widehat{x}(t)$, and the corresponding temperature distributions in the solid and liquid phases, $T_s(x,t)$ and $T_l(x,t)$ respectively ?

This problem can be approached in various different ways; see, for example, the classic work by Carslaw and Jaeger [7]. Usually it is assumed that the material is initially in the liquid phase at some constant temperature T_{l0} which is above the freezing temperature of the liquid T_{lf}. At time $t = 0$, the surface $x = 0$ is cooled to the temperature T_{sb}, which is below T_{lf}, the freezing temperature of the liquid, and thereafter maintained at this level.

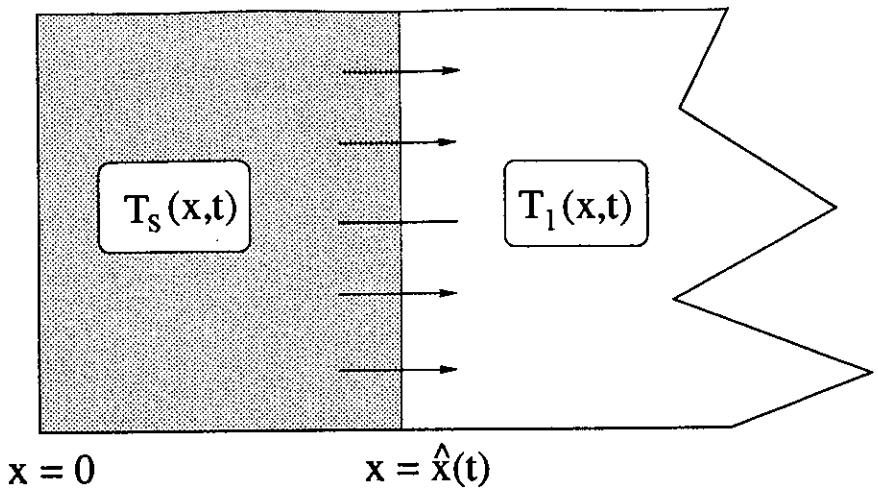

Figure 2.1: Freezing liquid with moving interface at $x = \hat{x}(t)$

As soon as the boundary temperature at $x = 0$ is dropped below the freezing temperature T_{lf}, a freezing front begins to propagate through the liquid region. Ahead of the freezing front the material is in the liquid phase and behind, the material is in the solid phase. Figure 2.1 shows a schematic representation of the freezing region. It is assumed that the physical and thermal properties for both the solid and liquid phase remain unchanged throughout the freezing process, that there is no change in volume whilst the material freezes and that the heat is transfered by conduction only. If the assumption about no volumetric change is not made, then bulk motion of the solid and/or liquid must be included, which increases the complexity of the governing equations greatly. Thus, the temperatures $T_s(x,t)$ and $T_l(x,t)$ are determined by solving the following heat conduction problems in time dependent domains

$$\begin{aligned} \frac{\partial T_s}{\partial t} &= \nu_s \frac{\partial^2 T_s}{\partial x^2}, \quad 0 \le x \le \hat{x}(t) \\ T_s(0,t) &= T_{sb}, \quad T_s(\hat{x}(t),t) = T_{lf}, \quad t > 0 \end{aligned} \tag{2.1}$$

behind the phase change front and

$$\begin{aligned} \frac{\partial T_l}{\partial t} &= \nu_l \frac{\partial^2 T_l}{\partial x^2}, \quad \hat{x}(t) \le x < \infty \\ T_l(\hat{x}(t),t) &= T_{lf}, \quad T_l(\infty,t) = T_{l0}, \quad t > 0 \\ T_l(x,0) &= T_{l0}, \quad 0 \le x < \infty, \end{aligned} \tag{2.2}$$

ahead of the phase change front, where ν_s and ν_l are the thermal diffusivities of the solid and liquid phase respectively. In addition, since there is no solid phase initially, we require that $\hat{x}(0) = 0$. It should be noted that at the interface of the two regions both temperatures take the same value, $T_s(\hat{x}(t),t) = T_l(\hat{x}(t),t) = T_{lf}$, the fusion temperature of the liquid. The condition on the liquid temperature at

$x = \infty$ forces the solution to remain stable i.e. the solution will not grow too fast nor will it blow up at infinity.

Essential to the derivation of heat flow in a material is Fourier's Law [3, 30] which states that the rate of heat flow across an isothermal surface (a surface of constant temperature) per unit area is proportional to the temperature gradient at the surface. Either side of the phase change front there is a difference in temperature which we need to relate to heat flow and it is Fourier's law which provides this link.

The freezing front moves in such a way that its velocity is proportional to the jump in heat flux across the front, this flux being due to the latent heat liberated on freezing. Specifically, if L is the latent heat of fusion, then when the front moves a distance $d\hat{x}$, a quantity of heat $\rho\, L\, d\hat{x}$ is released from the freezing liquid and is removed by conduction. So during the time interval dt we have a heat balance with heat flowing out of the liquid phase into the phase change interface and heat flowing out of the phase change interface into the solid phase. The difference between these heat fluxes must be equal to the latent heat liberated at the phase change interface, so that

$$K_s \frac{\partial T_s(\hat{x}(t),t)}{\partial x} - K_l \frac{\partial T_l(\hat{x}(t),t)}{\partial x} = \rho\, L \frac{d\hat{x}}{dt}, \tag{2.3}$$

where K_s and K_l are the thermal conductivities of the solid and liquid phases respectively. This equation is sometimes referred to as the Stefan condition, which along with (2.1), (2.2) and the initial condition $\hat{x}(0) = 0$ constitute all the mathematical information that is required to solve the problem posed by Stefan in [52]. The solution of this problem is discussed in Carslaw & Jaeger[7] and Crank [16]. In particular, they consider the case where initially the liquid is at the point of freezing, so that $T_l = T_{lf}$ everywhere. This means that when the boundary temperature is lowered, freezing takes place immediately and the problem reduces to one of heat conduction in the solid phase alone, since the temperature of the liquid at a point cannot change until the phase change front has passed through that point. This approximation leads to the retrieval of Neumann's solution of the planar problem [7, 16, 30, 31]. This solution is a special case of Stefan's problem with zero heat flux in the liquid region, the solution being completely determined in terms of the boundary condition.

Neumann's solution would be a suitable approximation to use if one was not taking account of the temperature distribution ahead of the moving boundary [12]. However, to take account of a variable temperature ahead of the front, a solution with varying temperature ahead of and behind the phase change front is required.

2.2 A Two-Phase Solution

A set of non-dimensional variables for the space, time and temperature is

$$x' = \frac{x}{a}, \quad \hat{x}' = \frac{\hat{x}}{a}, \quad t' = \frac{\nu_l t}{a^2}, \quad T'(x',t') = \frac{T(x,t) - T_{lf}}{T_t},$$

where a is an arbitrary length scale of the region and T_t is a typical scale for the initial temperature distribution. Using these non-dimensional variables and dropping primes, the governing equations (2.1), (2.2), the Stefan condition (2.3) and the initial condition $\hat{x}(0) = 0$ become

$$\begin{aligned} \frac{\partial T_s}{\partial t} &= \nu \frac{\partial^2 T_s}{\partial x^2}, \quad 0 \le x \le \hat{x}(t) \\ T_s(0,t) &= T_{sb}, \quad T_s(\hat{x}(t),t) = 0, \quad t > 0 \end{aligned} \tag{2.4}$$

behind the phase change front and

$$\begin{aligned} \frac{\partial T_l}{\partial t} &= \frac{\partial^2 T_l}{\partial x^2}, \quad \hat{x}(t) \le x < \infty \\ T_l(\hat{x}(t),t) &= 0, \quad T_l(\infty,t) = T_{l0}, \quad t > 0 \\ T_l(x,0) &= T_{l0}, \quad 0 \le x < \infty \end{aligned} \tag{2.5}$$

ahead of the phase change front. Here the non-dimensional diffusivity ν is given by

$$\nu = \frac{\nu_s}{\nu_l}. \tag{2.6}$$

In non-dimensional variables, the initial condition for the front position remains unchanged, $\hat{x}(0) = 0$, and the Stefan condition (2.3) becomes

$$K \frac{\partial T_s(\hat{x}(t),t)}{\partial x} - \frac{\partial T_l(\hat{x}(t),t)}{\partial x} = S_t \frac{d\hat{x}}{dt}, \tag{2.7}$$

where the non-dimensional constants

$$S_t = \frac{\rho L \nu_l}{T_t K_l} \quad \text{and} \quad K = \frac{K_s}{K_l} \tag{2.8}$$

are the Stefan number and the thermal conductivity respectively. The Stefan number or phase change parameter is the ratio of the latent heat to the heat capacitance of the liquid phase.

In general, the boundary condition at $x = 0$ would be a Newton cooling boundary condition [30, 31]; however, no fully analytical solutions exist for this boundary condition. An exact similarity solution does exist for the special case of a fixed temperature boundary condition with $T_s = T_{sb}$ at $x = 0$ (see Carslaw

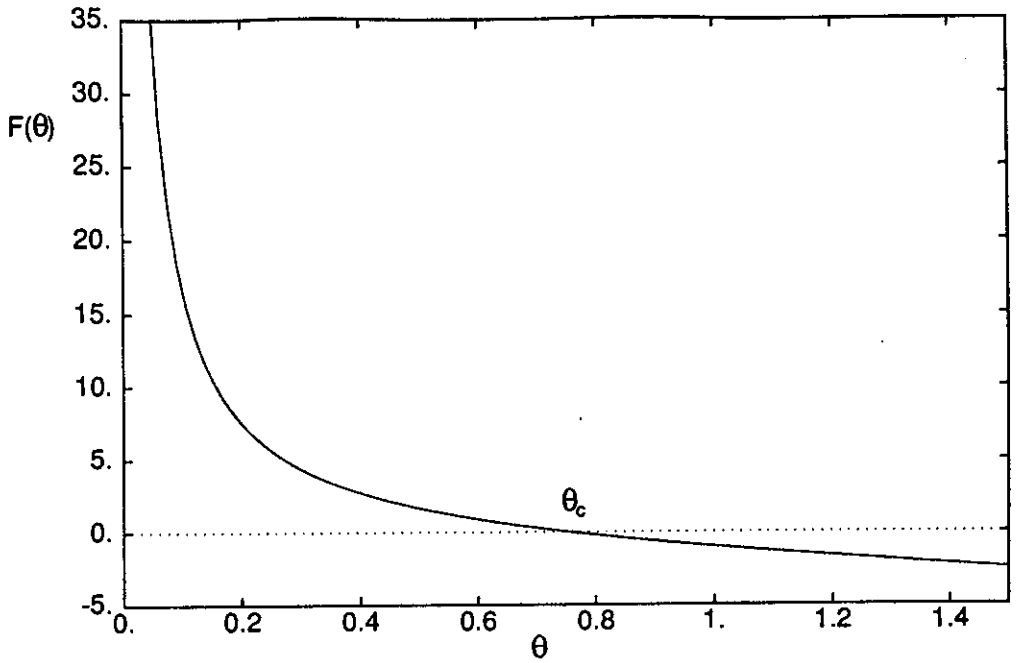

Figure 2.2: Plot of transcendental equation showing unique root θ_c for non-dimensional parameters $T_{sb} = -1.0$, $T_{l0} = 1.0$, $K = S_t = \nu = 1.0$

and Jaeger [7]). This solution is

$$\begin{aligned} T_s(x,t) &= T_{sb} - \frac{T_{sb}}{\operatorname{erf}\left(\frac{\theta}{2\sqrt{\nu}}\right)} \operatorname{erf}\left(\frac{x}{2\sqrt{\nu t}}\right) \\ \text{and} & \qquad (2.9) \\ T_l(x,t) &= T_{l0} - \frac{T_{l0}}{\operatorname{erfc}\left(\frac{\theta}{2}\right)} \operatorname{erfc}\left(\frac{x}{2\sqrt{t}}\right) \end{aligned}$$

(see Crank [16]). The phase change front is located at $x = \widehat{x}(t) = \theta\sqrt{t}$, where θ is the solution of

$$F(\theta) \equiv \frac{K\,T_{sb}}{\sqrt{\nu}\,\operatorname{erf}\left(\frac{\theta}{2\sqrt{\nu}}\right)} e^{-\theta^2/(4\nu)} - \frac{T_{l0}}{\operatorname{erfc}\left(\frac{\theta}{2}\right)} e^{-\theta^2/4} - \frac{1}{2}\sqrt{\pi}\,\theta\,S_t = 0. \qquad (2.10)$$

Figure 2.2 shows $F(\theta)$ plotted for some typical values of the non-dimensional parameters of the one-dimensional two-phase Stefan problem (Equations (2.4), (2.5) and (2.7)). It can be seen that the solution of $F(\theta) = 0$ is unique.

The solution of equation (2.10) will be required to start the numerical scheme for solving two-dimensional Stefan problems, to be described in Chapter 3.

Chapter 3

Two-Phase Problems

3.1 Governing Equations

In this section the governing equations for a two-dimensional moving boundary value problem, with heat being transfered by conduction alone, are presented. As in the one-dimensional case (see the previous chapter) the material is assumed to initially be in the liquid phase, leading to the formulation of a freezing problem. These equations are higher dimensional generalisations of those in Chapter 2.

To be specific, let us consider the freezing of a liquid contained in an arbitrary two-dimensional region R. The fixed boundary of the region R will be denoted by B_f. Inside the region R there will be a moving phase change front, which will be denoted by B_p. Furthermore, let us denote the temperature of the liquid by $T_l(\mathbf{r},t)$ and the temperature of the solid by $T_s(\mathbf{r},t)$, as shown in figure 3.1. Let the thermal diffusivity and thermal conductivity of the liquid and the solid be ν_l, K_l, ν_s and K_s respectively. The equation governing the heat flow in the solid is then

$$\frac{\partial T_s}{\partial t} = \nu_s \nabla^2 T_s \tag{3.1}$$

for points $\mathbf{r}$ lying between the fixed boundary B_f and the phase change front B_p, while the equation governing the heat flow in the liquid is

$$\frac{\partial T_l}{\partial t} = \nu_l \nabla^2 T_l \tag{3.2}$$

for points $\mathbf{r}$ lying ahead of the phase change front B_p [30]. Initially the region R is totally filled with liquid with some temperature distribution, so that the initial condition is

$$T_l(\mathbf{r},0) = T_{l0}(\mathbf{r}) \qquad \text{in} \quad R. \tag{3.3}$$

The boundary condition on the fixed boundary B_f is, in general, a Newton cooling condition

$$K_s\, \mathbf{n} \cdot \nabla T_s + h\,(T_s - T_a) = 0 \qquad \text{on} \quad B_f, \tag{3.4}$$

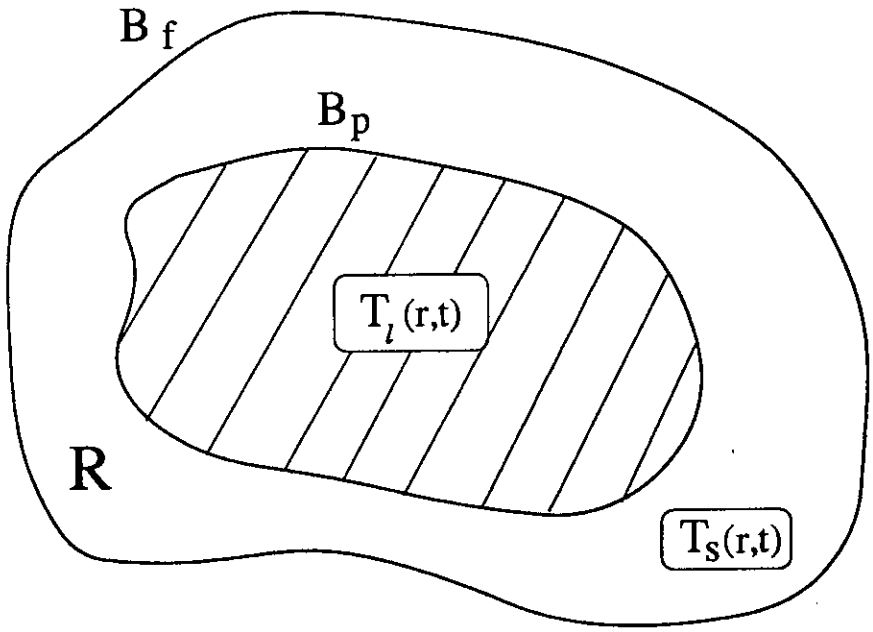

Figure 3.1: Region R with fixed boundary B_f and phase change front B_p

where $\mathbf{n}$ is the outward normal to the boundary and T_a is the temperature of the surroundings. The constant h is the surface heat transfer coefficient or surface conductance and K_s the thermal conductivity of the solid. On the moving boundary B_p the Stefan condition

$$K_s \frac{\partial T_s}{\partial n} - K_l \frac{\partial T_l}{\partial n} = L \rho \, \mathbf{n} \cdot \mathbf{V} \tag{3.5}$$

holds, where $\mathbf{n}$ is the outward normal to the solid region, $\mathbf{V}$ is the velocity of the phase change front, ρ is the density of the solid and L is the latent heat of fusion [30]. The Stefan condition expresses energy conservation across the phase change front, with energy being liberated due to the latent heat release as the liquid freezes. In deriving the Stefan condition it has been assumed for simplicity that the density of the solid and the density of the liquid are the same.

The governing equations (3.1) and (3.2), initial condition (3.3) and boundary conditions (3.4) and (3.5) can be non-dimensionalised relative to the parameter values for the liquid phase. Let temperature be measured with respect to the fusion temperature T_{lf} of the liquid and scaled with respect to some typical temperature T_t of the initial temperature distribution. A non-dimensional temperature T' is then

$$T' = \frac{T - T_{lf}}{T_t}. \tag{3.6}$$

If a is a typical length scale of the region R, then non-dimensional space and time variables can be defined by

$$\mathbf{r}' = \frac{\mathbf{r}}{a} \quad \text{and} \quad t' = \frac{\nu_l t}{a^2}. \tag{3.7}$$

Using these non-dimensional variables and dropping primes gives the non-dimensional equations

$$\frac{\partial T_s}{\partial t} = \nu \nabla^2 T_s \tag{3.8}$$

for the solid phase between the fixed boundary B_f and the phase change front B_p and

$$\frac{\partial T_l}{\partial t} = \nabla^2 T_l \tag{3.9}$$

for the liquid phase ahead of the phase change front B_p. The boundary condition (3.4) becomes

$$K_s \, \mathbf{n} \cdot \nabla T_s + a \, h \, (T_s - T_a) = 0 \tag{3.10}$$

on the fixed boundary B_f, where T_a is the non-dimensional temperature of the surroundings. The Stefan condition (3.5) becomes

$$K \frac{\partial T_s}{\partial n} - \frac{\partial T_l}{\partial n} = S_t \, \mathbf{n} \cdot \mathbf{V} \tag{3.11}$$

on the moving phase change front B_p. Here the non-dimensional diffusivity ν and conductivity K are

$$\nu = \frac{\nu_s}{\nu_l} \quad \text{and} \quad K = \frac{K_s}{K_l}. \tag{3.12}$$

The Stefan number S_t is

$$S_t = \frac{\rho \, \nu_l \, L}{K_l \, T_t}. \tag{3.13}$$

The non-dimensional equations (3.8) and (3.9), together with the Stefan condition (3.11), the initial condition $T_{l0} = \text{constant} > 0$ and the boundary condition $T_s = T_{sb} = \text{constant} < 0$ on the fixed boundary B_f (which corresponds formally to $\beta = K_s/(ah) = \infty$ in (3.10)) has an exact solution in one-dimension. This solution is given in the previous chapter.

3.2 Integral Equations

In this section the boundary integral equations used in the numerical solution of the two-dimensional Stefan problem will be derived from the heat equations (3.8) and (3.9) for the solid and liquid phases. These integral equations form a coupled system linked by the Stefan condition (3.11), which applies at the boundary between the liquid and solid phases. The numerical scheme presented here is an extension of the method of Coleman [12] to include a variable temperature ahead of the phase change front. Using the boundary integral method, the system of equations (3.8) and (3.9) is converted into a pair of coupled integral equations for the temperature ahead of and behind the phase change front. Let us consider first the integral equation for the temperature behind the front.

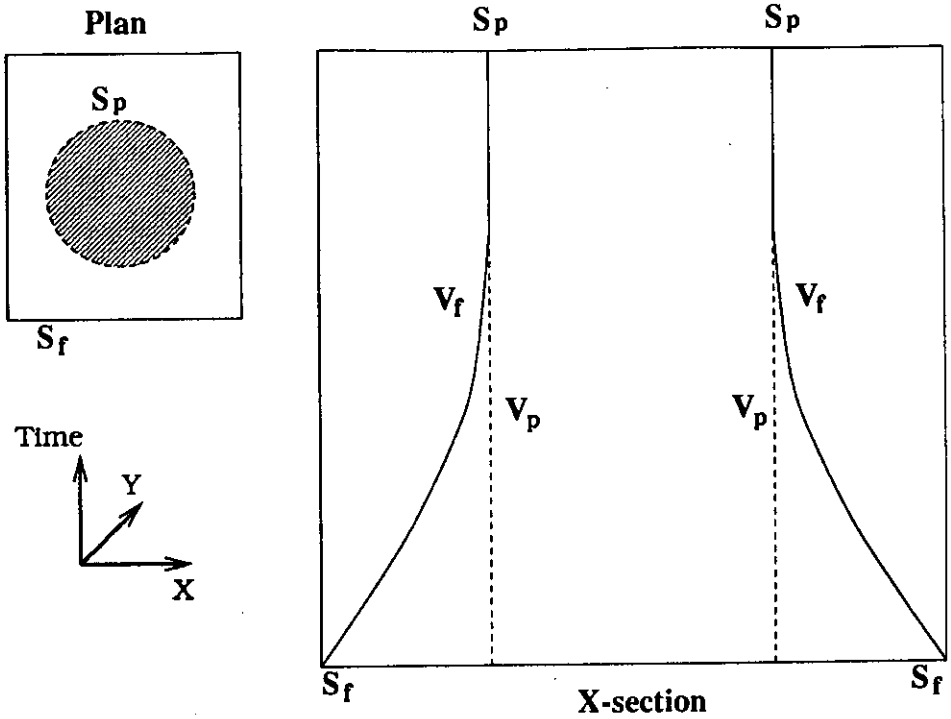

Figure 3.2: Fixed boundary B_f and phase change front B_p extended as surfaces S_f and S_p in space-time.

Let G_s be the Green's function

$$G_s(\mathbf{r},\mathbf{r}',t,t') = H(t-t')\frac{1}{4\pi\nu(t-t')}\exp\left(-\frac{|\mathbf{r}-\mathbf{r}'|^2}{4\nu(t-t')}\right), \tag{3.14}$$

so that

$$\frac{\partial G_s}{\partial t'} + \nu\,\nabla'^2\,G_s = -\delta(t-t')\,\delta(\mathbf{r}-\mathbf{r}'), \tag{3.15}$$

where ∇' refers to derivatives with respect to $\mathbf{r}'$ (see [7, 16, 12, 30]). It can then be shown from (3.8) and (3.15) that

$$\frac{\partial}{\partial t'}(G_s\,T_s') + \nu\nabla'\cdot(T_s{}'\nabla' G_s - G_s\nabla' T_s') = -T_s'\,\delta(t-t')\,\delta(\mathbf{r}-\mathbf{r}'), \tag{3.16}$$

where $T_s' = T_s(\mathbf{r}',t')$. The fixed boundary B_f and the phase change front B_p can be extended as surfaces S_f and S_p in space-time respectively, as shown in figure 3.2. The phase change front is then described by an equation of the form

$$t - f(\mathbf{r}) = 0 \tag{3.17}$$

in space-time. The outward unit normal to S_p is therefore given by

$$\mathbf{n}_p = \frac{(\nabla f, -1)}{\sqrt{1+|\nabla f|^2}}. \tag{3.18}$$

Let V_f be defined to be the space-time region between the fixed boundary of the region and the phase change front and V_p be defined to be the space-time region ahead of the phase change front, as shown in figure 3.2. Integrating equation (3.16) over space-time between the surfaces S_f and S_p gives

$$-\lambda T_s(\mathbf{r},t) = \int_{V_f} \frac{\partial}{\partial t'}(G_s T_s')\, dV' + \nu \int_{V_f} \nabla' \cdot (T_s' \nabla' G_s - G_s \nabla' T_s')\, dV'. \quad (3.19)$$

The parameter λ takes the value 1 at points away from the boundary and the value 1/2 at regular boundary points. The parameter $\lambda = \phi(\mathbf{r})/2\pi$, where $\phi(\mathbf{r})$ is the internal angle at the point $\mathbf{r}$ between the tangents to fixed boundary on either side of $\mathbf{r}$. In this case the volume element $dV' = dV_s'\, dt'$, where V_s is the $x-y$ region between the fixed boundary and the phase change front. Thus for the first integral in equation (3.19)

$$\int_{V_f} \frac{\partial}{\partial t'}(G_s T_s')\, dV' = \int_0^t \int_{V_s} \frac{\partial}{\partial t'}(G_s T_s')\, dV_s'\, dt' = \int_{V_s} [G_s T_s']_0^t\, dV_s' = 0, \quad (3.20)$$

since $G_s = 0$ at $t = t'$ and V_s vanishes at $t' = 0$. Applying the divergence theorem to the remainder of equation (3.19) then gives

$$-\lambda T_s(\mathbf{r},t) = \nu \int_{S_*} (T_s' \nabla' G_s - G_s \nabla' T_s') \cdot \mathbf{n}_p\, dS'. \quad (3.21)$$

The boundary S_* of the region V_f consists of two parts, the fixed boundary B_f (boundary S_f in space-time) and the phase change front S_p. Therefore

$$\begin{aligned} -\lambda T_s(\mathbf{r},t) &= \nu \int_0^{t+0} \int_{B_f} \left(T_s' \frac{\partial G_s}{\partial n'} - G_s \frac{\partial T_s'}{\partial n'} \right) ds'\, dt' \\ &\quad -\nu \int_{S_p} G_s \nabla' T_s' \cdot \mathbf{n}_p\, dS', \end{aligned} \quad (3.22)$$

since $T_s' = 0$ on the phase change front S_p. Using the outward unit normal (3.18) to the phase change surface S_p, this integral equation may be written as

$$\begin{aligned} -\lambda T_s(\mathbf{r},t) &= \nu \int_0^{t+0} \int_{B_f} \left(T_s' \frac{\partial G_s}{\partial n'} - G_s \frac{\partial T_s'}{\partial n'} \right) ds'\, dt' \\ &\quad -\nu \int_{S_p} G_s \frac{\nabla' T_s' \cdot \nabla' f}{\sqrt{1 + |\nabla' f|^2}}\, dS'. \end{aligned} \quad (3.23)$$

Projecting the integral over the surface S_p down onto the $x-y$ plane as the surface B_s finally gives

$$\begin{aligned} -\lambda T_s(\mathbf{r},t) &= \nu \int_0^{t+0} \int_{B_f} \left(T_s' \frac{\partial G_s}{\partial n'} - G_s \frac{\partial T_s'}{\partial n'} \right) ds' dt' \\ &\quad -\nu \int_{B_s} G_s(\mathbf{r},\mathbf{r}',t,f(x',y'))\, \nabla' T_s' \cdot \nabla' f|_{t'=f(x',y')}\, dx'\, dy'. \end{aligned} \quad (3.24)$$

This integral equation alone is not enough to determine the temperature behind the phase change front as the gradients $\nabla' T_s' \cdot \nabla' f|_{t'=f(x',y')}$ on the phase change front are not known. These unknown gradients are related to the same gradients ahead of the front by the Stefan condition (3.11). Differentiating with respect to time the equation for the phase change front in space-time, equation (3.17), gives

$$\nabla' f \cdot \mathbf{V} = 1, \tag{3.25}$$

and so the Stefan condition (3.11) yields

$$K \nabla' T_s' \cdot \nabla' f = S_t + \nabla' T_l' \cdot \nabla' f, \tag{3.26}$$

where S_t is the Stefan number (3.13). Since this Stefan condition relates temperature gradients ahead of and behind the phase change front, the temperature field ahead of the front also needs to be considered.

The equation governing the temperature field ahead of the phase change front is (3.9) and so the Green's function appropriate to the region ahead of the front is

$$G_l(\mathbf{r}, \mathbf{r}', t, t') = H(t - t') \frac{1}{4\pi(t - t')} \exp\left(-\frac{|\mathbf{r} - \mathbf{r}'|^2}{4(t - t')} \right). \tag{3.27}$$

G_l then satisfies

$$\frac{\partial G_l}{\partial t'} + \nabla'^2 G_l = -\delta(t - t')\, \delta(\mathbf{r} - \mathbf{r}'), \tag{3.28}$$

so that from (3.9)

$$\frac{\partial}{\partial t'}(G_l T_l') + \nabla' \cdot (T_l' \nabla' G_l - G_l \nabla' T_l') = -T_l' \delta(t - t')\, \delta(\mathbf{r} - \mathbf{r}'). \tag{3.29}$$

In a similar manner as for the temperature field behind the front, integrating this equation in space-time ahead of the phase change surface, S_p, yields

$$\begin{aligned} -\lambda T_l(\mathbf{r}, t) \;=\; & -\int_{S_0} T_l'(\mathbf{r}', 0)\, G_l(\mathbf{r}, \mathbf{r}', t, 0)\, dx'\, dy' \\ & + \int_{B_s} G_l(\mathbf{r}, \mathbf{r}', t, f(x', y'))\, \nabla' T_l' \cdot \nabla' f|_{t'=f(x',y')}\, dx'\, dy', \end{aligned} \tag{3.30}$$

on noting that the outward normal to the surface S_p is now $-\mathbf{n}_p$. The surface S_0 is the region inside the fixed boundary B_f. The integral equations (3.24) behind the phase change front and (3.30) ahead of the front, together with the Stefan condition (3.11), completely determine the temperature field within the material. The integral equation (3.24) involves both the temperature T_s and the normal temperature gradient $\partial T_s / \partial n$ on the fixed boundary B_f. In general, at any point on the fixed boundary, B_f, only the temperature, T_s, or the normal temperature

gradient, $\partial T_s/\partial n$, will be known. It is therefore necessary to determine the appropriate unknown temperature or normal temperature gradient as part of the solution process. For example, if a fixed temperature boundary condition is imposed on B_f, then the gradient $\partial T_s/\partial n$ on B_f will have to be determined. The calculation of the temperature distribution throughout the region will therefore require the determination of the unknown quantities on B_f, the position of the phase change front B_p and the temperature gradients $\nabla' T_l' \cdot \nabla' f|_{t'=f(x',y')}$ ahead of the front itself. Once these are known, the temperature at any point in the region can be determined using (3.24) and (3.30). Note that once the temperature gradients ahead of the phase change front are known, the Stefan condition (3.11) is used to calculate the corresponding temperature gradients $\nabla' T_s' \cdot \nabla' f|_{t'=f(x',y')}$ behind the phase change front. The numerical method used to determine these unknowns will now be described.

3.3 Numerical Scheme

In this section a method is presented to numerically solve the integral equations (3.24) and (3.30). This scheme is an extension of the method of Coleman [12] to include a variable temperature ahead of the phase change front and the possibility that Newton's method, which is used to determine the position of the phase change front, will not converge.

Let time be discretised into intervals of constant length Δt, so that $t_i = i\,\Delta t$, and let the temperature at time t_i be $T_{si}(\mathbf{r})$ behind the front and $T_{li}(\mathbf{r})$ ahead of the front. Then approximating the time integrals in (3.24) using the mid-point rule, we have that the temperature on the boundary at time step k is

$$\begin{aligned}
-\frac{1}{2}T_{sk}(\mathbf{r}) \approx\ & \nu\,\Delta t \sum_{i=1}^{k-1} \int_{B_f} \left(T_{si}' \frac{\partial}{\partial n'} G_s(\mathbf{r},\mathbf{r}',(k-1/2)\Delta t,(i-1/2)\Delta t) \right. \\
& \left. - G_s(\mathbf{r},\mathbf{r}',(k-1/2)\Delta t,(i-1/2)\Delta t)\, \frac{\partial T_{si}'}{\partial n'} \right) ds' \\
& + \nu \int_{B_f} \left(T_{sk}' \int_{(k-1)\Delta t}^{(k-1/2)\Delta t} \frac{\partial}{\partial n'} G_s(\mathbf{r},\mathbf{r}',(k-1/2)\Delta t,t')\, dt' \right. \\
& \left. - \frac{\partial T_{sk}'}{\partial n'} \int_{(k-1)\Delta t}^{(k-1/2)\Delta t} G_s(\mathbf{r},\mathbf{r}',(k-1/2)\Delta t,t')\, dt' \right) ds' \\
& - \nu \int_{B_s} G_s(\mathbf{r},\mathbf{r}',(k-1/2)\Delta t, f(x',y')) \\
& \quad \nabla' T_s' \cdot \nabla' f|_{t'=f(x',y')}\, dx'\, dy'. \qquad (3.31)
\end{aligned}$$

As in Coleman [12], the integral over the last time step has not been evaluated using the midpoint rule due to the singular nature of the Green's function there.

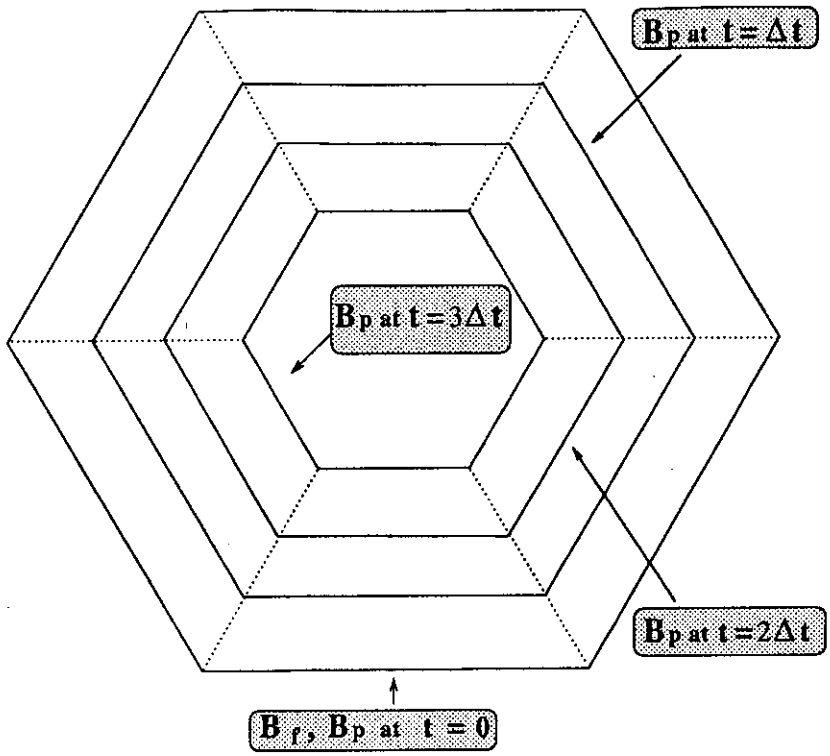

Figure 3.3: Distribution of quadrilaterals at time $3\Delta t$

Instead, over the last time step, the approximations

$$\int_{(k-1)\Delta t}^{(k-1/2)\Delta t} \frac{\partial}{\partial n'} G_s(\mathbf{r}, \mathbf{r}', (k-1/2)\Delta t, t')\, dt' \approx \frac{1}{2\pi\nu} \frac{(\mathbf{r}-\mathbf{r}')\cdot \mathbf{n}'}{|\mathbf{r}-\mathbf{r}'|^2} e^{-\frac{|\mathbf{r}-\mathbf{r}'|^2}{2\nu\Delta t}} \tag{3.32}$$

and

$$\int_{(k-1)\Delta t}^{(k-1/2)\Delta t} G_s(\mathbf{r}, \mathbf{r}', (k-1/2)\Delta t, t')\, dt' \approx \frac{1}{4\pi\nu} \mathrm{E_i}\left(\frac{|\mathbf{r}-\mathbf{r}'|^2}{2\nu\Delta t}\right) \tag{3.33}$$

are used, where $\mathrm{E_i}$ is the exponential integral [1].

Now that time has been discretised, space is also discretised. To evaluate the spatial integrals in (3.31), the boundaries B_f and B_p are approximated by N-sided polygons and T_s and $\partial T_s/\partial n$ are approximated by their midpoint values on the sides. The integrals are then evaluated using the midpoint rule, except for where G_s and $\partial G_s/\partial n'$ become singular. This occurs when $\mathbf{r}$ lies on the midpoint of a side of B_f, in which case by expanding about this point it can be shown that the term $\partial T_s/\partial n'$ in (3.31) has coefficient $\Delta L(\gamma - 2 + \log(\Delta L^2/(8\nu\Delta t)))/(4\pi\nu)$, where γ is the Euler constant and ΔL is the length of the side [12]. At these singular points, the term in (3.31) involving T_s on B_f is zero [12].

The integral over the surface B_s in (3.31) is evaluated in the following manner. The phase change front B_p is approximated by a polygon at each time step. By joining the vertices of these polygons for times 0 up to $k\Delta t$ together, a set of

quadrilaterals is formed which cover the surface B_s. By way of illustration, figure 3.3 shows a likely distribution of the quadrilaterals after three time steps when B_f is approximated by a hexagon. The integral over each of these polygons is then approximated by the value of the integrand at the centroid times the area of the quadrilateral, which is the midpoint rule in two dimensions. This approximation is valid for all quadrilaterals, except those between the $(k-1)$th and kth time step, due to G_s becoming singular on the phase change front B_p. As in Coleman [12], the integral over these quadrilaterals is approximated by

$$(\text{area of quadrilateral}) \times \frac{\nabla' T_s' \cdot \nabla' f|_{t'=(k-1/2)\Delta t}}{4\,\pi\,\nu\,\Delta t}\, \mathrm{E_i}\left(\frac{|\mathbf{r}-\mathbf{r}'|^2}{\nu \Delta t}\right), \tag{3.34}$$

where $\mathbf{r}'$ is the quadrilateral centroid. The function f is approximated by $(i-1/2)\Delta t$ for any quadrilateral between the $(i-1)$th and ith time step.

To evaluate the unknown gradients $\nabla' T_l' \cdot \nabla' f|_{t'=f(x',y')}$, the integral equation (3.30) is applied at the phase change front B_p where $T_l = 0$. Setting $T_l = 0$ at time $t = k\Delta t$, (3.30) gives

$$\begin{aligned} 0 \;\approx\; & -\int_{S_0} T_l'(\mathbf{r}',0)\, G_l(\mathbf{r},\mathbf{r}',(k-1/2)\Delta t,0)\, dx'\, dy' \\ & + \int_{B_s} G_l(\mathbf{r},\mathbf{r}',(k-1/2)\Delta t, f(x',y'))\, \nabla' T_l' \cdot \nabla' f|_{t'=f(x',y')}\, dx'\, dy', \end{aligned} \tag{3.35}$$

where $\mathbf{r}$ lies on the phase change front B_p. The second integral in this expression is evaluated in the same manner as the similar integral in (3.31). The first integral over the initial condition is evaluated by dividing the region inside B_f up into a grid. The integral is then approximated by the midpoint rule as the sum of the area of each grid box times the value of $T_l'(\mathbf{r}',0)G_l$ at the centroid.

The numerical procedure to solve (3.31) and (3.35) then works in the following manner. For definiteness, let us suppose that the boundary condition on B_f is the fixed temperature boundary condition $T_s = T_{sb} < 0$. We then assume that we know the temperature gradients $\nabla' T_l' \cdot \nabla' f|_{t'=f(x',y')}$ on the phase change front for times 0 up to $(k-1)\Delta t$. The position of the phase change front at time $k\Delta t$ is then approximated by extrapolating from its previous positions. The linear system arising from the integral equation (3.35) can then be solved for the unknown gradients $\nabla' T_l' \cdot \nabla' f|_{t'=f(x',y')}$ on the front at time $k\Delta t$. From these gradients and the Stefan condition (3.11), the gradients $\nabla' T_s' \cdot \nabla' f|_{t'=f(x',y')}$ behind the phase change front can then be determined. Substituting these gradients behind the phase change front into the linear system resulting from the integral equation (3.31), the unknown normal derivatives $\partial T_s/\partial n$ on the boundary B_f can then be found. Once these normal temperature derivatives are known, Newton's method,

with the temperature T_s given by the discretised form of (3.24), can then be used to find where the temperature T_s is zero. A revised position of the phase change front at time $k\Delta t$ is then determined. The whole process is repeated until the difference between the positions of successive estimates of the front is within a prescribed tolerance.

To start the process off, the one-dimensional solution (2.9) and (2.10) is used to give the front position and gradients $\nabla' T_l' \cdot \nabla' f|_{t'=f(x',y')}$ at time Δt. This solution will give a good approximation to these quantities at time Δt if Δt is small. To keep the phase change front smooth and to reduce truncation errors, when the iterations have converged, the points on the front are passed through a three point smoothing scheme. This smoothing of the front position at each time step is an essential part of the numerical scheme. In particular at time $t = \Delta t$ each point on the fixed boundary B_f is moved a fixed amount toward the centre of the region R. This results in points that are furthest away from the centre of the region (corner points) lagging behind the points closest to the centre. To improve the initial approximation at time $t = \Delta t$ for subsequent calculations the points are smoothed to bring them into alignment. It was found that the position of the phase change front could be successfully determined using Newton's method to search for when $T_s = 0$, unless ν was large. When ν is large, the derivative of the temperature T_s is small (see the one-dimensional solution (2.9)), and this causes Newton's method to converge slowly as successive estimates can be thrown far from the front position. To enable solutions to be found when ν is large, a bisection method was used to determine the position of the phase change front (searching for when $T_s = 0$) when Newton's method converges slowly. In applying the numerical scheme outlined in this section, Newton's method was used to determine the position of the phase change front, unless it did not converge within a fixed number of iterations. If Newton's method did not converge, the front finding method was then switched over to the bisection method. The procedure to solve the integral equations (3.31) and (3.35) can be summarised as follows :

Assuming a fixed temperature boundary condition on B_f,

1. For the first time step: The one-dimensional solution (2.9) and the transcendental equation (2.10) are used to give the front position and gradients.

2. Extrapolate to the next front position.

3. Solve the linear system arising from (3.35) to obtain the gradients $\nabla' T_l' \cdot \nabla' f|_{t'=f(x',y')}$ on the phase change front at time $k\Delta t$.

4. Use the Stefan condition (3.11) to obtain the gradients $\nabla' T_s' \cdot \nabla' f|_{t'=f(x',y')}$

behind the phase change front.

5. Solve the linear system which results from equation (3.31) to obtain the unknown normal temperature gradients $\partial T_s/\partial n$ on the boundary B_f.

6. Locate where T_s is zero using Newton's (Bisection) method.

7. Obtain an improved estimate of the phase change front position at time $k\Delta t$.

8. If the accepted tolerance (tol $= 5\times 10^{-3}$) is satisfied, go to step 2. Otherwise go to step 3.

A crucial part of the solution process is to solve the two linear systems of equations that occur as part of the numerical procedure. As with any implicit numerical method, these linear systems must be solved at each time step or, more precisely, for each estimate of the front position. This may seem to require a great deal of computation time but, behind the phase change front, the linear system takes on a special structure which provides not only a great saving in calculation, but also a vast reduction in storage requirements. In the cases considered here, the temperature T_s is specified at each point on the fixed boundary B_f and the normal temperature gradients are unknown at each point on B_f. Hence the integral equation behind the phase change front (3.31) can be rearranged into the following form

$$\begin{aligned}
&\nu\Delta t\sum_{i=1}^{k-1}\frac{\partial T'_{si}}{\partial n'}\int_{B_f} G_s\,ds' + \nu\frac{\partial T'_{sk}}{\partial n'}\int_{B_f}\int_{(k-1)\Delta t}^{(k-1/2)\Delta t} G_s\,dt'\,ds' \\
= \;& \nu\Delta t\sum_{i=1}^{k-1}\int_{B_f}\left(T'_{si}\frac{\partial G_s}{\partial n'}\right)ds' + \nu\int_{B_f} T'_{sk}\left(\int_{(k-1)\Delta t}^{(k-1/2)\Delta t}\frac{\partial G_s}{\partial n'}\,dt'\right)ds' \\
&-\nu\int_{B_s} G_s\nabla' T'_s\cdot\nabla' f|_{t'=f(x',y')}\,dx'dy' + \frac{1}{2}T_{sk}(\mathbf{r}),
\end{aligned} \tag{3.36}$$

where over each discretised interval of B_f the normal temperature gradients are taken to be constant. The linear system which results from equation (3.36) can be written in the standard form

$$\begin{pmatrix}
\Gamma_1 & 0 & 0 & 0 & \cdots & 0 \\
\Gamma_2 & \Gamma_1 & 0 & 0 & \cdots & 0 \\
\Gamma_3 & \Gamma_2 & \Gamma_1 & 0 & \cdots & 0 \\
\Gamma_4 & \Gamma_3 & \Gamma_2 & \Gamma_1 & & \\
\vdots & \vdots & \vdots & & \ddots & \\
\Gamma_k & \Gamma_{k-1} & \Gamma_{k-2} & & & \Gamma_1
\end{pmatrix}
\begin{pmatrix} \underline{x}_1 \\ \underline{x}_2 \\ \underline{x}_3 \\ \underline{x}_4 \\ \vdots \\ \underline{x}_k \end{pmatrix}
=
\begin{pmatrix} \underline{b}_1 \\ \underline{b}_2 \\ \underline{b}_3 \\ \underline{b}_4 \\ \vdots \\ \underline{b}_k \end{pmatrix}. \tag{3.37}$$

where $\mathbf{A}\,\underline{x} = \underline{b}$. The matrix $\mathbf{A}$ is a block matrix of coefficients of the unknown data on the fixed boundary B_f. Each block matrix, $\Gamma_i, i = 1,\cdots,k$, is constructed

from the integral of the Green's function G_s over the fixed boundary B_f. The vector $\underline{x}$ is partitioned into sub-vectors $\underline{x}_i, i = 1, \cdots, k$, and for the problems considered here contains the unknown normal temperature gradients, $\partial T_s/\partial n$, at each point on B_f. In general the vector $\underline{x}$ contains a mixture of temperatures and normal temperature gradients on B_f. The vector $\underline{b}$ is also partitioned into sub-vectors $\underline{b}_i, i = 1, \cdots, k$, and is constructed using the known data on the right hand side of equation (3.36). Each block matrix, $\mathbf{\Gamma}_i, i = 1, \cdots, k$, is an $n \times n$ matrix, with n being the number of discretised points on the fixed boundary B_f. The vectors $\underline{x}$ and $\underline{b}$ have n entries per sub-vector, $\underline{x}_i$ and $\underline{b}_i$, $i = 1, \cdots, k$, respectively.

Each row in the linear system (3.37) corresponds to a phase change front and the structure at a time step of matrix $\mathbf{A}$ is due to causality. Hence, the system (3.37) would be produced at the kth phase change front position (i.e. kth time step). Notice that the structure of $\mathbf{A}$ allows the linear system to be written as

$$\mathbf{\Gamma}_1 \, \underline{x}_1 = \underline{b}_1 \tag{3.38}$$

for the first time step, and more generally,

$$\mathbf{\Gamma}_1 \, \underline{x}_j = \underline{b}_j - \sum_{i=2}^{j} \left(\mathbf{\Gamma}_i \, \underline{x}_{j+1-i} \right), \quad 2 \leq j \leq k, \tag{3.39}$$

for subsequent time steps. To solve for the sub-vector of unknowns $\underline{x}_j$, the structure of (3.39) dictates that at each time step it is the same coefficient matrix, $\mathbf{\Gamma}_1$, that requires inversion. As a consequence of this only one matrix inversion is required. Clearly this inversion is performed during the first time step and the LU decomposition of $\mathbf{\Gamma}_1$ is stored and utilised at the subsequent time steps, resulting in a great saving of computation time. Furthermore, the structure of the system (3.37) and the corresponding equations (3.39) allows the calculation of $\underline{x}_j$ to be performed with the storage of only the first column of the matrix $\mathbf{A}$,

$$(\mathbf{\Gamma}_1, \mathbf{\Gamma}_2, \mathbf{\Gamma}_3, \mathbf{\Gamma}_4, \cdots, \mathbf{\Gamma}_k)^T, \tag{3.40}$$

and the right hand side vectors $\underline{b}_j$, which provides a great reduction in storage requirements.

The integral equation ahead of the phase change front (3.35) can be written in the following form

$$\nabla' T_l' \cdot \nabla' f|_{t'=f(x',y')} \int_{B_s} G_l \, dx'dy' = \int_{S_0} T_l'(\mathbf{r}', 0) \, G_l \, dx'dy', \tag{3.41}$$

where the temperature gradients $\nabla' T_l' \cdot \nabla' f|_{t'=f(x',y')}$ are assumed to be constant over a discretised interval of the phase change front B_p. Unlike the the linear system behind the phase change front, the same coefficient matrix, $\mathbf{\Gamma}_1$, is not

obtained for each position of the phase change front. This is because instead of having a fixed boundary for all time, the position of the phase change front, B_p, changes at each time step. Thus, the coefficient matrix must be recalculated at every time step and a new LU decomposition calculated for every estimate of the front position.

3.4 Results

The boundary integral method outlined in the previous section was applied to a number of examples of the freezing of a region. For simplicity, the boundary condition applied on B_f was taken to be $T_s = T_{sb} < 0$ and the initial condition was taken to be $T_l = T_{l0} \geq 0$, where T_{sb} and T_{l0} are constants. With these initial and boundary conditions, the phase change front will start to move instantaneously. As a check on the numerical scheme, the fixed boundary B_f was taken to be a square of side length 2 and T_{l0} was set equal to zero. This then reduces to one of the examples considered by Coleman [12], as the temperature ahead of the phase change front is constant at $T_l = 0$. With $T_{sb} = -1$, $S_t = 1$, $\nu = 1$ and $K = 1$, the time for the complete freezing of the region was found to be 0.474695, which agrees with the value 0.475 found by Coleman [12].

In the following examples the contour plots were drawn using N.C.A.R. graphics version 2.0 [11]. The surface and the (x, y) type two dimensional plots where drawn using GNUplot version 3.5.

Figures 3.4 to 3.7 show the solution for the boundary temperature $T_{sb} = -1.0$ and the initial temperature $T_{l0} = 0.60$ with the parameter values $\nu = 8.9649$, $S_t = 3.5732$ and $K = 4.1516$. The temperature is scaled by a base of $T_t = 20\,^{\circ}C$. These parameter values are those appropriate for water freezing to ice [17]. For these parameter values, Newton's method converges slowly and a bisection method was used to determine the position of the phase change frout. The region inside B_f was taken to be a square of side length 2. Figures 3.4, 3.5, 3.6 and 3.7 show contour and surface plots of the temperature field at intervals of $3\Delta t$, $\Delta t = 0.01$. The phase change front can be clearly seen, particularly in the contour plots. Figure 3.9 shows the temperature profiles along $x = 0$ for $y > 0$. At the interface between the two phases, the discontinuity of the temperature derivative is apparent. The discontinuity occurs close to, but not exactly at $T_s = 0$, due to numerical error. By reducing the tolerance for accepting the position of a front, error can be reduced to a desired level.

The time evolution of the phase change front is shown in figure 3.8 at time intervals of 0.03. This figure shows the front positions at each time step up to

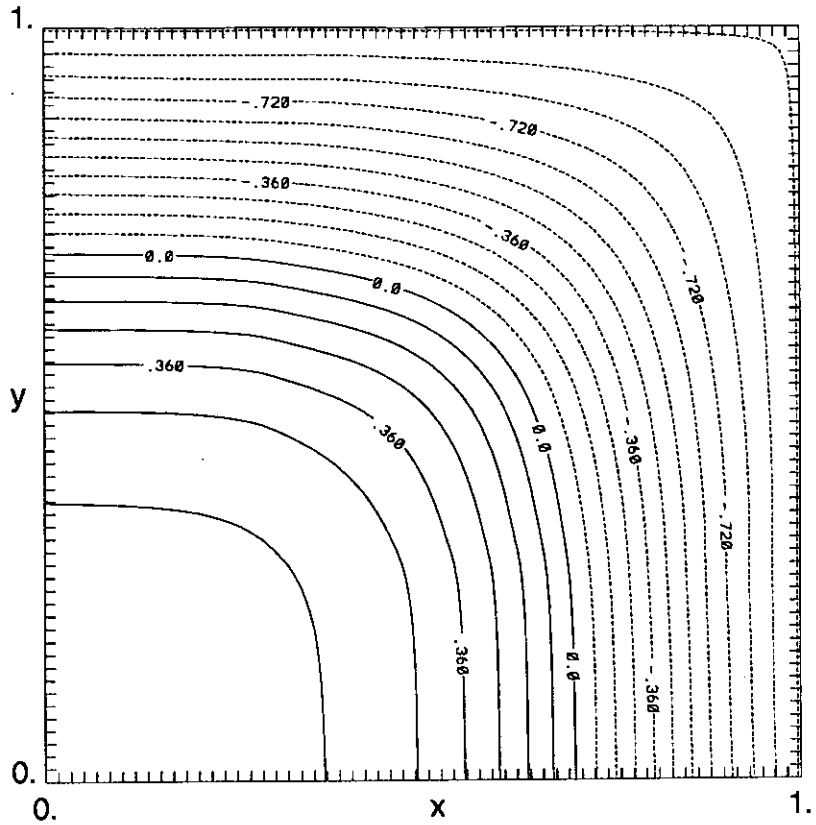

(a) Isotherms from -1.0 to 0.540 at intervals of 0.09

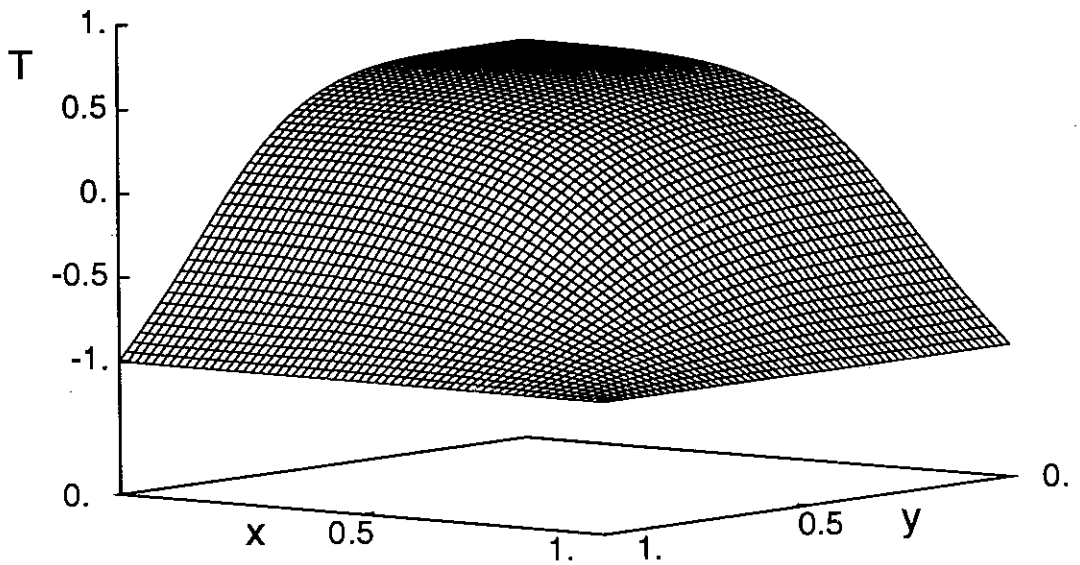

(b) Temperature distribution for $x > 0$ and $y > 0$ in region R

Figure 3.4: Temperature distribution at time $t = 0.050$ with initial condition $T_{l0} = 0.6$, boundary condition $T_{sb} = -1.0$, $\Delta t = 0.01$ and $\Delta s = 0.0125$. Here $\nu = 8.9649$, $S_t = 3.5732$ and $K = 4.1516$ (values for water).

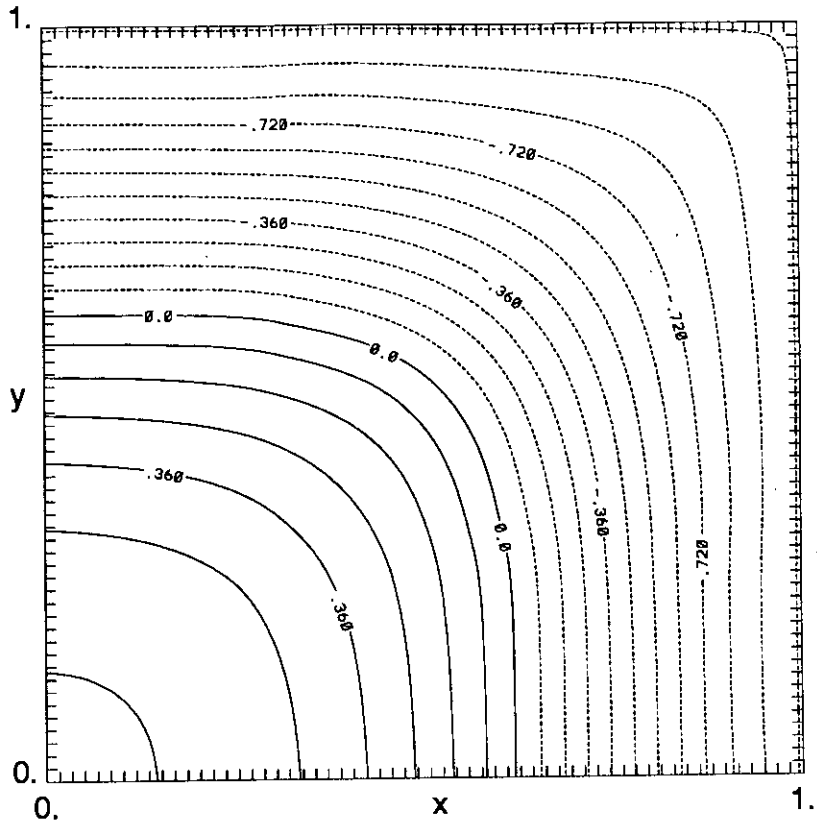

(a) Isotherms from -1.0 to 0.540 at intervals of 0.09

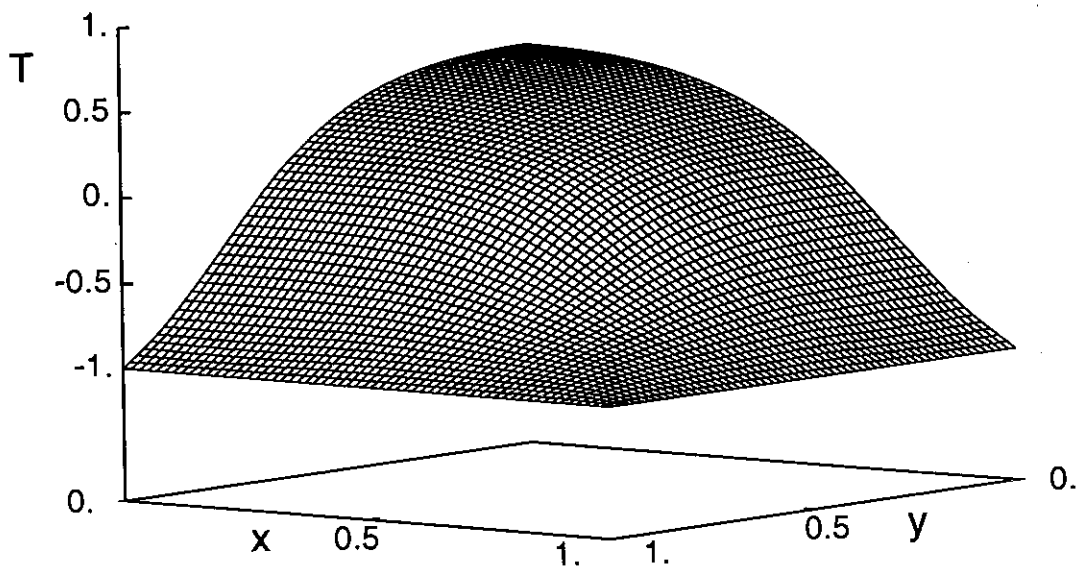

(b) Temperature distribution for $x > 0$ and $y > 0$ in region R

Figure 3.5: Temperature distribution at time $t = 0.080$ with initial condition $T_{l0} = 0.6$, boundary condition $T_{sb} = -1.0$, $\Delta t = 0.01$ and $\Delta s = 0.0125$. Here $\nu = 8.9649$, $S_t = 3.5732$ and $K = 4.1516$ (values for water).

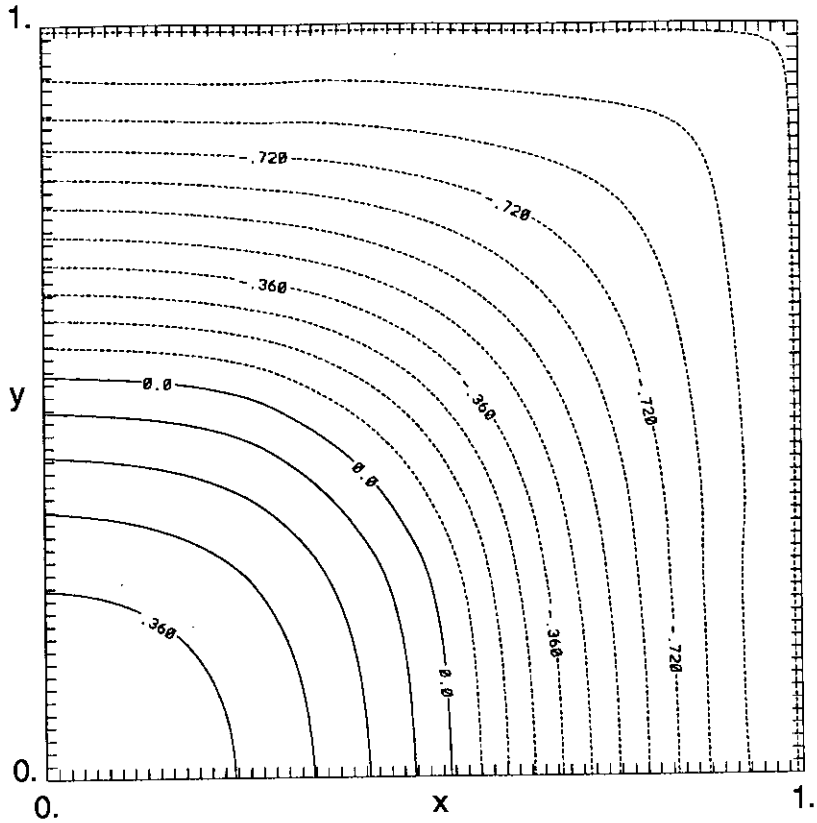

(a) Isotherms from -1.0 to 0.360 at intervals of 0.09

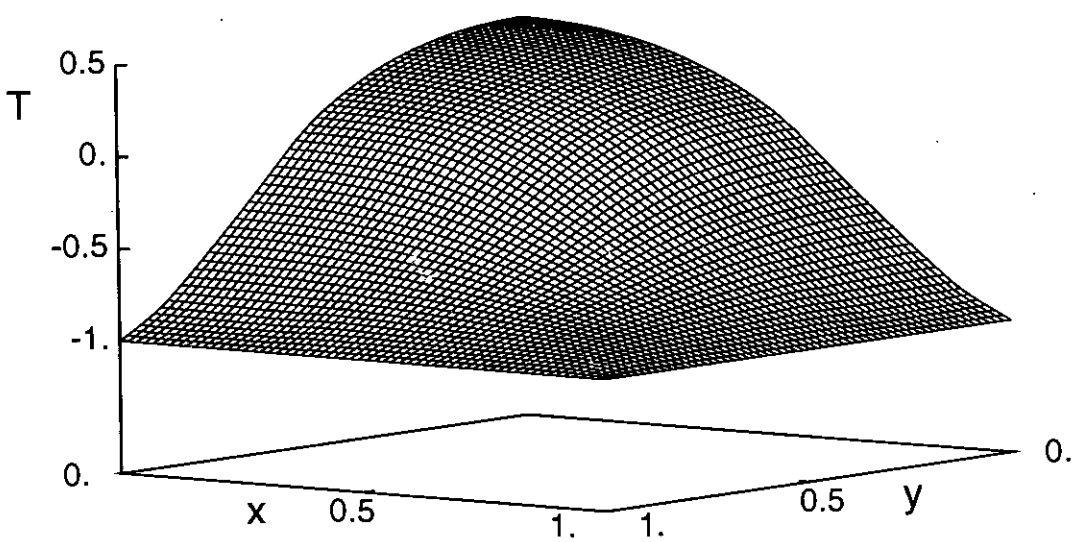

(b) Temperature distribution for $x > 0$ and $y > 0$ in region R

Figure 3.6: Temperature distribution at time $t = 0.110$ with initial condition $T_{l0} = 0.6$, boundary condition $T_{sb} = -1.0$, $\Delta t = 0.01$ and $\Delta s = 0.0125$. Here $\nu = 8.9649$, $S_t = 3.5732$ and $K = 4.1516$ (values for water).

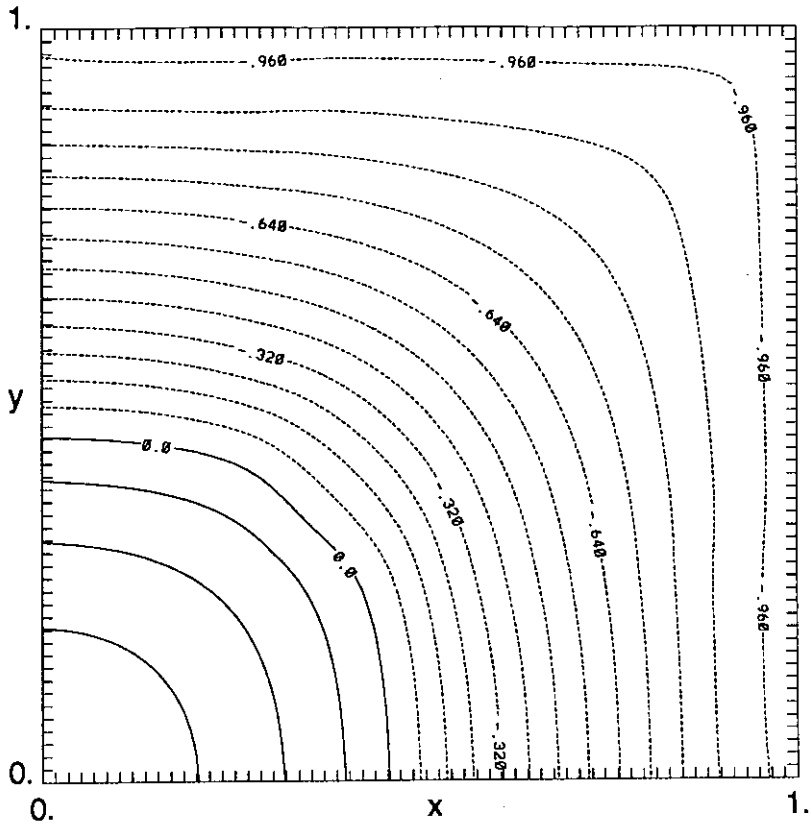

(a) Isotherms from -1.0 to 0.270 at intervals of 0.09

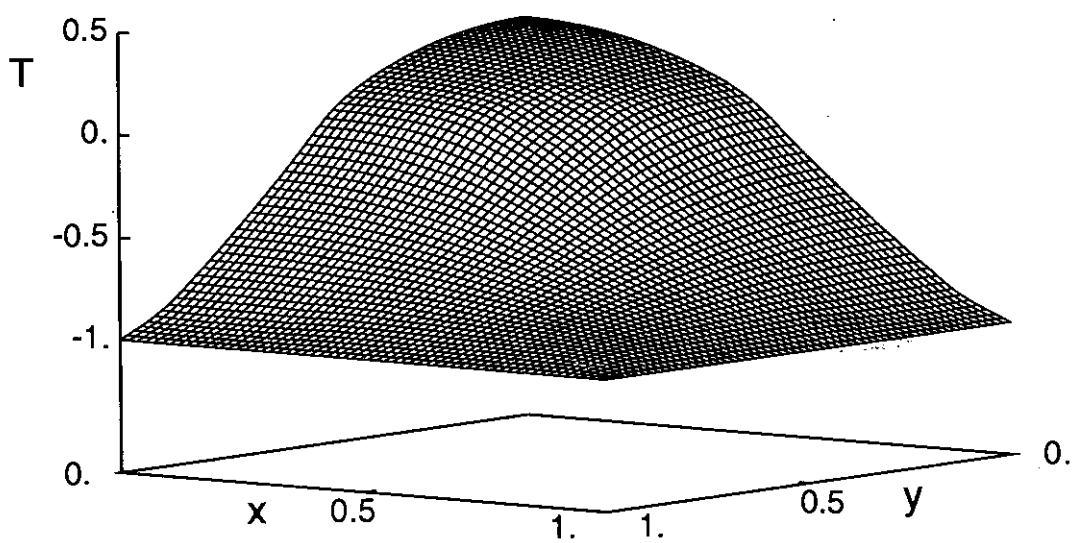

(b) Temperature distribution for $x > 0$ and $y > 0$ in region R

Figure 3.7: Temperature distribution at time $t = 0.140$ with initial condition $T_{l0} = 0.6$, boundary condition $T_{sb} = -1.0$, $\Delta t = 0.01$ and $\Delta s = 0.0125$. Here $\nu = 8.9649$, $S_t = 3.5732$ and $K = 4.1516$ (values for water).

the given time. It can be seen that the front is evolving to a circular shape as time increases. The freezing time for the parameter values used in figure 3.8 is 0.336943, which is smaller than the freezing time for the example of Coleman [12]. This is due to the larger values of the thermal conductivity K and the thermal diffusivity ν, which mean that heat is more easily transported to the boundary B_f. The Stefan number S_t is larger than for the example of Coleman [12], which means that more heat is liberated at freezing. This, and the larger value of the initial temperature T_{l0}, would cause the freezing time to increase over the value of Coleman [12]. However the larger values of the thermal diffusivity and the thermal conductivity have the greater effect and the freezing time decreases. The fact that the freezing time is not much reduced over the value of Coleman [12] shows that the increased values of ν, K, S_t and T_{l0} have effects which nearly balance out.

Figure 3.10 shows the variation of the freezing time t_f with T_{l0} for $T_{sb} = -1.0$, $\nu = 8.9649$, $S_t = 1.0$ and $K = 4.1516$ (taking $T_t = 20\,^oC$). These parameter values are those for water, except for S_t. For this high value of ν, Newton's method converges slowly and the bisection method was used to locate the position of the phase change front. As expected, the freezing time increases with the initial temperature T_{l0}, with the increase being nearly linear. The increase in the freezing time t_f as the initial temperature T_{l0} ranges from 0 to 1 is not very large because the boundary temperature is relatively low at $T_{sb} = -1$. This low boundary temperature and the large relative thermal diffusivity ν of the solid phase then dominate the heat flow. Figure 3.11 shows the variation of the freezing time t_f with the initial temperature T_{l0} for $T_{sb} = -1.0$, $\nu = 0.5$, $S_t = 3.5732$ and $K = 4.1516$. The values of S_t and K used for this figure are the values appropriate for water. The freezing time again increases with increasing initial temperature T_{l0} in a nearly linear fashion. The freezing times in figure 3.11 are larger than those in figure 3.10 due both to the smaller value of ν and the larger value of S_t. The smaller value of ν means that heat diffuses out of the region at a slower rate and the larger value of S_t means that more heat is liberated on freezing, which then has to diffuse out of the region.

Figure 3.12 shows the variation of the freezing time t_f with T_{l0} for $T_{sb} = -1.0$ and the water parameters ($\nu = 8.9649$, $S_t = 3.5732$ and $K = 4.1516$ for $T_t = 20\,^oC$). The freezing time again increases with T_{l0}, as expected, but in this case the increase is highly nonlinear, with the rate of increase slowing with increasing T_{l0}. The freezing times are between those of figures 3.10 and 3.11. The freezing times are increased over those of figure 3.10 due to the larger value of S_t leading to more heat liberated on freezing and are decreased over those of figure 3.11 due

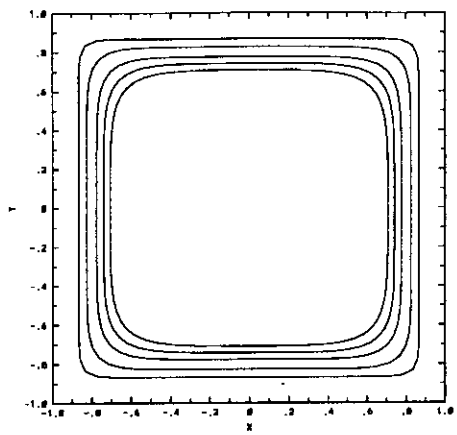

(a) At time $t = 0.050$

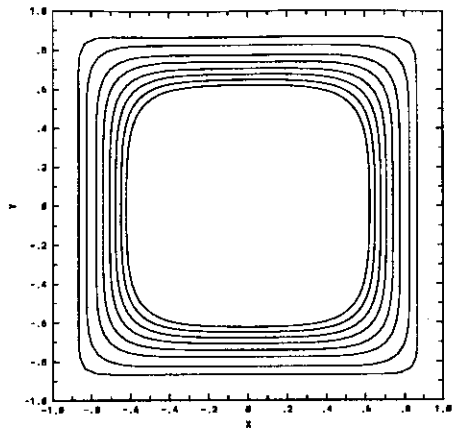

(b) At time $t = 0.080$

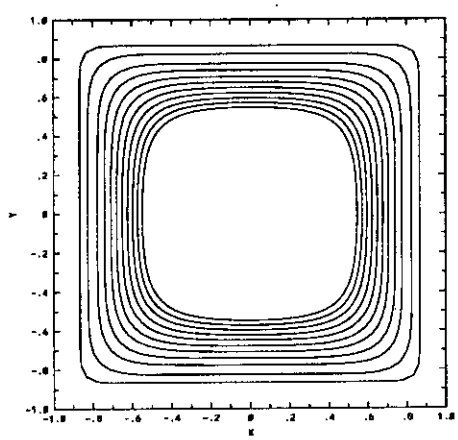

(c) At time $t = 0.110$

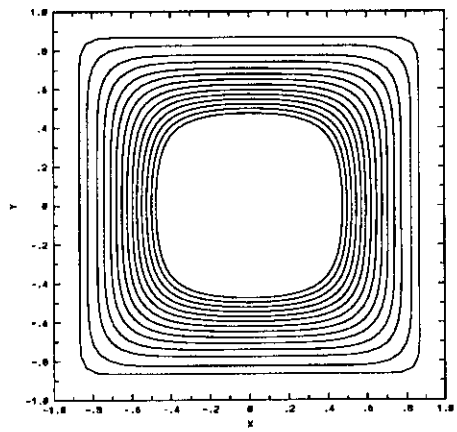

(d) At time $t = 0.140$

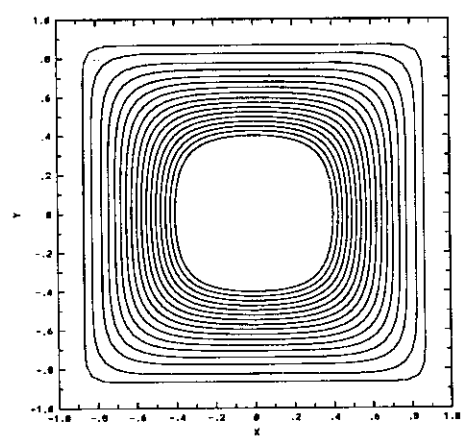

(e) At time $t = 0.170$

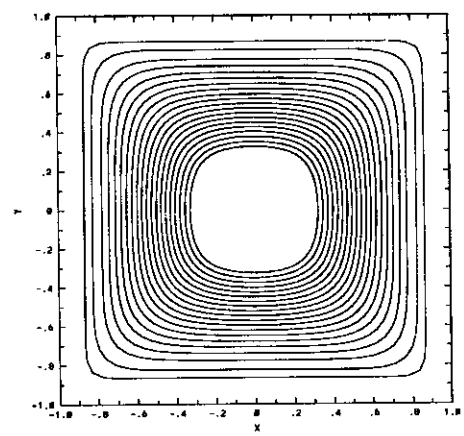

(f) At time $t = 0.200$

Figure 3.8: Time evolution of the phase change front with initial condition $T_{l0} = 0.6$, boundary condition $T_{sb} = -1.0$, $\Delta t = 0.01$ and $\Delta x = 0.0125$. Here $\nu = 8.9649$, $S_t = 3.5732$ and $K = 4.1516$ (values for water).

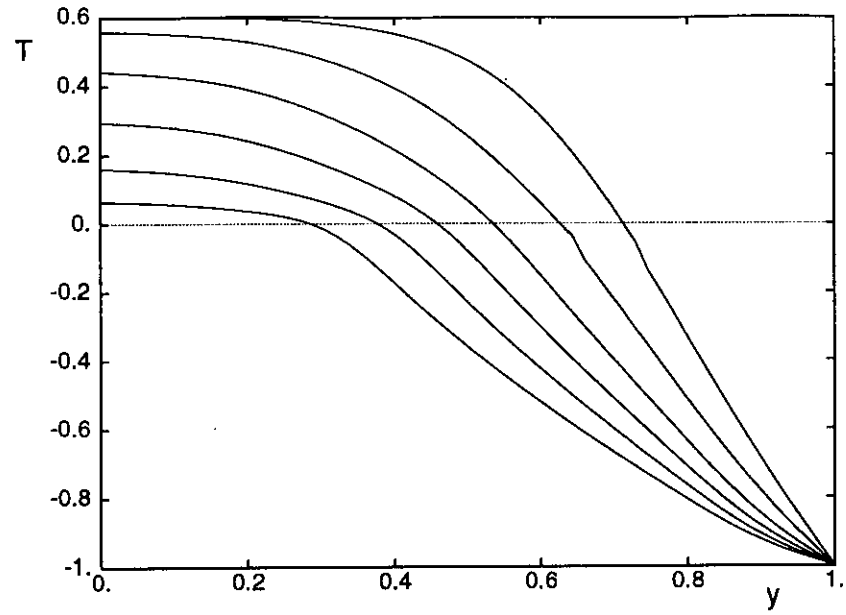

Figure 3.9: y cross–section of the region along $x = 0$: temperature profiles at 6 time intervals starting from $5\Delta t$ to $20\Delta t$, $\Delta t = 0.01$ for the initial condition $T_{l0} = 0.60$ and boundary condition $T_{sb} = -1.0$. Here $\nu = 8.9649$, $S_t = 3.5732$ and $K = 4.1516$ (values for water).

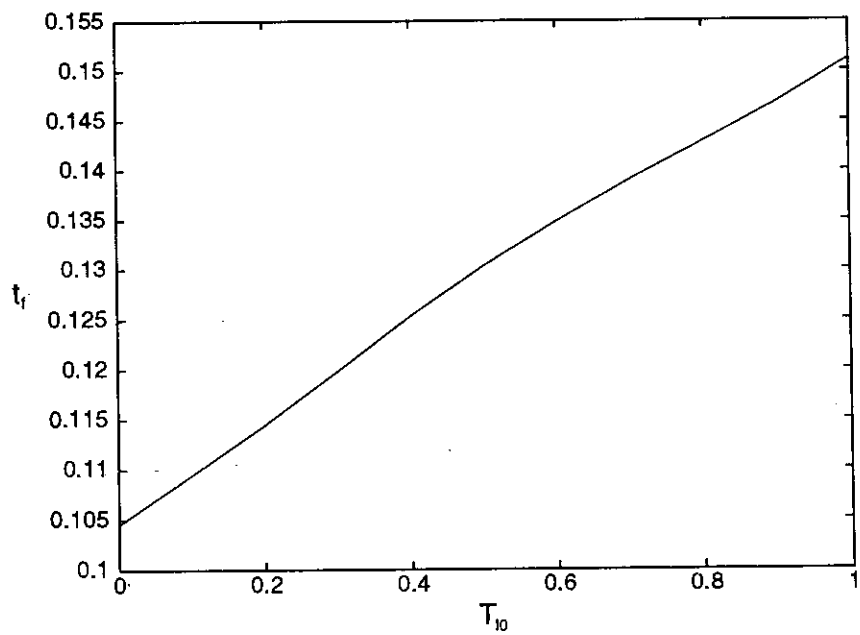

Figure 3.10: Plot of freezing time t_f as a function of T_{l0} for a square of side length 2 for the parameter values $T_{sb} = -1.0$, $\nu = 8.9649$, $S_t = 1.0$ and $K = 4.1516$.

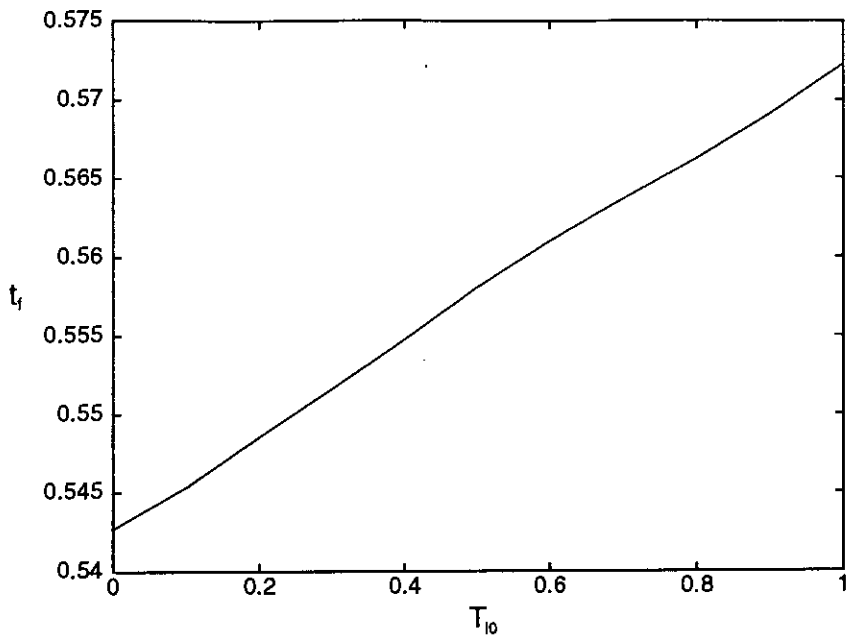

Figure 3.11: Plot of freezing time t_f as a function of T_{l0} for a square of side length 2 for the parameter values $T_{sb} = -1.0$, $\nu = 0.5$, $S_t = 3.5732$ and $K = 4.1516$.

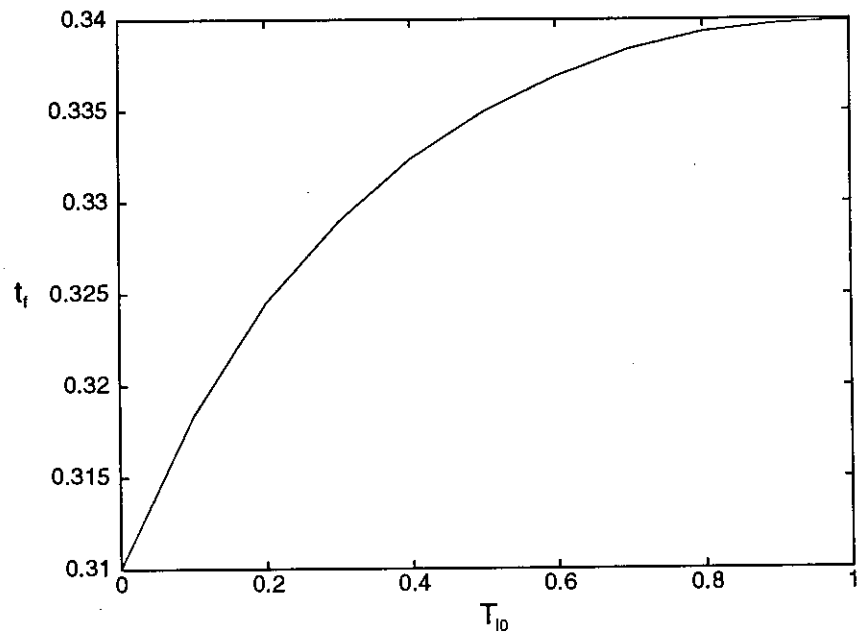

Figure 3.12: Plot of freezing time t_f as a function of T_{l0} for a square of side length 2 for the parameter values $T_{sb} = -1.0$, $\nu = 8.9649$, $S_t = 3.5732$ and $K = 4.1516$ (the values of ν, S_t and K are those for water freezing to ice with $T_t = 20\,^oC$).

to the larger value of ν leading to more rapid loss of heat.

3.5 Crystal Formation

The numerical method outlined in section 3.3 can be used, together with a simple model of crystal formation, to predict the sizes of crystals formed when a liquid freezes. If the growth of the crystal is radially symmetric, Frank [27] and Coriell and McFadden [15] showed that the size of the crystal formed when a liquid freezes is given in dimensional units by

$$S = \sqrt{\frac{2\,K_l\,(T_m - T_\infty)\,t}{\rho\,L}}. \tag{3.42}$$

Here K_l is the thermal conductivity of the liquid, L is the latent heat, T_m is the freezing temperature of the liquid and T_∞ is the temperature far ahead of the growing crystal. It should be emphasised that this expression is valid for the stable freezing of a liquid and is not valid for the dendritic growth which occurs when the liquid is undercooled [35]. The size expression (3.42) holds for a single crystal which has been growing for a time t and was found to give crystal sizes in accord with experimental results [15]. When a region freezes, as in the numerical solutions of the previous section, a large number of crystals form, the crystal at a given point being formed when the phase change front passes that point. Hence to apply the crystal growth expression (3.42) to the freezing of a region, this expression needs to be applied to each crystal formed (i.e. at each point of the region), where the time t is the time taken for a given crystal to form. In the present case, the crystal size expression (3.42) is most easily applied if the time t is replaced by the front velocity. This is in agreement with models of microstructure formation which show that the size of microstructural features is primarily determined by the speed of the phase change front [45, 44]. If the phase change front were planar, then the non-dimensional front position is given by $x = \theta\sqrt{t}$ (see (2.10)), so that the non-dimensional front velocity is $V = \theta/(2\sqrt{t})$. Eliminating time in favour of front velocity in the crystal size expression (3.42) and using (3.7) to convert to dimensional variables gives the alternative crystal size expression

$$S = \frac{a\theta}{V}\sqrt{\frac{c_l(T_m - T_\infty)}{2L}}, \tag{3.43}$$

where c_l is the specific heat of the liquid. While the phase change fronts considered in the present work are not planar, it was noted by Coleman [12] that even for non-planar phase change fronts, the position of the front is proportional to $\sqrt{t}$ to a good approximation. Therefore the crystal size expression (3.43) will be used in the present work on the freezing of two-dimensional regions.

The crystal sizes formed when the liquid in a region freezes are then calculated in the following manner using the boundary integral method of section 3.3. Using the positions of the phase change front calculated by the numerical scheme of section 3.3, the normal velocity V_n of a point on the front at a given time step can be calculated. This normal velocity V_n is then used as the velocity V in the crystal size expression (3.43). The crystal size expression (3.43) is now employed to calculate the crystal size in each quadrilateral used to calculate the surface integral B_s. At each time step, the parameter θ is determined from the transcendental equation (2.10) with T_{sb} set equal to the boundary temperature and T_{l0} set equal to the temperature at the centre of the square of section 3.4. While this transcendental equation is strictly valid only for a planar phase change front, the crystal size was found to be only weakly dependent on the value of θ. Indeed, the crystal sizes were found not to change to a significant extent if θ was set equal to its initial value. The value of θ was calculated using (2.10) so that the effect of the changing temperature of the liquid could be included. The temperature T_∞ is taken to be the boundary temperature T_{sb} and, for water, the freezing temperature is $T_m = 0$, these temperatures being made dimensional using (3.6). Hence the crystal size in each quadrilateral used to calculate the surface integral B_s can then be calculated. Adding up all such local crystal sizes over all positions of the phase change front until the region has completely frozen and dividing by the area of the region then gives the average crystal size $\bar{S}$.

Figure 3.13 shows a plot of the mean crystal size $\bar{S}$ as a function of the freezing time t_f for $T_{sb} = -1.0$ and the water parameters with $T_t = 20\,^\circ C$ and $a = 5.0cm$. The mean crystal size is nearly linear in t_f, except near $t_f = 0.34$ (i.e. except for initial temperatures near $T_{l0} = 1.0$: see figure 3.12). The rapid increase in the mean crystal size near $T_{l0} = 1$ is related to the slow increase of the freezing time with initial temperature T_{l0} near $T_{l0} = 1$, which can be seen in figure 3.12. The increase of the mean crystal size with freezing time is expected since a longer freezing time means a smaller mean front speed, which in turn leads to a larger crystal size. The actual mean crystal sizes, while a little on the high side, are in reasonable accord with the ice crystal sizes reported by Coriell and McFadden [15]. One reason for the mean crystal sizes being somewhat higher than experimental values is that the fluid flow ahead of the phase change front has been neglected. This flow is expected to produce faster freezing times and hence smaller mean crystal sizes. The inclusion of fluid flow into the freezing model is discussed in Chapter 4. The experimental measurements of Miyawaki *et al.* [37] of the freezing of soy protein curd show a basically linear dependence of the mean crystal size on freezing time (with a large amount of experimental scatter),

which is in qualitative agreement with our simple model of crystal formation on freezing. Unfortunately, the exact experimental conditions were not reported in this work, so that quantitative comparisons with their results cannot be made. Figure 3.14 shows the dependence of the mean crystal size $\bar{S}$ on the boundary temperature T_{sb} for fixed initial temperature $T_{l0} = 0.1$ and the water parameters with $T_t = 20\,^{\circ}C$ and $a = 5.0cm$. The mean crystal size decreases with decreasing boundary temperature, which is expected since a lower boundary temperature implies a larger mean front speed, which leads to a smaller crystal size. The mean crystal size dependence shown in figure 3.14 shows a good qualitative similarity to the experimental measurements for soy protein curd obtained by [37].

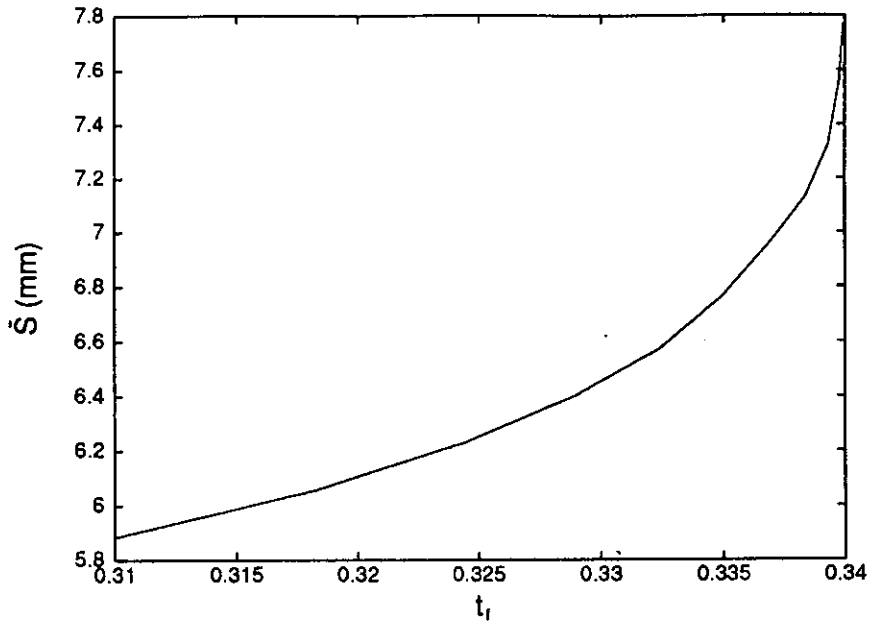

Figure 3.13: Plot of the mean crystal size $\bar{S}$ as a function of the freezing time t_f for $T_{sb} = -1.0$ and the water parameters $\nu = 8.9649$, $S_t = 3.5732$ and $K = 4.1516$ with $T_t = 20\,^{\circ}C$ and $a = 5.0cm$.

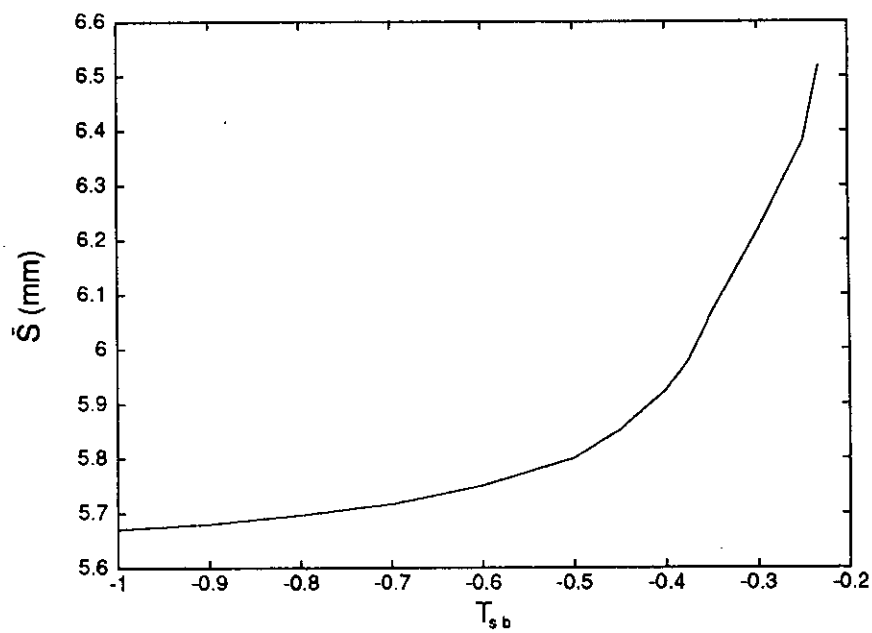

Figure 3.14: Plot of the mean crystal size $\bar{S}$ as a function of the boundary temperature T_{sb} for $T_{l0} = 0.1$ and the water parameters $\nu = 8.9649$, $S_t = 3.5732$ and $K = 4.1516$ with $T_t = 20\,^{\circ}C$ and $a = 5.0cm$.

Chapter 4

Fluid Flow

4.1 Fluid Motion Equations

In order to obtain a more accurate and realistic model of the freezing of a liquid, the fluid motion in the closed region ahead of the phase change front B_p needs to be included (see figure 3.1). The extension of the method of the previous chapter to include fluid flow ahead of the phase change front is the subject of this chapter. The present chapter will consist of a number of sections. In the first section we will derive the equations governing the fluid flow ahead of the phase change front. These equations are derived from the Navier-Stokes equation for a viscous Boussinesq fluid. Once the governing equations are derived, a numerical scheme for this solution in a two-dimensional region will be outlined, this numerical scheme being a finite-difference scheme. It will then be shown how the numerical solution for the fluid flow in the liquid region ahead of the phase change front can be coupled with the boundary integral solutions of Chapter 3 for the heat flow in the solid region behind the phase change front. Solutions obtained using the numerical method of this chapter will be discussed in section 4.3.

The fluid flow problem considered in this chapter is as follows. Let us consider the freezing of the liquid contained in an arbitrary region R. Inside the region R, there will be a moving phase change front denoted by B_p and the equations for fluid motion will be applied ahead of this moving boundary, in the liquid region of R. In the following, dimensional variables will be denoted by a tilde, for example $\tilde{\underline{u}}$ for the fluid velocity. Then maintaining the notation presented for the temperature T in the previous chapter, the equation governing the heat flow in the solid phase is again

$$\frac{\partial \tilde{T}_s}{\partial \tilde{t}} = \tilde{D}_s \tilde{\nabla}^2 \tilde{T}_s, \tag{4.1}$$

where $\tilde{D}_s$ is the thermal diffusivity of the solid phase.

For the liquid phase, the temperature distribution is no longer governed by the

heat equation alone since account is now being taken of fluid motion. The Navier-Stokes equation will be used to describe the motion of the fluid. In the present work it is found convenient to use the vorticity-streamfunction formulation of the Navier-Stokes equations, as in Moore and Weiss [39], rather than using the velocity-pressure formulation, (see Batchelor [3]). A detailed derivation of the vorticity-streamfunction formulation of the Navier-Stokes equation can be found in Batchelor [3] and in Drazin and Reid [22].

The fluid is assumed to be a Boussinesq fluid. The Boussinesq approximation is valid when the temperature, and hence density, variations are small, and assumes that density variations are only significant in the buoyancy terms in the Navier-Stokes equation. This assumption is made because it is these buoyancy terms which are driving the flow. In particular, the density is assumed to be constant in the continuity equation.

In a Boussinesq fluid the velocity $\underline{\tilde{u}}$ therefore satisfies the Navier-Stokes equation

$$\tilde{\rho}_0 \left\{ \frac{\partial \underline{\tilde{u}}}{\partial \tilde{t}} + \left(\underline{\tilde{u}} \cdot \tilde{\nabla} \right) \underline{\tilde{u}} \right\} = -\tilde{\nabla} \tilde{P} + \tilde{\rho}\, \underline{\tilde{g}} + \tilde{\rho}_0 \tilde{\nu}_l \tilde{\nabla}^2 \underline{\tilde{u}} \tag{4.2}$$

and the incompressibility condition

$$\tilde{\nabla} \cdot \underline{\tilde{u}} = 0, \tag{4.3}$$

where $\tilde{P}$ is the pressure, $\underline{\tilde{g}}$ is the gravitational acceleration and $\tilde{\nu}_l$ is the kinematic viscosity of the fluid. The equation of state is, for the moment, assumed to be

$$\tilde{\rho}\left(\tilde{T}_l\right) = \tilde{\rho}_0 \left[1 - \tilde{\alpha}_l \left(\tilde{T}_l - \tilde{T}_{lr} \right) \right], \tag{4.4}$$

where the density $\tilde{\rho}$ has the value $\tilde{\rho}_0$ when the temperature $\tilde{T}_l$ is equal to $\tilde{T}_{lr}$ and $\tilde{\alpha}_l$ is the coefficient of thermal expansion. This equation simply says that the density $\tilde{\rho}$ is varying linearly as a function of the liquid temperature $\tilde{T}_l$. This linear relation is a valid approximation to a more general equation of state when the temperature variation is small $\left(\text{i.e. } |\tilde{\alpha}_l(\tilde{T}_l - \tilde{T}_{lr})| \ll 1\right)$. The pressure can be eliminated from the Navier-Stokes equation (4.2) by taking its curl, which gives

$$\frac{\partial \tilde{\omega}}{\partial \tilde{t}} = \tilde{\nabla} \times (\underline{\tilde{u}} \times \underline{\tilde{\omega}}) - \tilde{\alpha}_l \tilde{\nabla} \tilde{T}_l \times \underline{\tilde{g}} + \tilde{\nu}_l \tilde{\nabla}^2 \underline{\tilde{\omega}} \tag{4.5}$$

is obtained. This form of the Navier-Stokes equation is called the Helmholtz vorticity equation, where $\underline{\tilde{\omega}} = \tilde{\nabla} \times \underline{\tilde{u}}$ is called the vorticity of the fluid. Adding heat convection to the heat equation (3.2) of Chapter 3 for the liquid results in the convection-diffusion equation

$$\frac{\partial \tilde{T}_l}{\partial \tilde{t}} = -\tilde{\nabla} \cdot \left(\tilde{T}_l \underline{\tilde{u}} \right) + \tilde{D}_l \tilde{\nabla}^2 \tilde{T}_l \tag{4.6}$$

for heat flow in the liquid phase, where $\tilde{D}_l$ is the thermal diffusivity of the liquid phase.

In the case of the two-dimensional convection to be considered in the present work, the Cartesian axes are chosen with $\tilde{z}$ vertical and $\tilde{x}$ horizontal, so that all flow is confined to the $\tilde{x} - \tilde{z}$ plane and is independent of $\tilde{y}$. Hence the velocity and vorticity fields are given in components by

$$\underline{\tilde{u}} = (\tilde{u}, 0, \tilde{w}) \quad \text{and} \quad \underline{\tilde{\omega}} = (0, \tilde{\omega}, 0) \tag{4.7}$$

respectively, while, from the incompressibility condition (4.3), there exists a streamfunction $\tilde{\psi}$ such that

$$\tilde{u} = -\frac{\partial \tilde{\psi}}{\partial \tilde{z}} \quad \text{and} \quad \tilde{w} = \frac{\partial \tilde{\psi}}{\partial \tilde{x}}. \tag{4.8}$$

Since $\tilde{\omega} = \tilde{\nabla} \times \underline{\tilde{u}}$, the vorticity is then related to the streamfunction by

$$\tilde{\omega} = -\tilde{\nabla}^2 \tilde{\psi}. \tag{4.9}$$

Using standard vector calculus relations, the Helmholtz vorticity equation (4.5) simplifies to

$$\frac{\partial \tilde{\omega}}{\partial \tilde{t}} = -\tilde{\nabla} \cdot (\tilde{\omega}\, \underline{\tilde{u}}) - \tilde{g}\, \tilde{\alpha}_l \frac{\partial \tilde{T}_l}{\partial \tilde{x}} + \tilde{\nu}_l \tilde{\nabla}^2 \tilde{\omega} \tag{4.10}$$

for the two-dimensional flow considered here.

The equations governing the fluid flow in the liquid region and the heat flow in the solid region will now be made non-dimensional. Non-dimensional variables will be denoted by plain symbols without tildes. In particular, a time unit based on a time scale for buoyancy is used. Dimensionless variables for the space, time and temperature scales are then

$$(x, z) = \frac{(\tilde{x}, \tilde{z})}{\tilde{d}}, \quad t = \sqrt{\frac{\tilde{g}\, \tilde{\alpha}_l \tilde{T}_t}{\tilde{d}}}\, \tilde{t} = \frac{\tilde{t}}{\tilde{\theta}_l}, \quad T_l = \frac{\tilde{T}_l - \tilde{T}_{lf}}{\tilde{T}_t}, \tag{4.11}$$

respectively. Here $\tilde{d}$ is a typical length scale for the region R, $\tilde{T}_{lf}$ is the fusion temperature of the liquid phase and $\tilde{T}_t$ is a typical temperature of the initial temperature distribution. In addition, dimensionless variables for the vorticity and the streamfunction are given by

$$\omega = \tilde{\theta}_l\, \tilde{\omega} \quad \text{and} \quad \psi = \frac{\tilde{\theta}_l}{\tilde{d}^2}\, \tilde{\psi} \tag{4.12}$$

respectively.

The length, time and temperature scales can be combined to form the Rayleigh and Prandtl numbers, given by

$$Ra = \frac{\tilde{g}\, \tilde{\alpha}_l \tilde{T}_t \tilde{d}^3}{\tilde{D}_l \tilde{\nu}_l} \quad \text{and} \quad Pr = \frac{\tilde{\nu}_l}{\tilde{D}_l} \tag{4.13}$$

respectively. In terms of the Rayleigh and Prandtl numbers, the non-dimensional velocity, thermal diffusivity and viscosity are

$$\underline{u} = \frac{\tilde{d}\,\underline{\tilde{u}}}{\tilde{D}_l\sqrt{Pr\,Ra}}, \quad D_l = \frac{1}{\sqrt{Pr\,Ra}} \quad \text{and} \quad \nu_l = \sqrt{\frac{Pr}{Ra}}. \tag{4.14}$$

The Rayleigh number Ra is a ratio of the destabilising effects of buoyancy to the stabilising effects of diffusion and dissipation. Thus, for high values of the Rayleigh number, buoyancy dominates and the stationary fluid state with heat propagation by diffusion alone is unstable and the fluid starts to convect. However, for low values of the Rayleigh number, diffusion dominates and the state with the fluid stationary remains stable and the heat flows by diffusion alone. There then exists a critical Rayleigh number Ra_c above which the stationary diffusion of heat is unstable (see Acheson [2] and Drazin & Reid [22]). The choice of boundary conditions can also have an effect in determining the value of the critical Rayleigh Number Ra_c. The Prandtl number is a ratio of the fluid's capacity to diffuse momentum as compared with its capacity to diffuse heat. If the Prandtl number is high, then vorticity diffuses faster than heat, but if it is small, then the diffusion of heat dominates the fluid flow. Expressing the velocity, thermal diffusivity and viscosity in this form enables the effects of the values of the Rayleigh and Prandtl numbers on the resulting fluid flow to be easily seen.

The governing equations (4.6), (4.9) and (4.10) for the fluid flow can then be written in terms of non-dimensional variables as

$$\frac{\partial T_l}{\partial t} = -\nabla\cdot(T_l\,\underline{u}) + D_l\nabla^2 T_l \tag{4.15}$$

$$\frac{\partial \omega}{\partial t} = -\nabla\cdot(\omega\,\underline{u}) - \frac{\partial T_l}{\partial x} + \nu_l\nabla^2\omega \tag{4.16}$$

and

$$\nabla^2\psi = -\omega. \tag{4.17}$$

Using the non-dimensional variables (4.11), equation (4.1) for the temperature of the solid region behind the phase change front is

$$\frac{\partial T_s}{\partial t} = D_s\,\nabla^2 T_s, \tag{4.18}$$

where

$$D_s = \frac{\tilde{D}_s\tilde{\theta}_l}{\tilde{d}^2} \tag{4.19}$$

is the non-dimensional thermal diffusivity of the solid.

The equations for the fluid motion in the liquid phase (4.15), (4.16) and (4.17), along with the heat equation (4.18) in the solid phase, are not enough on their own to fully describe the freezing of the region R. The liquid and solid phases

are connected by the Stefan condition at the phase change front B_p. In a similar manner to that of Chapter 3, it can be shown that the non-dimensional Stefan condition is

$$K\frac{\partial T_s}{\partial n} - \frac{\partial T_l}{\partial n} = S_t\,\underline{n}\cdot\underline{V} \tag{4.20}$$

on the moving phase change front B_p. Here $\underline{n}$ is the outward unit normal to B_p, $\underline{V}$ is the velocity of B_p and the non-dimensional thermal conductivity and Stefan number are given by

$$K = \frac{\tilde{K}_s}{\tilde{K}_l} \quad \text{and} \quad S_t = \frac{\tilde{\rho}\,\tilde{L}\,\tilde{d}^{\,2}}{\tilde{T}_t\,\tilde{K}_l\,\tilde{\theta}_l} \tag{4.21}$$

respectively. The numerical procedure used to solve the fluid flow equations in the liquid phase along with the suitably scaled heat equation in the solid phase is presented in section 4.2.

4.1.1 Density of Water

In the problems under consideration in section 4.3, we shall be specifically concerned with the freezing of water. For the purposes of modelling the freezing of water with fluid motion in the liquid phase, it should be noted that the density of water displays the peculiar characteristic that in the solid state (ice) the density is less than that of the liquid state, and furthermore the density of water is not a linear function of temperature. A detailed explanation of this phenomena is given in Fletcher [25]. In simple terms, when ice melts to form water the structure of the molecular lattice becomes less orderly, producing an increase in density. This effect becomes dominant at a temperature of $3.98\,^{\circ}C$ where water attains its maximum density. As the temperature of the water is raised, one might expect the collapse of molecular structure to continue. There is, however, an opposing effect. The higher the temperature, the more the atoms get agitated, moving individual molecules of water further apart. Above $3.98\,^{\circ}C$ the kinetic motion of the atoms dominates and the density is a monotonically decreasing function of temperature.

In the derivation of the equations for fluid motion outlined in section 4.1, the assumption was made that any change in the density of the fluid was linear in temperature; see the equation of state (4.4). However, figure 4.1 shows that a quadratic profile for the density as a function of temperature would provide a better description in the case of water. Therefore for water, the equation of state (4.4) given in the previous section, is replaced by the expression

$$\tilde{\rho}\left(\tilde{T}_l\right) = \tilde{\rho}_0\left[1 - \tilde{\alpha_q}\left(\tilde{T}_l - \tilde{T}_{lr}\right)^2\right], \tag{4.22}$$

where the density $\tilde{\rho}$ has the value $\tilde{\rho}_0$ when the temperature $\tilde{T}_l$ is equal to $\tilde{T}_{lr}$ and $\tilde{\alpha_q}$ is the coefficient of thermal expansion; see the CRC tables [17]. This

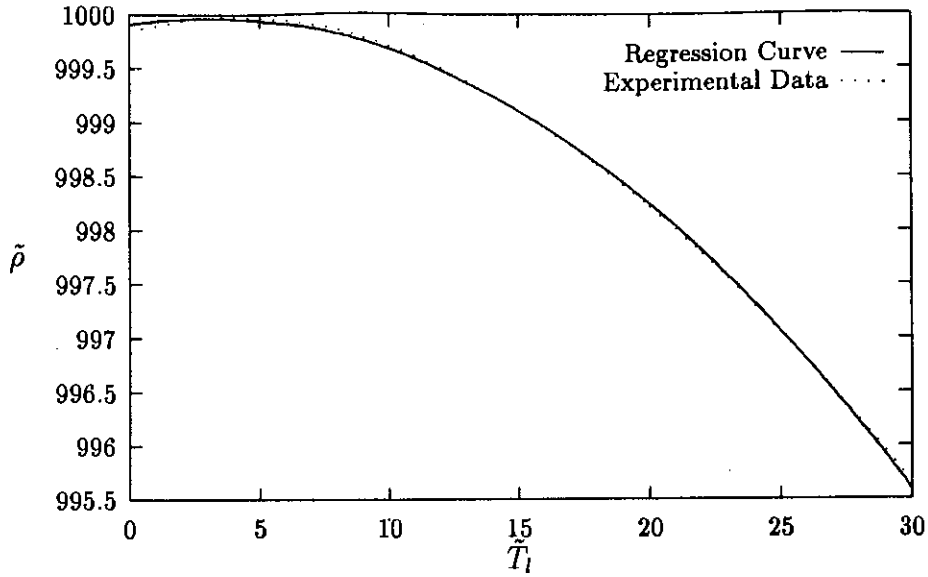

Figure 4.1: Comparison of experimental data taken from CRC tables [17] and quadratic fit generated by multiple regression

equation of state simply says that the density of water $\tilde{\rho}$ is varying quadratically as a function of the liquid temperature $\tilde{T}_l$. Using this new equation of state (4.22) with quadratic density dependence and proceeding in a similar manner as in section 4.1 with the linear equation of state, the forcing term

$$-\tilde{g}\,\tilde{\alpha}_l \frac{\partial \tilde{T}_l}{\partial \tilde{x}} \tag{4.23}$$

in the Helmholtz vorticity equation (4.10) is replaced by

$$-\tilde{g}\,\tilde{\alpha}_q \frac{\partial}{\partial \tilde{x}} \left(\tilde{T}_l - \tilde{T}_{lr}\right)^2 . \tag{4.24}$$

The dimensional Helmholtz vorticity equation for water is then

$$\frac{\partial \tilde{\omega}}{\partial \tilde{t}} = -\tilde{\nabla} \cdot (\tilde{\omega}\,\underline{\tilde{u}}) - \tilde{g}\,\tilde{\alpha}_q \frac{\partial}{\partial \tilde{x}} \left(\tilde{T}_l - \tilde{T}_{lr}\right)^2 + \tilde{\nu}_l \tilde{\nabla}^2 \tilde{\omega} . \tag{4.25}$$

The units for $\tilde{\alpha}_q$ in the quadratic equation of state (4.22) for water are different to the units for $\tilde{\alpha}_l$ in the linear equation of state (4.4). These different units mean that the scales used to form non-dimensional variables need to be changed when the water equation of state is used. In detail, when the water equation of state is used, the non-dimensional time is given by

$$t = \sqrt{\frac{\tilde{g}\,\tilde{\alpha}_q \tilde{T}_t^2}{\tilde{d}}}\,\tilde{t} = \frac{\tilde{t}}{\tilde{\theta}_q} \tag{4.26}$$

and the dimensionless variables for space and temperature remain as before as

$$(x, z) = \frac{(\tilde{x}, \tilde{z})}{\tilde{d}} \quad \text{and} \quad T_l = \frac{\tilde{T}_l - \tilde{T}_{lf}}{\tilde{T}_t} \tag{4.27}$$

respectively. The vorticity and the streamfunction in dimensionless variables are now given by

$$\omega = \tilde{\theta}_q \tilde{\omega} \quad \text{and} \quad \psi = \frac{\tilde{\theta}_q}{\tilde{d}^2} \tilde{\psi} \tag{4.28}$$

respectively. The new time scale together with the length and temperature scales can again be combined to form the Rayleigh and Prandtl numbers

$$Ra = \frac{\tilde{g}\,\tilde{\alpha}_q\,\tilde{T}_t^2\,\tilde{d}^3}{\tilde{D}_l\,\tilde{\nu}_l} \quad \text{and} \quad Pr = \frac{\tilde{\nu}_l}{\tilde{D}_l}. \tag{4.29}$$

As in section 4.1, in terms of the Rayleigh and Prandtl numbers the non-dimensional velocity, thermal diffusivity and kinematic viscosity are given by

$$\underline{u} = \frac{\tilde{d}\,\underline{\tilde{u}}}{\tilde{D}_l\sqrt{Pr\,Ra}}, \quad D_l = \frac{1}{\sqrt{Pr\,Ra}} \quad \text{and} \quad \nu_l = \sqrt{\frac{Pr}{Ra}}. \tag{4.30}$$

The governing equations for fluid flow with the water equation of state, consisting of the temperature equation (4.6), the Helmholtz vorticity equation (4.25) and equation (4.9) for the streamfunction, can then be written in terms of these new non-dimensional variables as

$$\frac{\partial T_l}{\partial t} = -\nabla\cdot(T_l\,\underline{u}) + D_l\nabla^2 T_l \tag{4.31}$$

$$\frac{\partial \omega}{\partial t} = -\nabla\cdot(\omega\,\underline{u}) - \frac{\partial}{\partial x}(T_l - T_{lr})^2 + \nu_l\nabla^2\omega \tag{4.32}$$

and

$$\nabla^2\psi = -\omega. \tag{4.33}$$

Using the non-dimensional variables for time, space and temperature equations (4.26) and (4.27) respectively, the non-dimensional form for equation (4.1) for the temperature of the solid region behind the phase change front is

$$\frac{\partial T_s}{\partial t} = D_s\nabla^2 T_s, \tag{4.34}$$

where

$$D_s = \frac{\tilde{D}_s\,\tilde{\theta}_q}{\tilde{d}^2} \tag{4.35}$$

is the non-dimensional thermal diffusivity of the solid. In terms of the new non-dimensional variables, the Stefan condition (4.20) is

$$K\frac{\partial T_s}{\partial n} - \frac{\partial T_l}{\partial n} = S_t\,\underline{n}\cdot\underline{V} \tag{4.36}$$

on the moving phase change front B_p. The non-dimensional thermal conductivity and Stefan number are given by

$$K = \frac{\tilde{K}_s}{\tilde{K}_l} \quad \text{and} \quad S_t = \frac{\tilde{\rho}\,\tilde{L}\,\tilde{d}^2}{\tilde{T}_t\,\tilde{K}_l\,\tilde{\theta}_q} \tag{4.37}$$

respectively.

Figure 4.1 clearly indicates a nonlinear dependence of water density on temperature $\tilde{T}_l$. We approximate this relationship by fitting a second order polynomial to the experimental data using linear regression. The experimental data was obtained from the CRC tables [17] at temperature intervals of $0.1\,^{\circ}C$ up to $11\,^{\circ}C$ and thereafter in increments of $1\,^{\circ}C$ up to $30\,^{\circ}C$, producing

$$\tilde{\rho}\left(\tilde{T}_l\right) \approx \left[999.963641 - 6.296541 \times 10^{-3}\left(\tilde{T}_l - 3.552573\right)^2\right] kg\,m^{-3}. \quad (4.38)$$

The dimensional forcing term in the Helmholtz vorticity equation therefore is (4.24) with $\tilde{\alpha}_q = 6.296770 \times 10^{-6}\,{}^{\circ}K^{-2}$. In the case of water the reference temperature $\tilde{T}_{lr}$ for this forcing term is $3.552573\,^{\circ}C$. Using the non-dimensionalisations for space and temperature (4.27), along with (4.26) for time and (4.28) for the vorticity, the non-dimensional Helmholtz vorticity equation (4.32), which holds for a quadratic dependence of fluid density on temperature, becomes

$$\frac{\partial \omega}{\partial t} = -\nabla \cdot (\omega\, \underline{u}) - \frac{\partial}{\partial x}\left(T_l - 0.355257\right)^2 + \nu_l \nabla^2 \omega \quad (4.39)$$

in the case of water. For water, the fusion temperature is $\tilde{T}_{lf} = 0\,^{\circ}C$ and the characteristic temperature scale for the initial temperature distribution is taken to be $\tilde{T}_t = 10\,^{\circ}C$.

The non-dimensional governing equations for fluid motion with a quadratic dependence of fluid density on temperature will provide a better model of the freezing of water than those with the linear equation of state. Numerical results obtained using the quadratic equation of state will be presented in section 4.3. The equations with the linear equation of state will be used for comparison with previous results only.

4.1.2 Formulation

In this section, a description of the region that will be used in the present work for two-dimensional freezing problems will be given, along with the relevant boundary conditions for the liquid and solid phases.

Let us consider the freezing of an infinite cylinder with square cross-section R. At a general time t, the region R has a fixed boundary B_f and inside the region R, a moving phase change front B_p. Ahead of the phase change front, the material is taken to be in the liquid phase and behind the phase change front, in the solid phase. This region is the same as the one used for the problems discussed in section 3.4. The temperature distribution in the solid phase, $T_s(\underline{r}, t)$, is described by the heat equation (4.18). In the liquid phase however, the equations of fluid

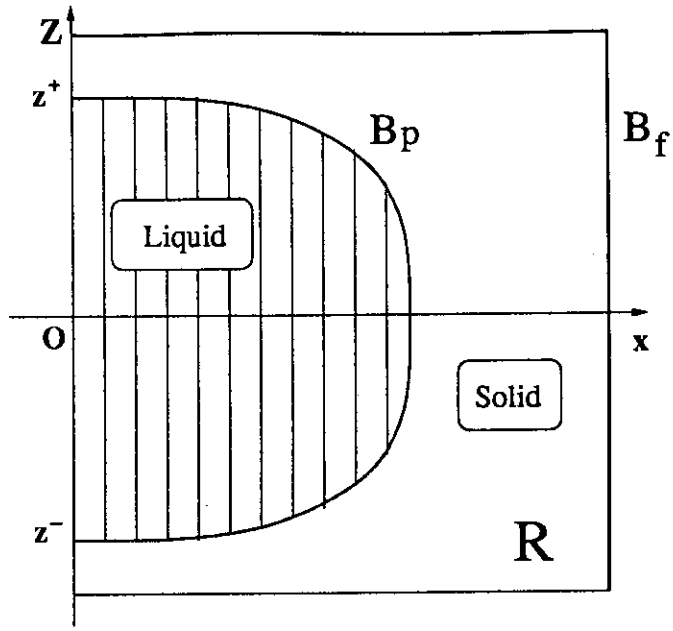

Figure 4.2: Region R with fixed boundary B_f and phase change front B_p

motion are applied. For the linear equation of state, the governing equations for the liquid phase are (4.15) for the temperature $T_l(\underline{r},t)$, (4.16) for the vorticity $\omega(\underline{r},t)$ and (4.17) for the streamfunction $\psi(\underline{r},t)$. For the quadratic equation of state the relevant equations are (4.31) for the temperature $T_l(\underline{r},t)$; (4.39) for the vorticity $\omega(\underline{r},t)$ and (4.33) for the streamfunction $\psi(\underline{r},t)$.

In general one would have a Newton cooling boundary condition on the fixed boundary B_f (see section 3.1), but for simplicity and comparison with the results of Chapter 3 (section 3.4), a fixed temperature boundary condition $T_s = T_{sb}$ is imposed. Initially the region is totally filled with liquid with some temperature distribution, so that the initial condition is $T_l(\underline{r},0) = T_{l0}(\underline{r})$ in R. In the examples considered in the present work, T_{l0} is taken to be a positive constant. On the moving phase change front B_p, the freezing temperature is scaled to be zero, so that $T_s = T_l = 0$ on B_p.

The streamfunction ψ is taken to be zero on the phase change front B_p so that the normal velocity of the fluid is zero on the front. Taking the normal velocity to be zero on the moving boundary might, at first sight, seem strange, until it is recalled how the phase change front is formed. The phase change front moves from one position to the next by all the fluid in a region next to the front freezing. The front is therefore not moving by pushing the fluid ahead of it, and so the normal velocity of the fluid is zero on the phase change front. The phase change front, being composed of ice, is of course a rigid boundary for which the no-slip condition applies. The no-slip boundary condition (see Acheson [2] and Drazin

& Reid [22]) is then applies on the phase change front. The boundary conditions for the streamfunction ψ are therefore those proposed by Hirasaki and Hellums [32]; namely

$$\psi_{t_i} = 0 \quad \text{and} \quad \frac{\partial \psi_n}{\partial n} = 0 \quad \text{on } B_f. \tag{4.40}$$

Here the subscripts t_i and n refer to the tangential and normal directions. The value of the vorticity ω on the phase change front B_p can be obtained from the second of these conditions on ψ and Poisson's equation relating ψ and ω, namely equation (4.17) for the linear equation of state or equation (4.33) for the quadratic equation of state. Woods [56] showed that these equations yield

$$\omega_b = \frac{-3(\psi_{b+1} - \psi_b)}{(\Delta n)^2} - \frac{\omega_{b+1}}{2} \tag{4.41}$$

on a solid boundary, where the subscripts b and $b+1$ denote mesh points on the boundary and one mesh length Δn away from the boundary in the normal direction. In general ψ_b is an arbitrary constant, but is taken to be zero here.

Due to the symmetries of the square cross-section of the region R, the region can be reduced to that shown in figure 4.2 for a fixed temperature initial condition and for T_s a constant on the boundary. The horizontal line of symmetry for the square which existed for the freezing problems of Chapter 3 no longer exists due to the influence of gravity in the vertical direction. Along the z axis between z^+ and z^- (see figure 4.2), the vorticity and streamfunction take the value zero since this is a fixed stress-free fluid boundary. Furthermore the temperature of the fluid along $[z^-, z^+]$ satisfies the symmetry condition $\partial T_l / \partial x = 0$.

4.2 Numerical Scheme

In this section a detailed account of the numerical scheme that is employed to solve the governing equations of the fluid motion which consist of (4.15) to (4.17) for the linear equation of state, or (4.31) to (4.33) for the quadratic equation of state, is given. The numerical scheme used is a finite-difference method and is based on the methods presented by Moore, Peckover & Weiss [38] and Moore & Weiss [39, 40]. Furthermore, a description of how the numerical scheme may be adapted to take account of the quadratic equation of state that occurs when water is frozen is included (see sub-section 4.1.1). Finally, the procedure for numerically solving two-phase Stefan problems with fluid flow is presented. This new numerical method is an extension of that presented in Chapter 3 to include the fluid motion ahead of the phase change front.

The governing equations for fluid motion for the temperature T_l, vorticity ω and streamfunction ψ are solved numerically on a rectangular grid ahead of the

phase change front B_p; see figure 4.2. The grid is applied over the entire region R. Initially at time $t = 0$, the phase change front B_p and the fixed boundary B_f coincide. However, at subsequent times $t > 0$, the phase change front lies between the fixed boundary B_f and the centre of the region R. Hence at times $t > 0$, grid points can be behind the phase change front. As the fluid flow does not need to be calculated behind the phase change front each point of the grid that lies either ahead of or on the phase change front B_p is retained as an active grid point. The remaining grid points that lie behind the phase change front are considered inactive. In this way the grid of points on which the fluid motion is calculated is reduced at each time step until the region R consists entirely of solid with no liquid phase remaining. If the space variables are simply discretised by equally spaced grid points, then at any particular time step, with time $t > 0$, the phase change front could fall between grid points. To overcome this, at each time step the grid solved on is extended to include points on the phase change front. The extra distances from the closest grid points to the phase change front itself are $\varepsilon\,\Delta x$ in the x direction and $\beta_1\,\Delta z$ and $\beta_2\,\Delta z$ in the z direction. The values of ε, β_1 and β_2 will in general vary around the edge of the active grid. The orientation of $\varepsilon\,\Delta x$, $\beta_1\,\Delta z$ and $\beta_2\,\Delta z$ are shown in figure 4.3. Each of ε, β_1 and β_2 lie in the range $(0, 1]$. There are no extra points required for grid points to the left in the x direction since the region R has been reduced by symmetry (see figure 4.2) and the left hand boundary of the computation region is the z axis, which is fixed. This formulation of the spatial discretisation assumes, to some degree, that the moving phase change front B_p is suitably convex. If this is not the case, then a new strategy to include points on the phase change front must be devised. For the problems considered in section 4.3 the meshing strategy outlined above is sufficient, since for stable Stefan problems the phase change front is convex.

Let us now derive finite difference approximations on a non-uniform mesh for the partial derivatives needed for the fluid flow equations. These approximations will not be used across the phase change front, where there is a discontinuity in temperature derivative, and consequently the assumptions on the properties of the function are valid. Using the parameters ε, β_1 and β_2, the Taylor series expansions about the point (x, z) of an arbitrary function $f(x, z)$ with continuous and single valued derivatives are given by the following expressions in the x direction

$$\begin{aligned} f(x + \varepsilon\Delta x, z) &= f(x, z) + \varepsilon\Delta x f_x(x, z) + \frac{(\varepsilon\Delta x)^2}{2!} f_{xx}(x, z) + \ldots, \\ f(x - \Delta x, z) &= f(x, z) - \Delta x f_x(x, z) + \frac{\Delta x^2}{2!} f_{xx}(x, z) + \ldots \end{aligned}$$

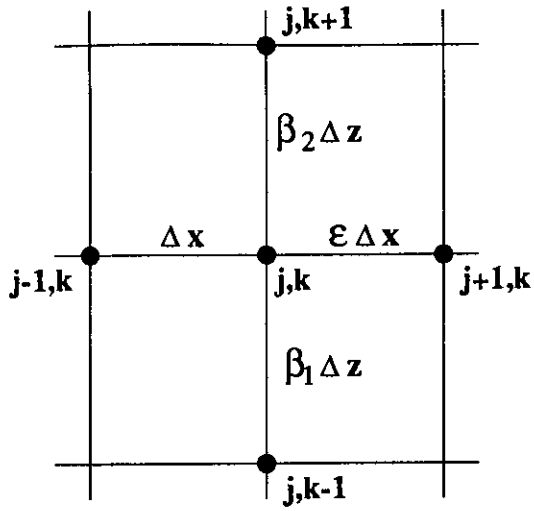

Figure 4.3: Orientation of spatial discretisation parameters ε, β_1 and β_2 around a typical point (j,k)

and

$$\begin{aligned} f(x, z+\beta_2\Delta z) &= f(x,z) + \beta_2\Delta z f_z(x,z) + \frac{(\beta_2\Delta z)^2}{2!} f_{zz}(x,z) + \ldots, \\ f(x, z-\beta_1\Delta z) &= f(x,z) - \beta_1\Delta z f_z(x,z) + \frac{(\beta_1\Delta z)^2}{2!} f_{zz}(x,z) + \ldots \end{aligned}$$

in the z direction. The Taylor series expansions in the x direction can now be combined to give second order approximations to the first and second derivatives with respect to x

$$\frac{\partial f(x,z)}{\partial x} = \frac{f(x+\varepsilon\Delta x, z) - \varepsilon^2 f(x-\Delta x, z) - (1-\varepsilon^2) f(x,z)}{\varepsilon\Delta x(1+\varepsilon)} + \mathrm{O}\left(\Delta x^2\right) \quad (4.42)$$

and

$$\begin{aligned} \frac{\partial^2 f(x,z)}{\partial x^2} = & \quad \frac{2\left[f(x+\varepsilon\Delta x, z) + \varepsilon f(x-\Delta x, z) - (1+\varepsilon) f(x,z)\right]}{\varepsilon(1+\varepsilon)\Delta x^2} \\ & + \mathrm{O}\left(\Delta x^2\right). \end{aligned} \quad (4.43)$$

In a similar manner, second order approximations to the first and second z derivatives can be found using theses Taylor series as

$$\begin{aligned} \frac{\partial f(x,z)}{\partial z} = & \quad \frac{\beta_1^2 f(x, z+\beta_2\Delta z) - \beta_2^2 f(x, z-\beta_1\Delta z)}{\beta_1\beta_2\Delta z(\beta_1+\beta_2)} \\ & - \frac{(\beta_1^2 - \beta_2^2) f(x,z)}{\beta_1\beta_2\Delta z(\beta_1+\beta_2)} + \mathrm{O}\left(\Delta z^2\right) \end{aligned} \quad (4.44)$$

and

$$\begin{aligned} \frac{\partial^2 f(x,z)}{\partial z^2} = & \quad \frac{2\left[\beta_1 f(x, z+\beta_2\Delta z) + \beta_2 f(x, z-\beta_1\Delta z)\right]}{\beta_1\beta_2(\beta_1+\beta_2)\Delta z^2} \\ & - \frac{2(\beta_1+\beta_2) f(x,z)}{\beta_1\beta_2(\beta_1+\beta_2)\Delta z^2} + \mathrm{O}\left(\Delta z^2\right). \end{aligned} \quad (4.45)$$

The spatial derivatives that occur in the governing equations for fluid motion are then approximated using these finite difference approximations.

If the arbitrary function f is also taken to be a function of time, then in a similar manner to the spatial derivatives, we can obtain

$$\frac{\partial f(x,z,t)}{\partial t} = \frac{f(x,z,t+\Delta t) - f(x,z,t)}{\Delta t} + \mathrm{O}(\Delta t) \tag{4.46}$$

as a first order approximation to the time derivatives that occur in the governing equations of fluid motion. The DuFort-Frankel method (see Smith [51] and Roberts & Weiss [47]) is then applied to the convective terms in the fluid flow equations. This method gives unconditional stability for the scheme and furthermore the order of the error for the time derivatives is reduced to $\mathrm{O}(\Delta t^2)$ which concurs with the spacial approximations.

Let us now consider in detail the numerical solution of the governing equations for fluid flow in the liquid region. Let time be discretised into intervals of length Δt, so that $t_n = n\,\Delta t$, and let the x and z directions be discretised into intervals of length $\varepsilon\,\Delta x$ and $\beta\,\Delta z$ respectively, where ε is the scaling parameter in the positive x direction and β represents either β_1 or β_2, the scaling parameters for the negative and positive z directions respectively. It is noted that $\varepsilon = \beta_1 = \beta_2 = 1$, except adjacent to the phase change front B_p. The grid points in the x and z directions are x_j, $j = 0, 1, 2, \ldots, N_x$ and z_k, $k = 0, 1, 2, \ldots, N_z$, respectively. The temperature T_l, vorticity ω and the streamfunction ψ are calculated on the mesh in space-time and are denoted at the grid points by

$$T_l(x_j, z_k, t_n) = T^n_{j,k}, \quad \omega(x_j, z_k, t_n) = \omega^n_{j,k} \quad \text{and} \quad \psi(x_j, z_k, t_n) = \psi^n_{j,k},$$

at time step n respectively.

Applying the finite difference approximations (4.42) to (4.46) to the convection-diffusion equation (4.15), the numerical approximation

$$\begin{aligned}
T^{n+1}_{j,k} = T^n_{j,k} \;+\; & \frac{2\Delta t}{1 + \frac{D_l \Delta t}{\varepsilon \Delta x^2} + \frac{D_l \Delta t}{\beta_1 \beta_2 \Delta z^2}} \left[\left(\frac{T^{n+1/2}_{j+1,k} - \varepsilon^2 T^{n+1/2}_{j-1,k} - (1-\varepsilon^2) T^{n+1/2}_{j,k}}{\varepsilon(1+\varepsilon)\Delta x} \right) \right. \\
& \times \left(\frac{\beta_1^2 \psi^{n+1/2}_{j,k+1} - \beta_2^2 \psi^{n+1/2}_{j,k-1} - (\beta_1^2 - \beta_2^2) \psi^{n+1/2}_{j,k}}{\beta_1 \beta_2 \Delta z (\beta_1 + \beta_2)} \right) \\
& - \left(\frac{\beta_1^2 T^{n+1/2}_{j,k+1} - \beta_2^2 T^{n+1/2}_{j,k-1} - (\beta_1^2 - \beta_2^2) T^{n+1/2}_{j,k}}{\beta_1 \beta_2 \Delta z (\beta_1 + \beta_2)} \right) \\
& \times \left(\frac{\psi^{n+1/2}_{j+1,k} - \varepsilon^2 \psi^{n+1/2}_{j-1,k} - (1-\varepsilon^2) \psi^{n+1/2}_{j,k}}{\varepsilon(1+\varepsilon)\Delta x} \right) \\
& + 2\,D_l \left(\frac{T^{n+1/2}_{j+1,k} + \varepsilon T^{n+1/2}_{j-1,k} - (1+\varepsilon) T^n_{j,k}}{\varepsilon(1+\varepsilon)\Delta x^2} \right)
\end{aligned}$$

$$+ \quad 2\,D_l \left(\frac{\beta_1 T_{j,k+1}^{n+1/2} + \beta_2 T_{j,k-1}^{n+1/2} - (\beta_1+\beta_2) T_{j,k}^{n}}{\beta_1\beta_2(\beta_1+\beta_2)\Delta z^2} \right) \Bigg] \tag{4.47}$$

is obtained. In a similar manner, the discretised form of the Helmholtz vorticity equation (4.16) is found as

$$\begin{aligned}
\omega_{j,k}^{n+1} = \omega_{j,k}^{n} \quad + \quad & \frac{2\Delta t}{1 + \frac{\nu_l \Delta t}{\varepsilon \Delta x^2} + \frac{\nu_l \Delta t}{\beta_1 \beta_2 \Delta z^2}} \Bigg[\left(\frac{\omega_{j+1,k}^{n+1/2} - \varepsilon^2 \omega_{j-1,k}^{n+1/2} - (1-\varepsilon^2)\omega_{j,k}^{n+1/2}}{\varepsilon(1+\varepsilon)\Delta x} \right) \\
& \times \left(\frac{\beta_1^2 \psi_{j,k+1}^{n+1/2} - \beta_2^2 \psi_{j,k-1}^{n+1/2} - (\beta_1^2 - \beta_2^2)\psi_{j,k}^{n+1/2}}{\beta_1\beta_2\Delta z(\beta_1+\beta_2)} \right) \\
& - \left(\frac{\beta_1^2 \omega_{j,k+1}^{n+1/2} - \beta_2^2 \omega_{j,k-1}^{n+1/2} - (\beta_1^2 - \beta_2^2)\omega_{j,k}^{n+1/2}}{\beta_1\beta_2\Delta z(\beta_1+\beta_2)} \right) \\
& \times \left(\frac{\psi_{j+1,k}^{n+1/2} - \varepsilon^2 \psi_{j-1,k}^{n+1/2} - (1-\varepsilon^2)\psi_{j,k}^{n+1/2}}{\varepsilon(1+\varepsilon)\Delta x} \right) \\
& - \left(\frac{T_{j+1,k}^{n+1/2} - \varepsilon^2 T_{j-1,k}^{n+1/2} - (1-\varepsilon^2) T_{j,k}^{n+1/2}}{\varepsilon\Delta x(1+\varepsilon)} \right) \\
& + \quad 2\,\nu_l \left(\frac{\omega_{j+1,k}^{n+1/2} + \varepsilon \omega_{j-1,k}^{n+1/2} - (1+\varepsilon)\omega_{j,k}^{n}}{\varepsilon(1+\varepsilon)\Delta x^2} \right) \\
& + \quad 2\,\nu_l \left(\frac{\beta_1 \omega_{j,k+1}^{n+1/2} + \beta_2 \omega_{j,k-1}^{n+1/2} - (\beta_1+\beta_2)\omega_{j,k}^{n}}{\beta_1\beta_2(\beta_1+\beta_2)\Delta z^2} \right) \Bigg] .
\end{aligned} \tag{4.48}$$

Before the finite difference equations for temperature (4.47) and vorticity (4.48) can be solved explicitly ahead of the moving phase change front (subject to any boundary conditions), the equation for the streamfunction (4.17) must also be expressed in finite difference form. The finite difference approximations (4.42) to (4.46) give that the finite difference form of equation (4.17) for the streamfunction is

$$\begin{aligned}
& \left(\frac{\psi_{j+1,k} + \varepsilon \psi_{j-1,k} - (1+\varepsilon)\psi_{j,k}}{\varepsilon\,(1+\varepsilon)\,\Delta x^2} \right) \\
+ \quad & \left(\frac{\beta_1 \psi_{j,k+1} + \beta_2 \psi_{j,k-1} - (\beta_1+\beta_2)\psi_{j,k}}{\beta_1\,\beta_2\,(\beta_1+\beta_2)\,\Delta z^2} \right) = -\frac{1}{2}\omega_{j,k}.
\end{aligned} \tag{4.49}$$

This is just the five-point Laplacian representation of Poisson's equation in terms of the scaling parameters ε, β_1 and β_2. This equation relates the values of the vorticity and the streamfunction at all points on the mesh at each time step.

Now that the equations of fluid motion have been expressed in finite difference form they can be solved numerically in the following manner. At $t = 0$ it is assumed that the temperature T_l, vorticity ω and streamfunction ψ have known initial values. The boundary conditions to be used are given in sub-section 4.1.2.

At the first intermediate fluid flow time step, time $t = 1/2\,\Delta t$, the equations for temperature (4.47) and vorticity (4.48) in the form given are not applicable, since they require information at two different time levels and currently we have information at time $t = 0$ only. To overcome this problem, the modified Euler method (2nd order Runge Kutta), see Burden, Faires and Reynolds [6], is used to provide an initial time discretisation of the temperature and vorticity equations. The discretised space derivatives in the temperature equation (4.47) and vorticity equation (4.48) are, of course, not changed. The modified Euler scheme is second order and so is compatible with the time discretisation in (4.47) and (4.48). The temperature T_l and the vorticity ω can then be calculated at time $t = 1/2\,\Delta t$. Then since we now know the values of the vorticity across the mesh from the modified Euler method, we use the streamfunction equation (4.49) to formulate a linear system of unknowns of ψ at each of the interior mesh points. This linear system takes the standard form

$$\mathbf{A}\,\underline{x} = \underline{b}, \tag{4.50}$$

where the matrix $\mathbf{A}$ is a banded matrix of coefficients of the streamfunction in (4.49), the vector $\underline{x}$ contains the unknown values of the streamfunction and the right hand side vector $\underline{b}$ contains the values of the vorticity ω at each interior point of the mesh. Since the relationship between the vorticity and the streamfunction is described by Poisson's equation (4.17), with corresponding finite difference form (4.49), the banded structure of matrix $\mathbf{A}$ will be penta diagonal. Matrix $\mathbf{A}$ has dimension $N_x \times N_z$, and so, in general, will be large. Faced with such a large linear system to solve, the most attractive method of solution is an iterative method, see [6, 18]. In the cases considered in section 4.3 it was found that successive-over-relaxation (SOR) had difficulty converging to a stable solution. For this reason a simpler iterative method was chosen to solve the linear system; the Jacobi iterative method [6, 18] which proved to be sufficient for the problems considered in section 4.3.

Now that the temperature, vorticity and streamfunction are known in the liquid phase at times $t = 0$ and $t = 1/2\,\Delta t$, the standard finite difference approximations (4.47) to (4.49) to the governing equations of fluid flow are applied at successive intervals of time of $1/2\,\Delta t$. The streamfunction equation (4.49) is solved at each time step using the Jacobi iterative method. In this manner, the fluid flow equations can be marched forward in time.

The numerical scheme presented here is based upon the formulation given in the paper by Moore, Peckover and Weiss [38]. Since they were not concerned with Stefan problems, they solve the fluid equations on an equally spaced grid, so that

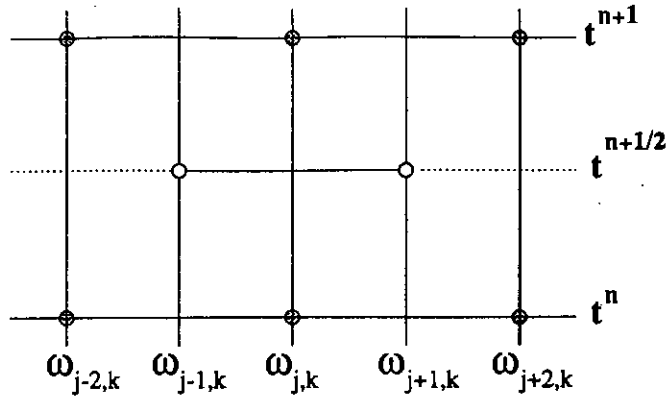

Figure 4.4: Staggered mesh on the $x - t$ plane: Known values of ω are marked with dark circles with required values of ω shown by white circles.

$\varepsilon = \beta_1 = \beta_2$ in our notation. Furthermore, they solved the finite difference forms of the fluid flow equations on a staggered mesh at each time step; see Roberts and Weiss [47]. The main advantage of adopting this strategy is that it results in the quantities T_l and ω being evaluated at only half the grid points at each time step, with a consequent decrease in storage and computation time. The idea behind this staggered mesh is as follows. Let us assume that a quantity, say the vorticity $\omega_{j,k}$, is known at times t_n and t_{n+1} and that its neighbours $\omega_{j-1,k}$ and $\omega_{j+1,k}$ are known at the intermediate time step $t_{n+1/2}$; see figure 4.4. Then from equations (4.47) to (4.49) with $\varepsilon = \beta_1 = \beta_2 = 1$, it can be seen that $\omega_{j,k}^{n+1}$ can be calculated. The same holds true for temperature $T_{j,k}$. Hence to calculate the solution at time step $n+1$, the solution has to be known at odd grid points only at time step $n + 1/2$ and even grid points only at time step n. To facilitate this, a parameter q is introduced such that $q = 2n = 0, 1, 2, \ldots$. Then for $j + k$ and q even, the temperature T_l and the vorticity ω are calculated explicitly and stored only at integral time steps. For $j + k$ and q odd, the temperature and vorticity are calculated at intermediate time steps $t_{n+1/2}$ only. However, when a staggered mesh is used, the vorticity is defined on half the mesh points at each time step only and the finite difference form (4.49) of the streamfunction equation cannot be solved. The solution for the streamfunction (4.49) is instead found by solving for the streamfunction at the grid points where the vorticity is available. Then by means of interpolation, the streamfunction can be obtained at all other grid points. This numerical procedure using a staggered mesh would seem to be a good choice. However, when there is a moving boundary, we need to add points to our mesh to incorporate the phase change front as we refine the grid. This process introduces the spatial orientation parameters ε, β_1 and β_2, and upon examination of the governing fluid equations (4.47) to (4.49), it is clear that unless $\varepsilon = \beta_1 =$

$\beta_2 = 1$ the staggered mesh method will not work. In general, the parameters ϵ, β_1 and β_2 will not all be equal to one, forcing the use of a more computationally intensive grid. Thus the finite difference approximations to the equations of fluid motion are applied across the whole active computational grid ahead of the phase change front using the method outlined previously.

4.2.1 Water Equations

In this section we present the amendments that are required to the finite difference equations when a quadratic equation of state is used.

For the examples considered in section 4.3, we are interested in modelling the freezing of water and, as was shown in sub-section 4.1.1 a quadratic equation of state provides a better model. The governing equations of fluid flow in the case of a quadratic equation of state are given by equation (4.31) for the temperature, (4.39) for the vorticity and (4.33) for the streamfunction. Following the notation introduced in section 4.2 for discretised space and time and applying the finite difference approximations (4.42) to (4.46) to the convection-diffusion and stream-function equations, we obtain the same finite difference approximations as for the linear equation of state, equations (4.47) and (4.49) respectively. However, the non-dimensional coefficients in these finite difference equations are not the same in the case of a quadratic equation of state. The appropriate forms of the coefficients are given in sub-section 4.1.1. The vorticity equation (4.39), however, contains a quadratic forcing term which can be expressed in the form

$$\frac{\partial}{\partial x}\left(T_l - 0.355257\right)^2 = 2\,\frac{\partial T_l}{\partial x}\left(T_l - 0.355277\right) . \tag{4.51}$$

Using this form of the the forcing term (4.51) and applying the approximations (4.42) to (4.46) for space and time discretisations, the finite difference approximation to the Helmholtz vorticity equation (4.39) becomes,

$$\begin{aligned}
\omega_{j,k}^{n+1} = \omega_{j,k}^{n} \;+\; & \frac{2\Delta t}{1 + \frac{\nu_l \Delta t}{\epsilon \Delta x^2} + \frac{\nu_l \Delta t}{\beta_1 \beta_2 \Delta z^2}} \left[\left(\frac{\omega_{j+1,k}^{n+1/2} - \epsilon^2 \omega_{j-1,k}^{n+1/2} - (1-\epsilon^2)\omega_{j,k}^{n+1/2}}{\epsilon(1+\epsilon)\Delta x} \right) \right. \\
& \times \left(\frac{\beta_1^2 \psi_{j,k+1}^{n+1/2} - \beta_2^2 \psi_{j,k-1}^{n+1/2} - (\beta_1^2 - \beta_2^2)\psi_{j,k}^{n+1/2}}{\beta_1 \beta_2 \Delta z (\beta_1 + \beta_2)} \right) \\
& - \left(\frac{\beta_1^2 \omega_{j,k+1}^{n+1/2} - \beta_2^2 \omega_{j,k-1}^{n+1/2} - (\beta_1^2 - \beta_2^2)\omega_{j,k}^{n+1/2}}{\beta_1 \beta_2 \Delta z (\beta_1 + \beta_2)} \right) \\
& \times \left(\frac{\psi_{j+1,k}^{n+1/2} - \epsilon^2 \psi_{j-1,k}^{n+1/2} - (1-\epsilon^2)\psi_{j,k}^{n+1/2}}{\epsilon(1+\epsilon)\Delta x} \right) \\
& - 2 \left(\frac{T_{j+1,k}^{n+1/2} - \epsilon^2 T_{j-1,k}^{n+1/2} - (1-\epsilon^2) T_{j,k}^{n+1/2}}{\epsilon \Delta x (1+\epsilon)} \right)
\end{aligned}$$

$$\times \quad \left(T_{j,k}^{n+1/2} - 0.355257\right)$$
$$+ \quad 2\nu_l \left(\frac{\omega_{j+1,k}^{n+1/2} + \varepsilon\omega_{j-1,k}^{n+1/2} - (1+\varepsilon)\omega_{j,k}^{n}}{\varepsilon(1+\varepsilon)\Delta x^2} \right)$$
$$+ \quad 2\nu_l \left(\frac{\beta_1\omega_{j,k+1}^{n+1/2} + \beta_2\omega_{j,k-1}^{n+1/2} - (\beta_1+\beta_2)\omega_{j,k}^{n}}{\beta_1\beta_2(\beta_1+\beta_2)\Delta z^2} \right) \Bigg]. \qquad (4.52)$$

It is this form of the vorticity equation, together with the corresponding equations for temperature (4.47) and (4.49) for the streamfunction that are solved in section 4.3 to model the freezing of water.

4.2.2 The Solid Phase

In Chapter 3, the strategy for solving two-phase Stefan problems was to obtain a set of coupled integral equations for the solid and liquid phases (see section 3.2), which together with the Stefan condition were solved via a boundary integral method (see section 3.3). Since we are now taking account of the fluid motion in the liquid phase of the region, the numerical strategy must be revised. Essentially, the approach will be to use the boundary integral formulation that was presented in the previous chapter for the solid phase, while the finite difference method outlined in the present chapter will be used to solve for the fluid flow in the liquid region ahead of the phase change front.

Let us suppose that the geometry of the region R, along with the boundary conditions to be used are those specified in sub-section 4.1.2. Ahead of the moving boundary B_p, in the liquid phase, we require the solution to the equations of fluid motion. In the case of density being linearly dependent on temperature this would entail solving equations (4.15) for the temperature, (4.16) for the vorticity and (4.17) for the streamfunction. For quadratic density dependence on temperature however, the solution of equations (4.31) for the temperature, (4.39) for the vorticity and (4.33) for the streamfunction are required. In the solid phase, behind the phase change front, the solution of the heat equation (4.18), with the Stefan condition (4.20) providing a link between the two phases at the moving boundary, is required in the linear case. While for quadratic density dependence the heat equation (4.34) and the Stefan condition (4.36) are required.

The integral equation describing the temperature distribution in the solid phase behind the phase change front,

$$-\lambda T_s(\underline{r},t) = D_s \int_0^{t+0} \int_{B_f} \left(T_s' \frac{\partial G_s}{\partial n'} - G_s \frac{\partial T_s'}{\partial n'} \right) ds'dt' \qquad (4.53)$$
$$-D_s \int_{B_s} G_s(\underline{r},\underline{r}',t,f(x',z'))\, \nabla' T_s' \cdot \nabla' f|_{t'=f(x',z')}\, dx'\, dz' ,$$

is obtained from the governing equation of heat flow in the solid phase, by utilising the Green's function formulation of section 3.2. The requirements for the solution of integral equation (4.53) are threefold. Firstly, since equation (4.53) involves both the temperature T_s and the normal temperature gradient $\partial T_s/\partial n$ on the fixed boundary B_f and only the temperature or normal temperature gradient is known at each point, the unknown boundary data T_s or $\partial T_s/\partial n$ must be determined as part of the solution process. In the problem specified in sub-section 4.1.2, a fixed boundary temperature $T_s = T_{sb}$ is imposed on B_f. Hence the normal temperature gradients form the unknowns on the fixed boundary and must be determined. Furthermore, the position of the phase change front B_p is also required and will be determined by the same process described in section 3.3. That is, for each new front position we will provide an initial estimate of the position of the front by extrapolation and repeatedly refine this estimate until it falls within an accepted tolerance. Finally, the temperature gradients $\nabla' T_s' \cdot \nabla' f|_{t'=f(x',z')}$ behind the phase change front are required. The numerical formulation of the solution of the integral equation for the temperature distribution in the solid phase (4.53) will follow that presented in section 3.3.

The way in which we obtain the gradients $\nabla' T_s' \cdot \nabla' f|_{t'=f(x',z')}$ forms one of the key differences between the treatment of the integral equations given in section 3.3 and the procedure to be detailed here. These unknown gradients are related to the same gradients ahead of the phase change front by the Stefan condition (4.20), from which the relationship

$$K \nabla' T_s' \cdot \nabla' f = S_t + \nabla' T_l' \cdot \nabla' f, \tag{4.54}$$

is obtained, where S_t is the Stefan number (4.21). A similar expression is obtained in the case of a quadratic equation of state. The gradients $\nabla' T_l' \cdot \nabla' f$ that occur explicitly in the integral equation

$$\begin{aligned} -\lambda T_l(\underline{r}, t) \;=\; & -\int_{S_0} T_l'(\underline{r}', 0)\, G_l(\underline{r}, \underline{r}', t, 0)\, dx'\, dz' \\ & + \int_{B_s} G_l(\underline{r}, \underline{r}', t, f(x', z'))\, \nabla' T_l' \cdot \nabla' f|_{t'=f(x',z')}\, dx'\, dz' \end{aligned} \tag{4.55}$$

that was derived in section 3.2 to describe the temperature distribution ahead of the phase change front are obtained by solving a linear system of equations (see section 3.3). However, when we consider the equations of fluid motion, these gradients do not appear explicitly in the convection-diffusion equation that describes the temperature distribution in the liquid phase. These gradients for the liquid phase when there is fluid flow can be expressed as

$$\nabla' T_l' \cdot \nabla' f = |\nabla' f|\, (\underline{n} \cdot \nabla' T_l'), \tag{4.56}$$

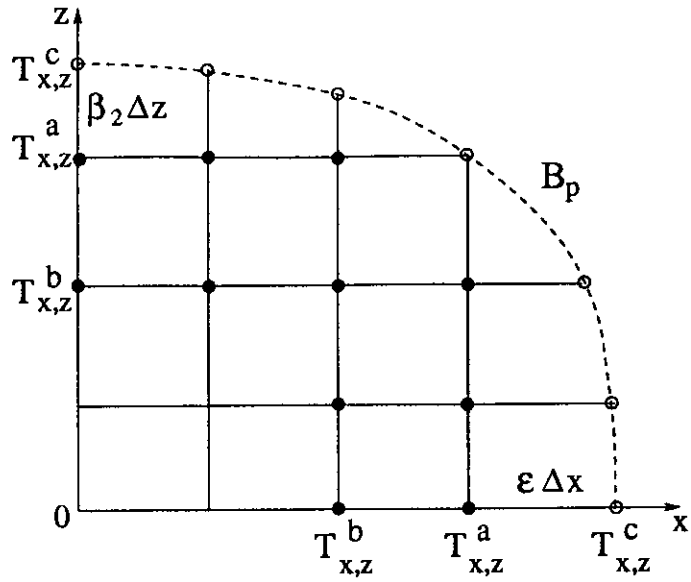

Figure 4.5: A typical space mesh in the liquid region (first quadrant) spatial derivatives $T^{a}_{x,z}$ and $T^{b}_{x,z}$ are evaluated on the dark circles

where $\underline{n}$ is the outward unit normal to the phase change front. Using expression (3.25) the normal velocity of the phase change front is found to be

$$\underline{n} \cdot \underline{V} = \frac{1}{|\nabla' f|}, \tag{4.57}$$

where $\underline{V}$ is the velocity of the phase change front (see section 3.2), we can evaluate the unknown gradients at the phase change front B_p, as is now outlined.

The following procedure is employed to obtain the gradients $\nabla' T_l' \cdot \nabla' f$ when there is fluid motion in the liquid phase. We require the gradients $\nabla' T_l' \cdot \nabla' f$ to be available at each grid point on the moving phase change front B_p. In the integral formulation of the last chapter, the grid points on the phase change front for the solid and liquid regions matched up exactly. However, if we use the spatial discretisation proposed for the equations of fluid motion, there is no guarantee that mesh points in the solid phase will coincide with the mesh points of the liquid phase at the moving phase change front. Thus at a given time t after the mesh for the fluid motion equations has been reduced to active and inactive grid points, the following strategy is employed. We evaluate the spatial derivatives

$$\frac{\partial T_l}{\partial x} \quad \text{and} \quad \frac{\partial T_l}{\partial z} \tag{4.58}$$

using the finite difference approximations (4.42) and (4.44) respectively at the nearest two grid points closest to the moving phase change front B_p. A typical distribution of points is shown in figure 4.5 for the first quadrant. At the points

where the phase change front intersects the z axes,

$$\frac{\partial T_l}{\partial x} = 0$$

due to symmetry; see sub-section 4.1.2. Once the derivatives have been evaluated at each of the required interior fluid flow mesh points, linear extrapolation is employed to obtain the value of the given derivative at the mesh points on the moving phase change front B_p. In general this is achieved by applying the following formulae for the x and z derivatives

$$\frac{\partial T_l^{\mathrm{c}}}{\partial x} = \frac{\partial T_l^{\mathrm{a}}}{\partial x} - \Omega \left(\frac{\partial T_l^{\mathrm{b}}}{\partial x} - \frac{\partial T_l^{\mathrm{a}}}{\partial x} \right)$$

and

$$\frac{\partial T_l^{\mathrm{c}}}{\partial z} = \frac{\partial T_l^{\mathrm{a}}}{\partial z} - \Omega \left(\frac{\partial T_l^{\mathrm{b}}}{\partial z} - \frac{\partial T_l^{\mathrm{a}}}{\partial z} \right),$$

where Ω represents one of the scaling parameters of the space variables, β_1, β_2 for $z < 0$ and $z > 0$ respectively or ε for $x > 0$. Once the values of the spatial derivatives (4.58) are known at each of the finite difference grid points on the phase change front (see figure 4.5), we parameterise two curves through $(x, \partial T_l/\partial x)$ and $(x, \partial T_l/\partial z)$ respectively, by the arclength formulae

$$s_i^x = s_{i-1}^x + \sqrt{\left(\frac{\partial T_l}{\partial x}^i - \frac{\partial T_l}{\partial x}^{i-1} \right)^2 + (x^i - x^{i-1})^2}\,, \tag{4.59}$$

$$s_i^z = s_{i-1}^z + \sqrt{\left(\frac{\partial T_l}{\partial z}^i - \frac{\partial T_l}{\partial z}^{i-1} \right)^2 + (x^i - x^{i-1})^2}\,, \tag{4.60}$$

for $i = 0, 1, 2, \ldots \overline{n}_f$, with $s_0^x = s_0^z = 0$, where $\overline{n}_f$ is the number of finite difference grid points on the phase change front. Thus for each value of x^i there is a corresponding value of s_i^x and s_i^z; see figure 4.6. Fitting a cubic spline through the points $(s_i^x, \partial T_l^i/\partial x)$ and (s_i^x, x^i) allows us to determine the values of $\partial T_l/\partial x$ at any point on the phase change front. Similarly fitting a cubic spline through $(s_i^z, \partial T_l^i/\partial z)$ and (s_i^z, x^i) will produce a value for $\partial T_l/\partial z$ at any point on the phase change front. Thus by expressing the position of the boundary integral mesh points on the phase change front in terms of the respective arclengths (4.59) and (4.60), the required spatial derivatives (4.58) can be evaluated from the cubic spline approximations. Thus the elements of the $\nabla' T_l$ term appearing in equation (4.56) can now be calculated.

In this formulation, a given value of x, $x^* = x(s^*)$ say, has a one-to-one correspondence with a particular z^* value, for $z^* > 0$ and $z^* < 0$. If this is not the

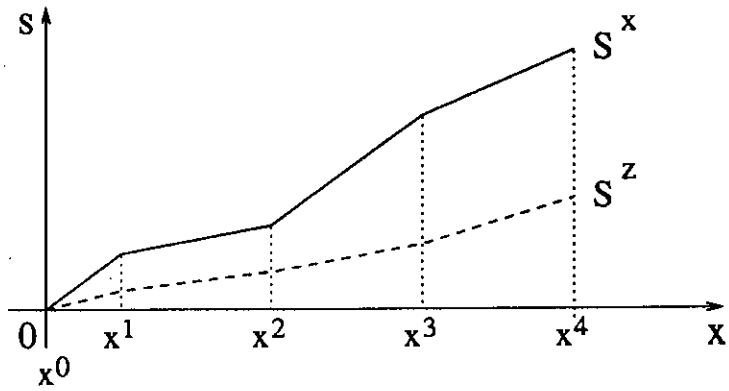

Figure 4.6: Plot of the arclengths s_i^x and s_i^z against x^i

case and we obtain multiple values of z for a given x^*, greater care is required in determining the correct arclength s^*. This may be achieved, for example, by parameterising the curves $(z, \partial T_l/\partial x)$ and $(z, \partial T_l/\partial z)$ by their respective arclengths and ensuring that correct values of $z^*, \partial T_l/\partial x$ and $\partial T_l/\partial z$ are selected.

The outward unit normal $\underline{n}$ is also required at each boundary integral grid point on the phase change front. The procedure employed here to evaluate the normals is discussed in the paper by Henshaw *et al* [29]. Firstly the boundary integral grid points on the phase change front are parameterised by

$$s_i = \begin{cases} 0 & \text{if } i = 0 \\ s_{i-1} + |\underline{x}_i - \underline{x}_{i-1}| & \text{if } i = 1, 2, \ldots, \overline{n}_b. \end{cases} \tag{4.61}$$

Here s_i is the arclength on the front and $\underline{x}_i = (x_i, z_i)$ is the ith boundary integral grid point on the phase change front, $i = 0, 1, 2, \ldots, \overline{n}_b$. The normal $\underline{n}$ to the phase change front is determined by differentiating two cubic splines fitted through the data (s_i, x_i) and (s_i, z_i), $i = 0, 1, 2, \ldots, \overline{n}_b$. Let these two cubic splines be denoted by $\overline{x}(s)$ and $\overline{z}(s)$ respectively. The smooth curve $(\overline{x}(s), \overline{z}(s))$ is then an approximation to the phase change front and therefore the normal $\underline{n}_i$, at the ith point, is given by

$$\underline{n}_i = \frac{(\overline{z}'(s_i), -\overline{x}'(s_i))}{\left[(\overline{x}'(s_i))^2 + (\overline{z}'(s_i))^2\right]^{\frac{1}{2}}}, \tag{4.62}$$

where the primes denote differentiation with respect to s. The normal velocity of the phase change front is then evaluated at these same points as

$$\underline{n}_i \cdot \underline{V}_i \approx \frac{n_{ix}\,\varepsilon\,\Delta x + n_{iz}\,\beta\,\Delta z}{\Delta t}. \tag{4.63}$$

Once these normal velocities have been calculated, equation (4.57) can be used to obtain $|\nabla' f|$. Thus using the numerical approximations obtained by extrapolation to the spatial derivatives (4.58) on the phase change front, we can obtain

numerical estimates of the gradients (4.56) to be used in the Stefan condition (4.54) that links the two regions of different phase. This process is repeated each time a new front position is calculated.

In general, for stability the time step used in the numerical approximation of the fluid flow equations is smaller than that used in the integral equation (4.53) for the solid phase. To make the two time steps compatible, a step for the solid phase Δt_s and a suitable time step Δt_l for the liquid phase are chosen such that $\Delta t_s = C\,\Delta t_l$, where the constant $C \in \mathbb{N}$. If the same time steps were used in the boundary integral and fluid flow numerical schemes so that $\Delta t_s = \Delta t_l$, then the areas of the quadrilaterals used in the boundary integral method would become so small that they would become of the same order as the rounding error. A detailed discussion of the stability of the convective difference scheme used here can be found in Roberts and Weiss [47]. The stability of the numerical approximations of the fluid flow equations is discussed by Moore, Peckover and Weiss [38]. It was shown by those authors that the numerical scheme for the fluid flow equations is stable for

$$\frac{\nu_l\,\Delta t}{\Delta s^2} \leq \frac{1}{2} \quad \text{and} \quad \frac{D_l\,\Delta t}{\Delta s^2} \leq \frac{1}{2} \tag{4.64}$$

where Δs is the minimum of $(\Delta x, \Delta z)$.

4.2.3 Numerical Implementation

The numerical procedure to solve the integral equation (4.53) in the solid phase together with the convection-diffusion equation (4.47), vorticity equation (4.48) and the streamfunction equation (4.49) in the liquid phase is now discussed. In addition the numerical procedure to be discussed here also applies to the equations of fluid motion with a quadratic equation of state.

The boundary conditions are taken to be those given in sub-section 4.1.2. It is assumed that the temperature gradients $\nabla' T_l' \cdot \nabla' f$ are known on the moving phase change front B_p for times 0 up to $(k-1)\Delta t_s$. The position of the phase change front at time $k\Delta t_s$ is then approximated by extrapolating from its previous positions. The mesh for the fluid flow equations is then reduced to active and inactive grid points. On the active grid points the finite difference approximations of the governing equations of fluid flow are applied. The difference in magnitude of the fluid flow time step and boundary integral time step, $\Delta t_s = C\,\Delta t_l$, necessitates that for each boundary integral time step we have to perform C fluid flow time steps for the total time to concur. The unknown gradients $\nabla' T_l' \cdot \nabla' f$ on the phase change front at time $k\Delta t_s$ can now be found using the cubic splines approximation, as outlined in sub-section 4.2.2. From these gradients and the Stefan

condition (4.20), the gradients behind the phase change front $\nabla' T_s' \cdot \nabla' f$ can then be determined. Substituting these gradients into the linear system that results from the integral equation (4.53), the unknown boundary data, in this case the normal temperature gradients $\partial T_s / \partial n$, on the boundary B_f can be found. Once the unknown boundary data is found, Newton's method is employed, with the temperature T_s given by the discretised form of (4.53), to locate where the temperature T_s is zero. This provides a revised position of the phase change front at time $k\Delta t_s$. The whole process is repeated until successive estimates of the front positions lie within a prescribed tolerance. As in section 3.3, the first front position and gradients $\nabla' T_l' \cdot \nabla' f$ at time $t = \Delta t_s$ are obtained from the one-dimensional solution, equations (2.9) and (2.10). To keep the phase change front smooth, when the iterations have converged the points on the phase change front are passed through a three point smoothing scheme. As in section 3.3, Newton's method is employed in the location of where the temperature $T_s = 0$, unless D_s is large, in which case Newton's method converges slowly. For D_s large a bisection method is then used to determine the position of the phase change front. Thus if Newton's method has not converged within a specified number of iterations, the front finding method is switched to the bisection method.

4.3 Results

The numerical method presented in sections 4.2 to 4.2.3 was applied to a number of examples of the freezing of a region which includes fluid motion in the liquid phase. For simplicity and comparison with the previous examples of Chapter 3 the constant boundary condition $T_{sb} < 0$ on the fixed boundary B_f and the constant initial condition $T_{l0} > 0$ are used. Furthermore, in order to induce the instability in the rest state of the fluid, the vorticity ω was given a small initial value ω_0 with $|\omega_0| \ll 1$. A more detailed discussion of the formulation of the problems presented in this section is given in sub-section 4.1.2.

In the following examples the contour plots were drawn using N.C.A.R. graphics version 2.0 [11]. The surface and the (x, y) type two dimensional plots where drawn using GNUplot version 3.5.

As a means of validating the finite difference scheme for solving the fluid motion equations we compare the results of the present scheme with the solution of the classical Bénard convection problem presented by Moore *et al.* [38]. In this context, the fluid equations are solved on a square of side length 1.0 with the origin located at lower left hand corner. The lower boundary along $z = 0$ is maintained at a temperature of $T_l(x, 0, t) = 1.0$ whilst on the upper boundary

along $z = 1$ the temperature is $T_l(x, 1, t) = 0.0$. On the sides of the square along $x = 0$ and $x = 1$ the zero-flux (insulated) boundary condition is imposed. The region was discretised with a spatial step of $\Delta s (= \Delta x = \Delta z) = 1/90$ and a time step of $\Delta t = 7.5 \times 10^{-3}$. The initial conditions for temperature and vorticity are taken to be $T_{l0} = 0.25$ and $\omega_0 = 7.5 \times 10^{-3}$ respectively. A Rayleigh number $Ra = 657.5 \times 10^3$ and Prandtl number $Pr = 1.0$ were chosen. In this case the Rayleigh number is $1000 \times Ra_c$, where Ra_c is the critical Rayleigh number for instability. Using a value of the Rayleigh number which is greater than the critical value Ra_c induced convective motion in the fluid due to instability. The fluid equations (4.47) to (4.49) were solved using these parameters until steady convection was reached and this steady flow was found to compare favourably with the results of Moore *et al.* [38].

Figure 4.7 shows contour and surface plots of the vorticity at steady state with a single steady vortex formed. The lozenge shaped distribution of vorticity is in good agreement with that obtained by Moore *et al.* [38]. Figure 4.8 shows surface and contour plots for the temperature distribution, also at steady state. In this case two vortices are shown to distinguish more clearly the transport of heat from the top to the bottom of the region. It should be noted that the orientation of the surface plot is different to that of the contour plot to highlight the features of this plot more clearly. In this case the temperature remains roughly constant in the centre of each vortex with two horizontal boundary layers formed at $z = 0$ and $z = 1$. The rise of hot fluid from the boundary layer at $z = 0$ and the fall of colder fluid from the boundary layer at $z = 1$ is clearly visible in both of these plots. This exchange of hot and cold fluid results in the convective motion which characterises Bénard convection problems. Finally figure 4.9 shows surface and contour plots for the streamfunction at steady state with a single steady vortex formed.

The full numerical scheme for two-phase Stefan problems that includes fluid motion, presented in the previous sections, was applied to the freezing of water which is contained in a square region of non-dimensional side length 2.0. In particular three different non-dimensional initial conditions were investigated $T_{l0} = 0.40$ $(4\,^{\circ}C)$, $T_{l0} = 0.75$ $(7.5\,^{\circ}C)$ and $T_{l0} = 1.50$ $(15\,^{\circ}C)$. As far as possible the other parameters were kept the same for each of the three initial conditions for the purpose of comparison. It was, however, found necessary to change the time steps in each of the three simulations as this proved the best way in which to capture the dynamics of the fluid motion in each case. The computational region is reduced by symmetry from solving on a square of side 2.0 to solving on a rectangle with width in the x direction of 1.0 and height in the z direction of

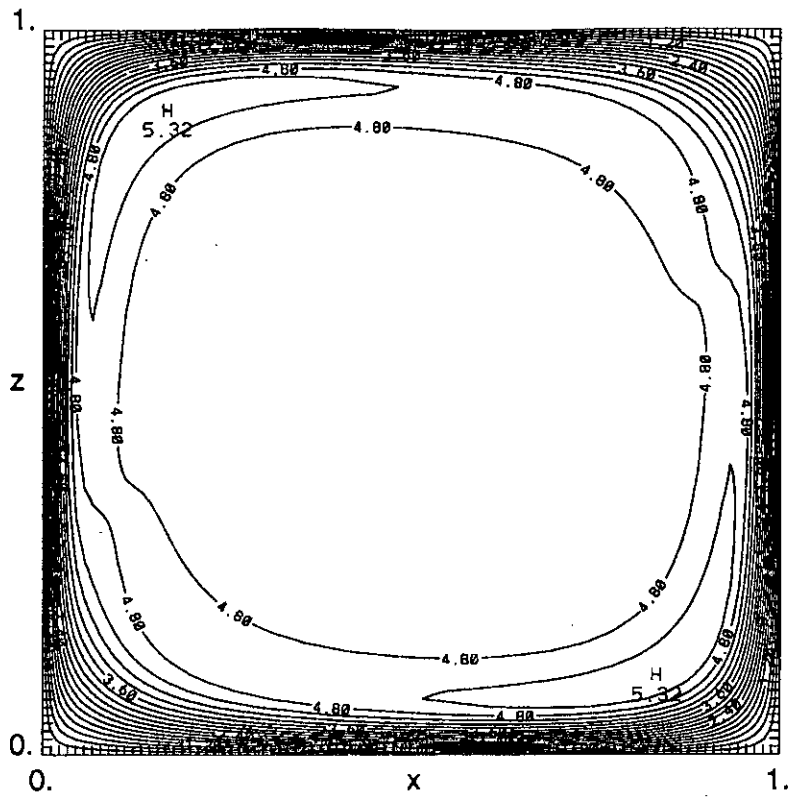

(a) Contours of the vorticity ω from 0.0 to 0.480 at intervals of 0.03

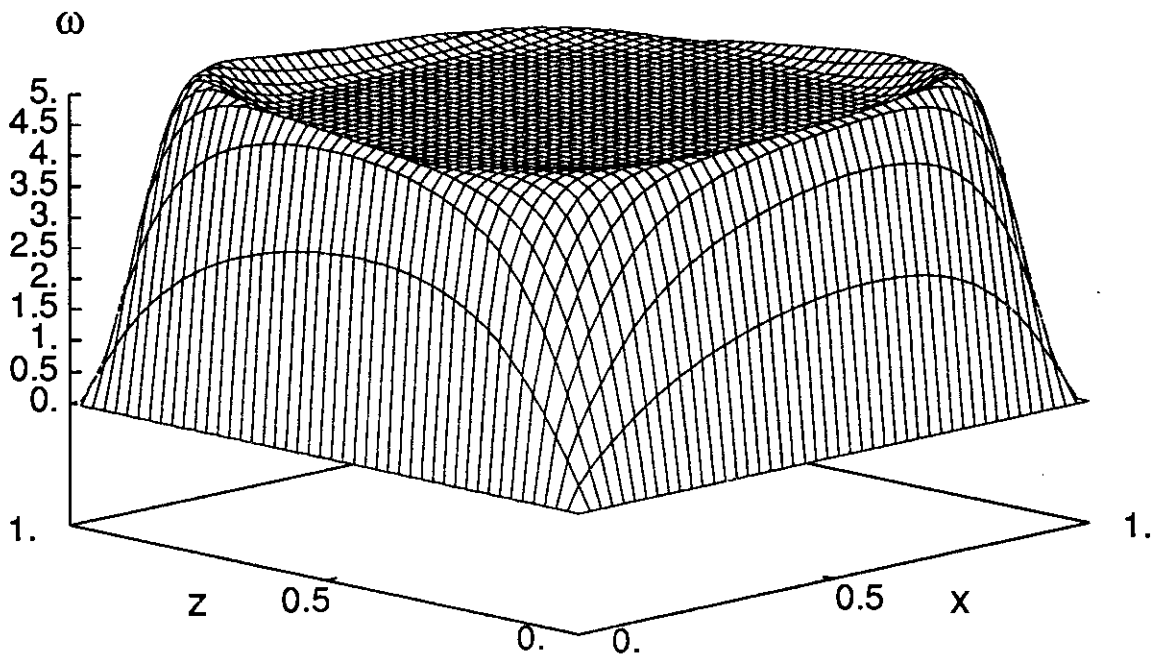

(b) Surface plot of vorticity ω at alternate (x, z) grid points for a single vortex

Figure 4.7: Vorticity distribution at steady state with initial conditions $T_{l0} = 0.25$ and $\omega_0 = 7.5 \times 10^{-3}$. The spatial step is $\Delta s = 1/90$ and the time step is $\Delta t = 7.5 \times 10^{-3}$. The dimensionless constants are $Ra = 657.5 \times 10^3$ and $Pr = 1.0$

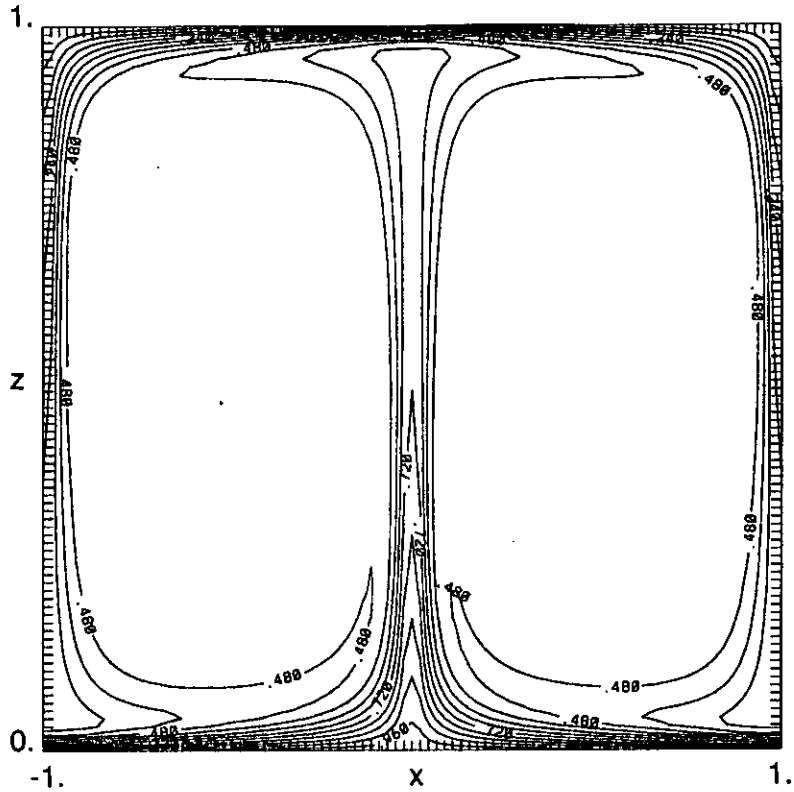

(a) Isotherms from 0.0 to 1.0 at intervals of 0.06

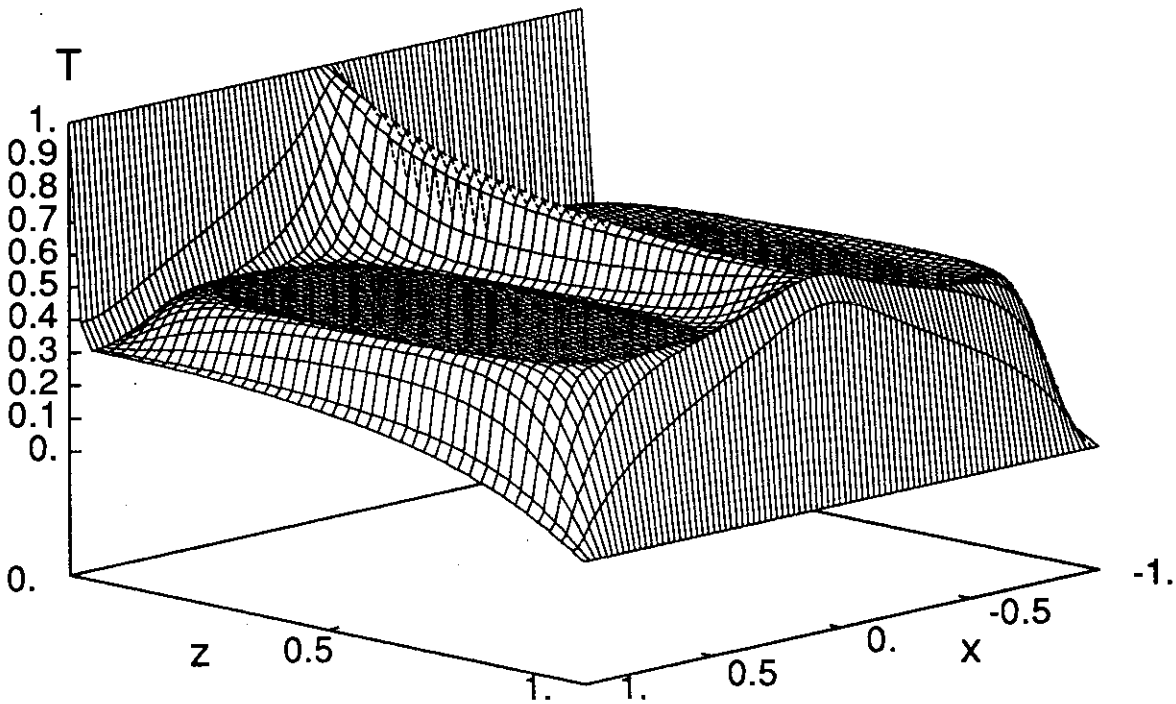

(b) Surface plot of temperature distribution over two vortices at alternate (x, z) grid points

Figure 4.8: Temperature distribution at steady state with initial conditions $T_{l0} = 0.25$ and $\omega_0 = 7.5 \times 10^{-3}$. The spatial step is $\Delta s = 1/90$ and the time step is $\Delta t = 7.5 \times 10^{-3}$. The dimensionless constants are $Ra = 657.5 \times 10^3$ and $Pr = 1.0$

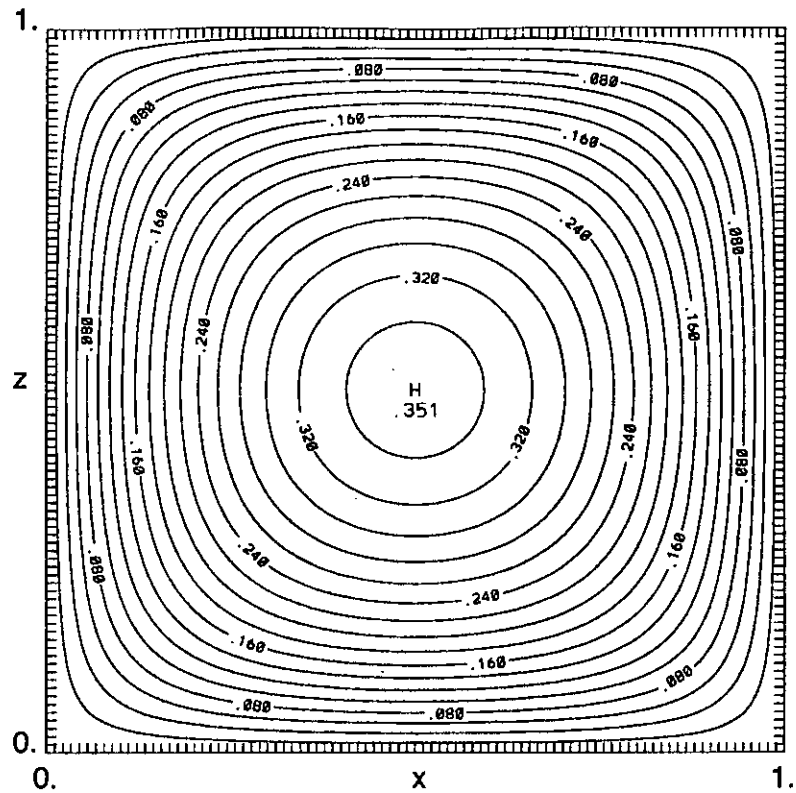

(a) Streamlines: contours of the streamfunction ψ from 0.0 to 0.340 at intervals of 0.02

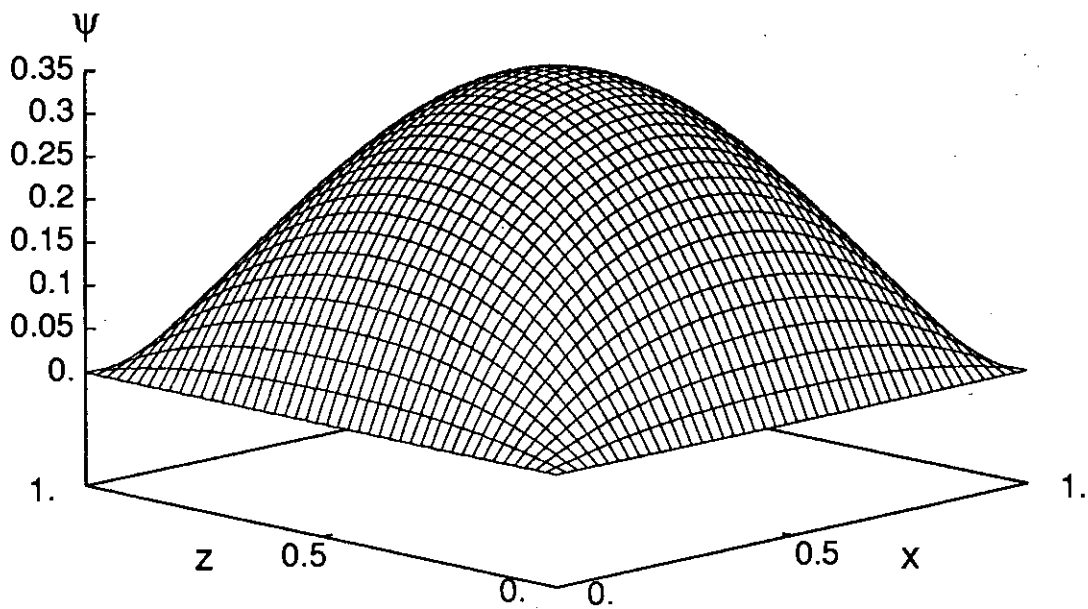

(b) Surface plot of the streamfunction ψ at alternate (x, z) grid points for a single vortex

Figure 4.9: Streamfunction distribution at steady state with initial conditions $T_{l0} = 0.25$ and $\omega_0 = 7.5 \times 10^{-3}$. The spatial step is $\Delta s = 1/90$ and the time step is $\Delta t = 7.5 \times 10^{-3}$. The dimensionless constants are $Ra = 657.5 \times 10^3$ and $Pr = 1.0$

Quantity	Symbol	Value
Thermal diffusivity (liquid)	D_l	4.280784×10^{-4}
Thermal diffusivity (solid)	D_s	3.837696×10^{-3}
Thermal conductivity	K	4.151624
Prandtl number	Pr	7.519227
Rayleigh number	Ra	7.257384×10^{5}
Stefan number	S_t	1.669446×10^{4}
Kinematic viscosity	v_l	3.218819×10^{-3}

Table 4.1: Values of non-dimensional parameters for water generated with length scale $\tilde{d}_b$; see Appendix A : table A.1

2.0. A schematic representation of the computational region is shown in figure 4.2 in sub-section 4.1.2. One should note that for this type of problem there may be symmetry breaking solutions due to the inherent nonlinearity of the problem. However for the problems considered in this section this was not found to be the case.

Figures 4.10 to 4.15 show contour and surface plots of vorticity, temperature and streamfunction at non-dimensional times $t = 20.0$ (40.23 secs) and $t = 40.0$ (80.47 secs) for an initial condition of $T_{l0} = 0.40$ ($4\,^{\circ}C$). The boundary condition was taken to be $T_{sb} = -2.0$ ($-20\,^{\circ}C$) and the initial vorticity was $\omega_0 = 5.0 \times 10^{-3}$. The region was discretised with spatial steps for the solid and liquid regions of $\Delta s_s = 5.0 \times 10^{-2}$ and $\Delta s_l = 1.25 \times 10^{-2}$ respectively. The solid and liquid time steps were $\Delta t_s = 10.0$ and $\Delta t_l = 5.0 \times 10^{-3}$ respectively. The dimensional parameters for water are shown in Appendix A, table A.1 and the non-dimensional parameters are given table 4.1.

Figures 4.10 and 4.13 show the vorticity profiles at times $t = 20.0$ (40.23 secs) and $t = 40.0$ (80.47 secs) respectively. It should be noted that the orientation of the surface plot in both cases is different to that of the contour plot to highlight the features more clearly. Furthermore the ragged edge that is found at the zero contour is a consequence of the fact that we are trying to describe a curve with a square mesh. All grid points that occur behind the phase change front as part of the inactive grid have been assigned the value zero. This is found necessary since a regular mesh is required by both the contour and surface plot packages. In each of these plots two dominant vortices, one positive and one negative, can clearly be seen. They are formed by some fluid being above and some below the temperature at which water attains its maximum density; $3.98\,^{\circ}C$ experimentally and $3.55\,^{\circ}C$ for our model (see sub-section 4.1.1). For water with temperature above $3.55\,^{\circ}C$ located at the left of the region $0 \leq x \leq 1$, the hot fluid in the middle of the liquid

region rises and the cold water near the phase change front descends carrying a clockwise rotating vortex. Conversely for water with temperature below $3.55\,^{\circ}C$, this water being located at the right hand side of the liquid region, the hot fluid in the middle of the region descends and the cold fluid near the phase change front rises carrying an anticlockwise rotating vortex. Once the temperature ahead of the phase change front falls below $3.55\,^{\circ}C$ everywhere in the liquid region there are no longer any counter rotating vortices within the fluid. A single anticlockwise rotating vortex will dominate the fluid motion until the fluid is completely frozen. Furthermore along the upper and lower sides of the liquid region in both figures 4.10 and 4.13 the boundary layers occurring there can be clearly seen.

Multiple vortices would not occur for this problem if the density of water was modelled using a linear equation of state i.e. as a linear function of temperature. This is because there no longer exists a value of temperature $\tilde{T}_{lc}$ ($= 3.55\,^{\circ}C$ in this case) that produces an anticlockwise rotating vortex when $\tilde{T}_l < \tilde{T}_{lc}$ and a clockwise rotating vortex for $\tilde{T}_{lc} < \tilde{T}_l$. For a linear equation of state a small anticlockwise vortex is formed and remains for the duration of the freezing.

Figures 4.11 and 4.14 show the temperature profiles both ahead of and behind the phase change front at times $t = 20.0$ (40.23 secs) and $t = 40.0$ (80.47 secs) respectively. A three point smoothing routine has been applied at the interface of the solid and liquid regions to eliminate the ragged mesh points there. The initial condition for temperature in the case, $T_{l0} = 0.40$ ($4\,^{\circ}C$), was taken as an example close to the density maximum of water. Below this temperature density is as an increasing function of temperature (see sub-section 4.1.1). We thus expect the hot fluid to sink towards the bottom of the liquid region and the colder fluid to rise, which is apparent in figures 4.11 and 4.14. The colder fluid on the right hand side of the liquid region is rising towards the top with the hot fluid at the top of the liquid region being cooled by the rising fluid and by the phase change front. This hot fluid then descends to the left of the liquid region since the cold fluid is rising from the right. This continuing exchange of hot and cold fluid forces the circulation in an anticlockwise direction. The increasing penetration of colder fluid on the left hand side of the liquid region caused by this circulation can be seen quite clearly at $\tilde{t} = 40.23$ secs in figure 4.11 and to a greater extent at $\tilde{t} = 80.47$ secs in figure 4.14.

Figures 4.12 and 4.15 show the streamfunction profiles at times $t = 20.0$ (40.23 secs) and $t = 40.0$ (80.47 secs) respectively. The orientation of the surface plots is again different to the contour plots to highlight the features of these plots more clearly. A single vortex is formed in the corner of the liquid region in figure 4.12 and it moves to a more central position in figure 4.15. At subsequent time steps

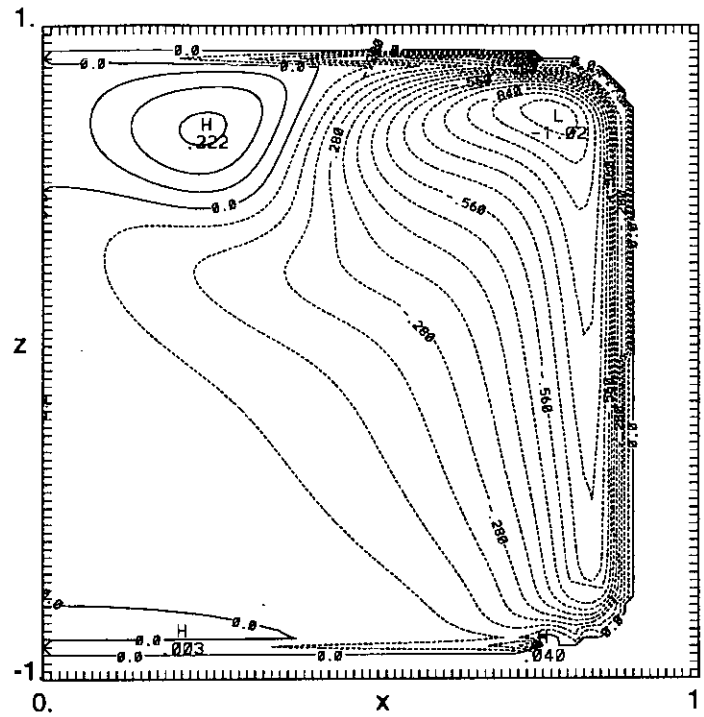

(a) Contours of the vorticity ω from -0.98 to 0.21 at intervals 0.07

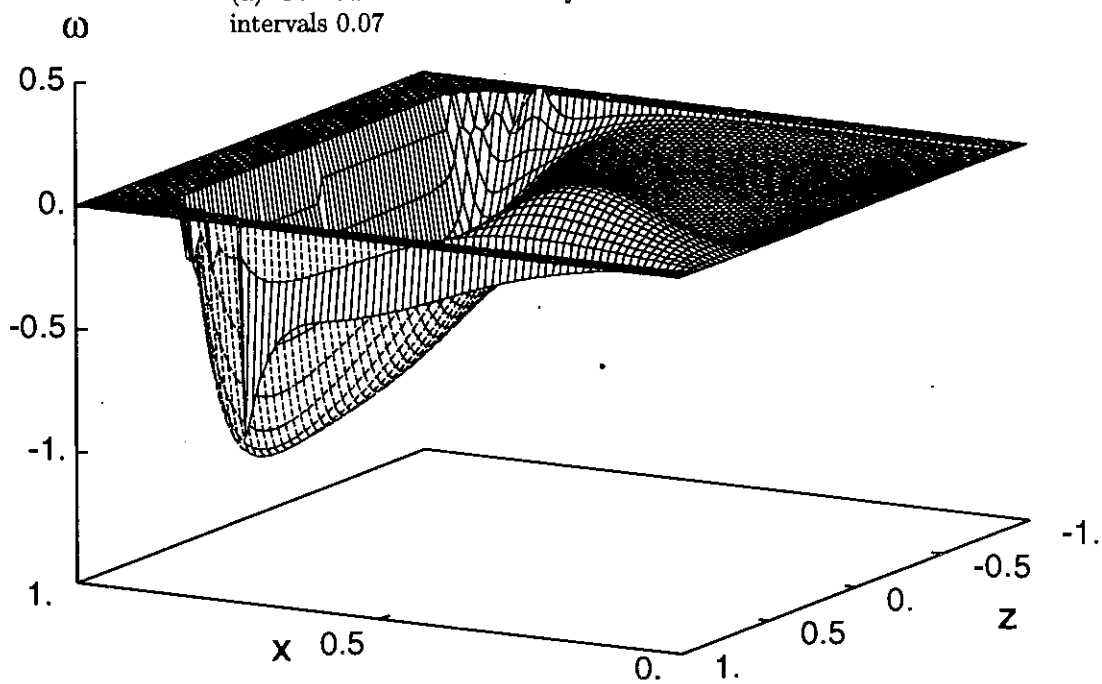

(b) Surface plot of vorticity ω at alternate each alternate row of mesh

Figure 4.10: Vorticity distribution at time $t = 20.0$ with initial conditions $T_{l0} = 0.40$ and $\omega_0 = 5.0 \times 10^{-3}$. The spatial and time steps for the solid and liquid regions are $\Delta s_s = 5.0 \times 10^{-2}$, $\Delta s_l = 1.25 \times 10^{-2}$, $\Delta t_s = 10.0$ and $\Delta t_l = 5.0 \times 10^{-3}$ respectively. The dimensionless constants for water are given in table 4.1

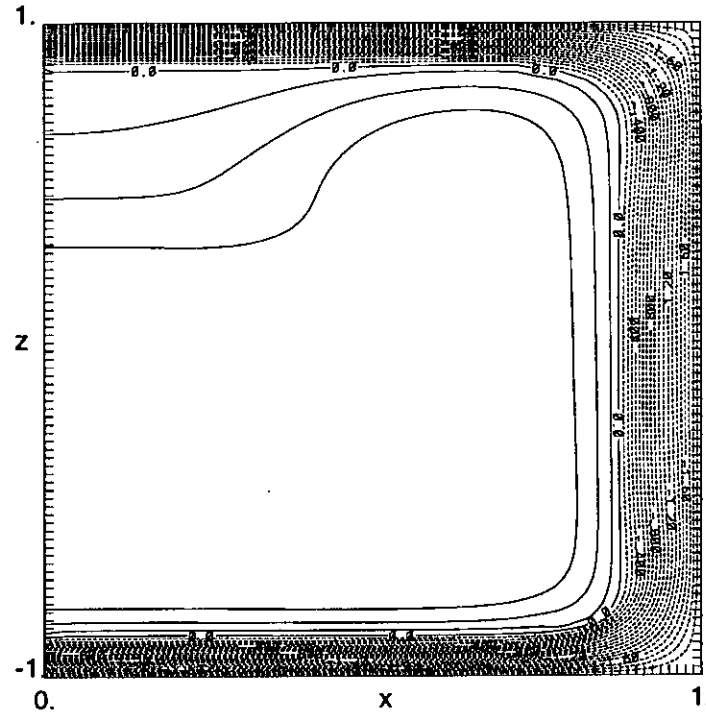

(a) Isotherms from -2.0 to 0.30 at intervals of 0.10

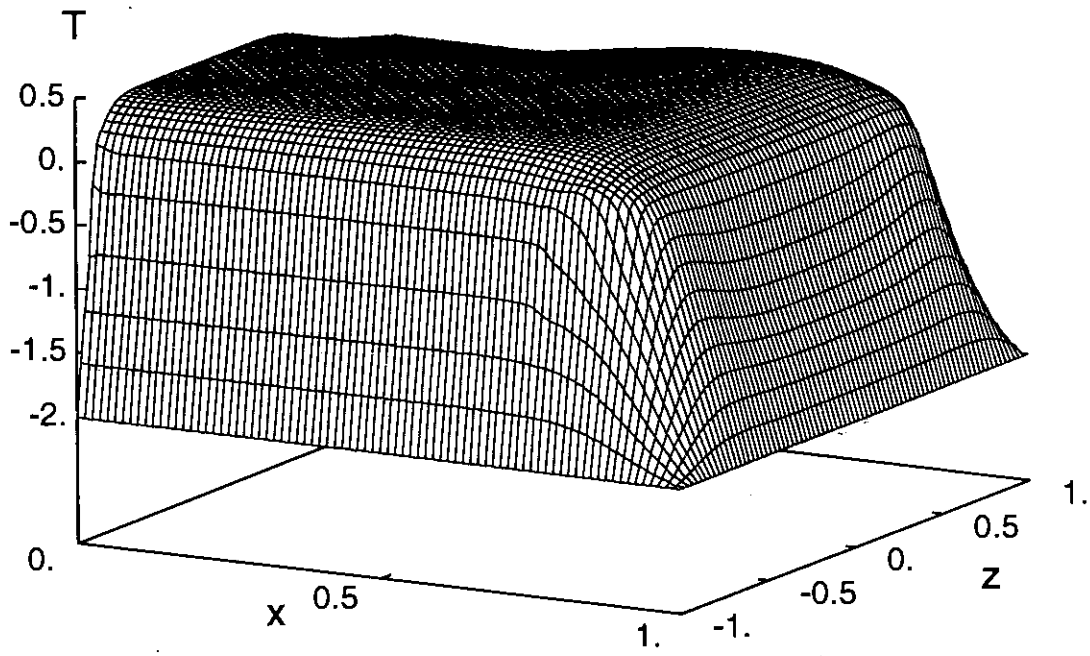

(b) Surface plot of temperature T at alternate each alternate row of mesh

Figure 4.11: Temperature distribution at time $t = 20.0$ with initial conditions $T_{l0} = 0.40$ and $\omega_0 = 5.0 \times 10^{-3}$. The spatial and time steps for the solid and liquid regions are $\Delta s_s = 5.0 \times 10^{-2}$, $\Delta s_l = 1.25 \times 10^{-2}$, $\Delta t_s = 10.0$ and $\Delta t_l = 5.0 \times 10^{-3}$ respectively. The dimensionless constants for water are given in table 4.1

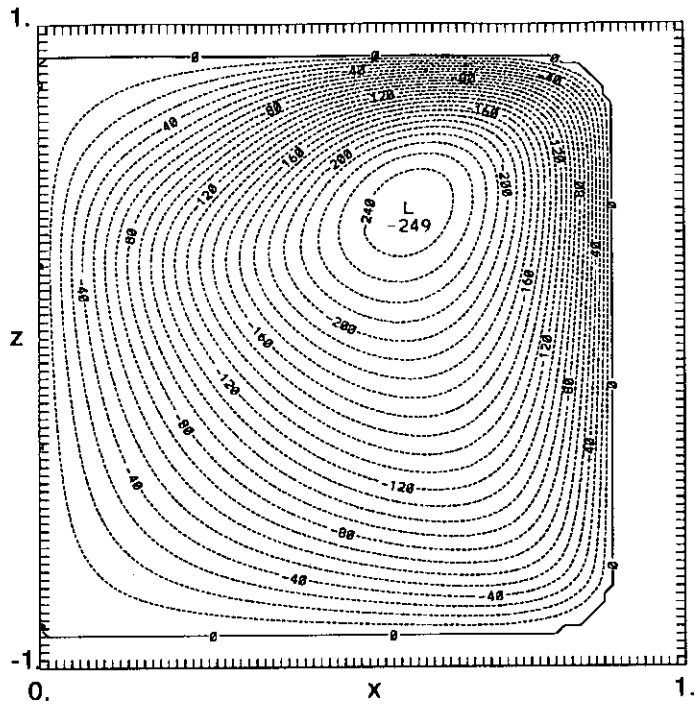

(a) Streamlines: contours of the streamfunction ψ from -2.4×10^{-2} to 0.0 at intervals of 1.0×10^{-3}. (Scaled by 10^4)

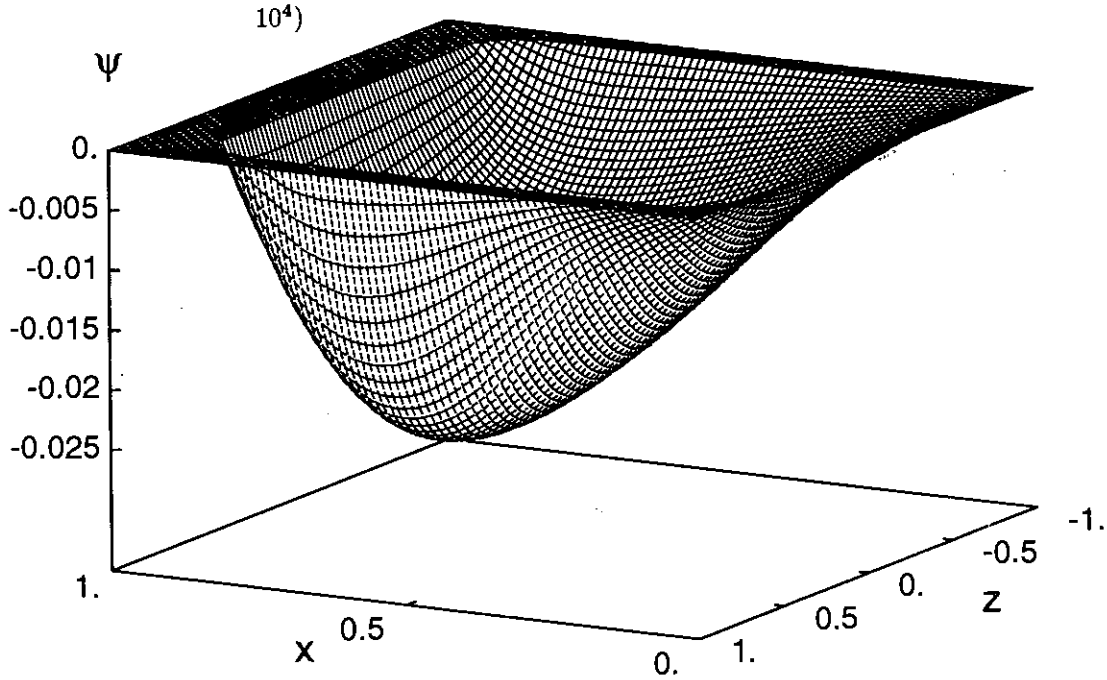

(b) Surface plot of streamfunction ψ at alternate each alternate row of mesh

Figure 4.12: Streamfunction distribution at time $t = 20.0$ with initial conditions $T_{l0} = 0.40$ and $\omega_0 = 5.0 \times 10^{-3}$. The spatial and time steps for the solid and liquid regions are $\Delta s_s = 5.0 \times 10^{-2}$, $\Delta s_l = 1.25 \times 10^{-2}$, $\Delta t_s = 10.0$ and $\Delta t_l = 5.0 \times 10^{-3}$ respectively. The dimensionless constants for water are given in table 4.1

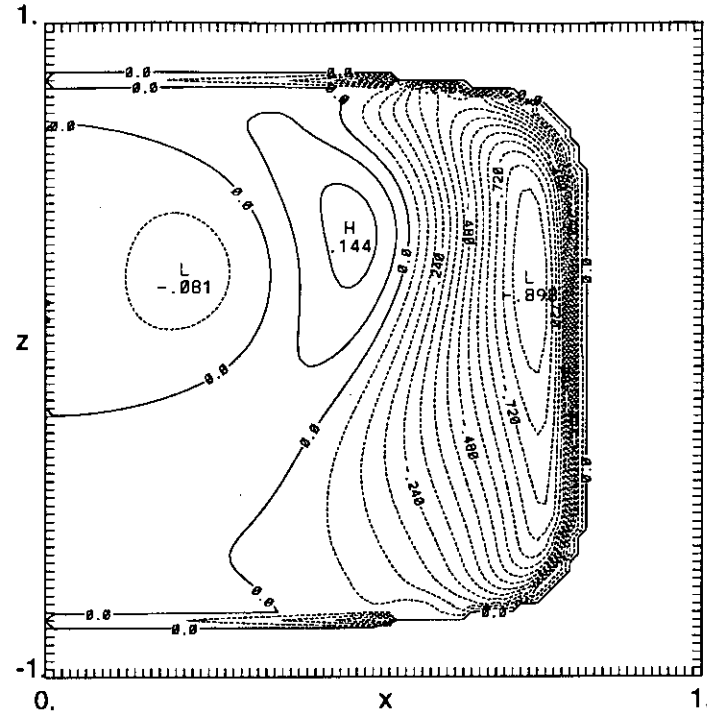

(a) Contours of the vorticity ω from -0.84 to 0.12 at intervals 0.06.

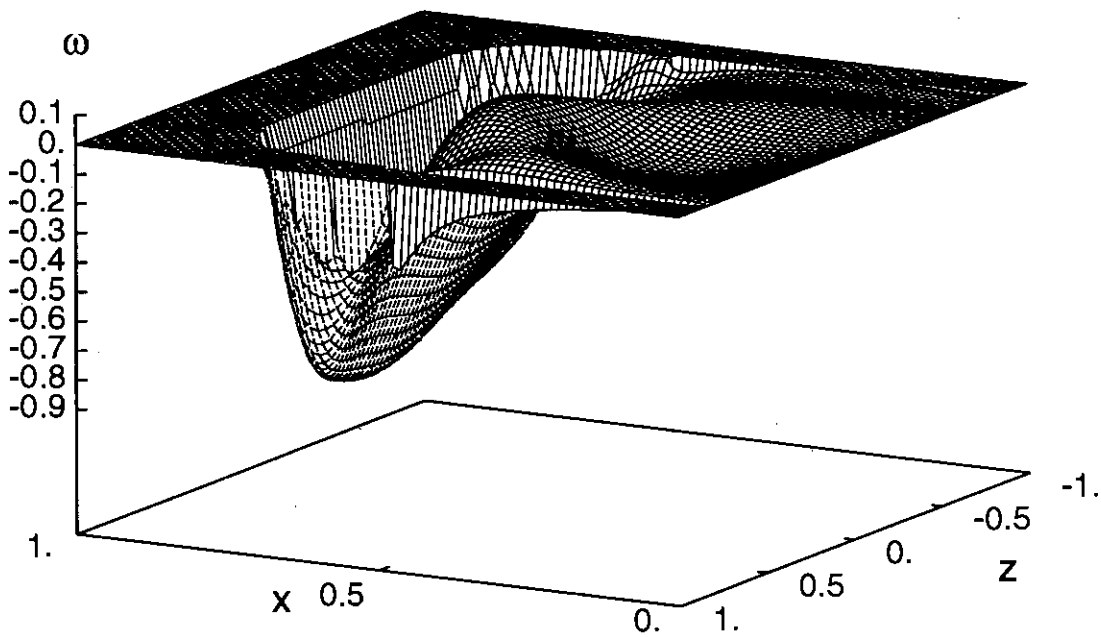

(b) Surface plot of vorticity ω at alternate each alternate row of mesh

Figure 4.13: Vorticity distribution at time $t = 40.0$ with initial conditions $T_{l0} = 0.40$ and $\omega_0 = 5.0 \times 10^{-3}$. The spatial and time steps for the solid and liquid regions are $\Delta s_s = 5.0 \times 10^{-2}$, $\Delta s_l = 1.25 \times 10^{-2}$, $\Delta t_s = 10.0$ and $\Delta t_l = 5.0 \times 10^{-3}$ respectively. The dimensionless constants for water are given in table 4.1

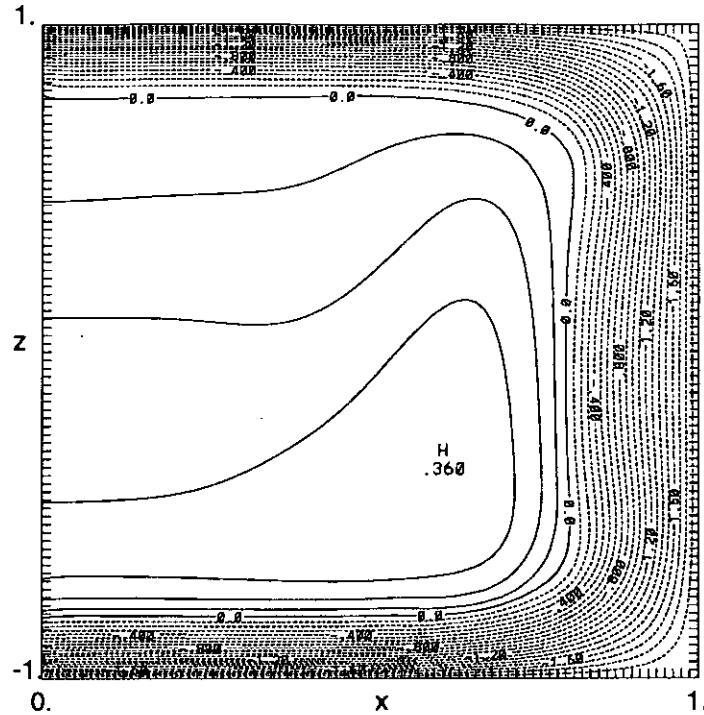

(a) Isotherms from -2.0 to 0.30 at intervals of 0.10

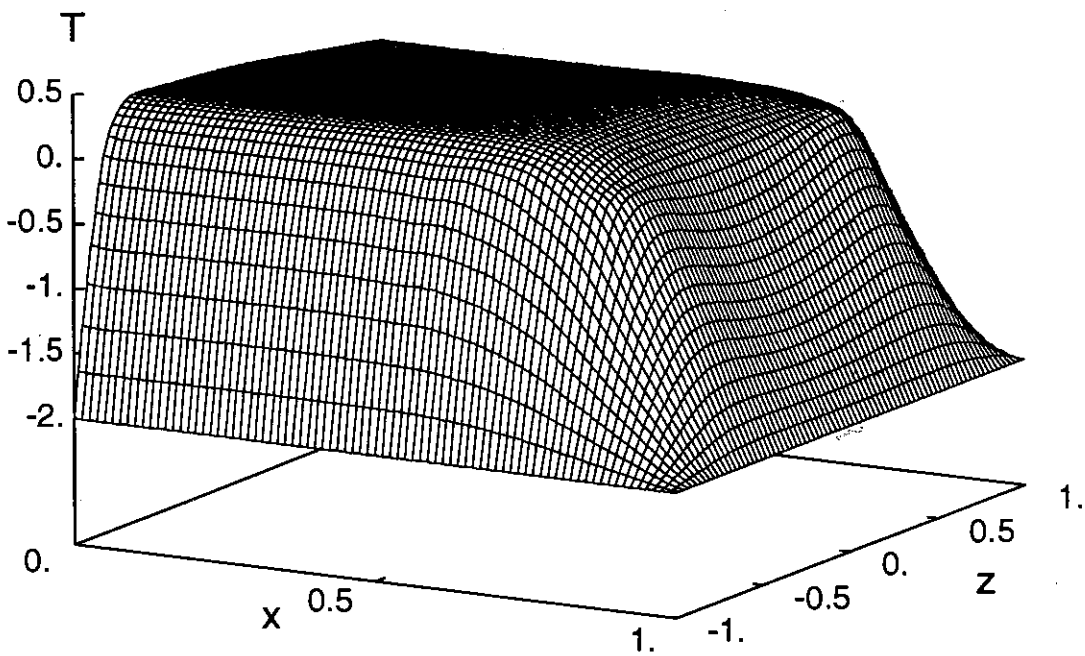

(b) Surface plot of temperature T at alternate each alternate row of mesh

Figure 4.14: Temperature distribution at time $t = 40.0$ with initial conditions $T_{l0} = 0.40$ and $\omega_0 = 5.0 \times 10^{-3}$. The spatial and time steps for the solid and liquid regions are $\Delta s_s = 5.0 \times 10^{-2}$, $\Delta s_l = 1.25 \times 10^{-2}$, $\Delta t_s = 10.0$ and $\Delta t_l = 5.0 \times 10^{-3}$ respectively. The dimensionless constants for water are given in table 4.1

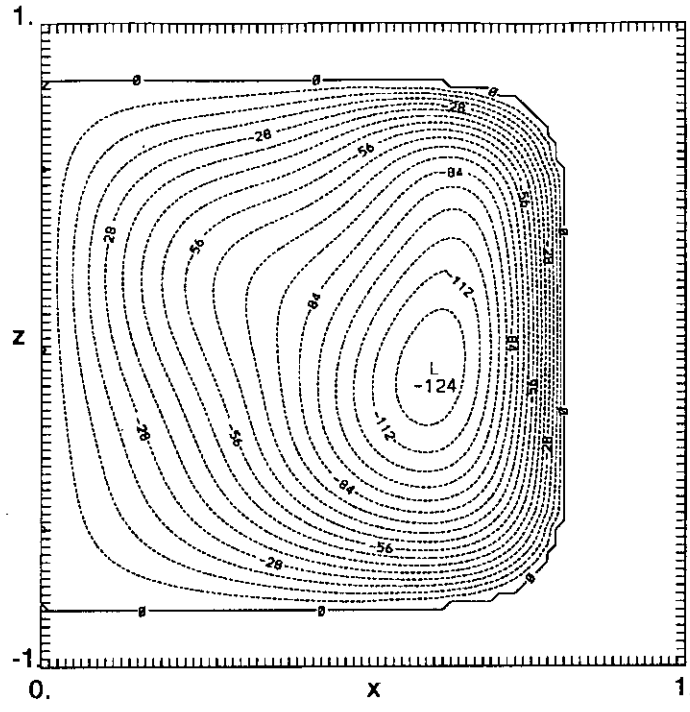

(a) Streamlines: contours of the streamfunction ψ from -1.19×10^{-2} to 0.0 at intervals of 7.0×10^{-4}. (Scaled by 10^4)

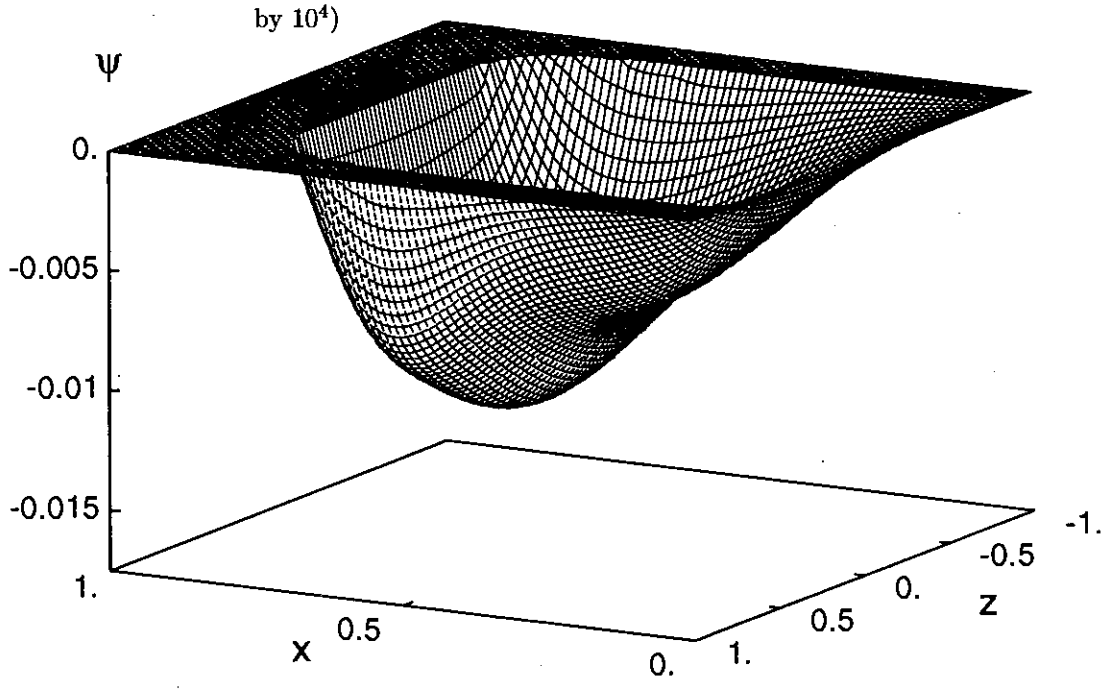

(b) Surface plot of streamfunction ψ at alternate each alternate row of mesh

Figure 4.15: Streamfunction distribution at time $t = 40.0$ with initial conditions $T_{l0} = 0.40$ and $\omega_0 = 5.0 \times 10^{-3}$. The spatial and time steps for the solid and liquid regions are $\Delta s_s = 5.0 \times 10^{-2}$, $\Delta s_l = 1.25 \times 10^{-2}$, $\Delta t_s = 10.0$ and $\Delta t_l = 5.0 \times 10^{-3}$ respectively. The dimensionless constants for water are given in table 4.1

the single anticlockwise rotating vortex remains roughly in this central position.

The previous simulation was repeated with an initial temperature condition of $T_{l0} = 0.75$ $(7.5\,^{\circ}C)$. In this case the time steps for the solid and liquid phases were taken as $\Delta t_s = 15.0$ and $\Delta t_l = 6.0 \times 10^{-3}$ respectively. Figures 4.16 to 4.21 show contour and surface plots of the vorticity, temperature and streamfunction at times $t = 30.0$ (60.35 secs) and $t = 60.0$ (120.70 secs) for this initial condition.

The vorticity profiles at times $t = 30.0$ (60.35 secs) and $t = 60.0$ (120.70 secs) are shown in figures 4.16 and 4.19 respectively. The surface plots have again been orientated differently to the contour plots to enable the details of these plots to be seen more clearly. In figure 4.16 four separate vortices can be seen; two positive and two negative. For the positive vortex in the top right hand corner of the computational region ahead of the phase change front the temperature is greater than $\tilde{T}_{lc}$ $(= 3.55\,^{\circ}C)$. Therefore hot fluid is rising and cold fluid is falling, resulting in clockwise rotation. The other positive vortex also has a clockwise rotation. However the temperature in this vortex is less than $\tilde{T}_{lc}$ and so cold fluid is rising from the lower boundary and hot fluid is falling. In the bottom right hand corner of the liquid region the negative vortex is occurring in an area where the temperature of the fluid is below $\tilde{T}_{lc}$ as the temperature is less than that for the maximum water density colder fluid rises and hotter fluid falls, resulting in an anticlockwise rotation of fluid. The remaining negative vortex, which has an anticlockwise rotation, occurs roughly in the centre of the region and is being pulled down by the effects of temperature and the two clockwise rotating vortices. In contrast the fluid flow at the later time in figure 4.19 is dominated by three vortices, two positive and one negative. On the right hand side of $0 \leq x \leq 1$ the fluid is being cooled by the phase change boundary of the liquid region. Consequently the temperature of the fluid there has cooled quite rapidly, forcing it below $\tilde{T}_{lc}$. This results in circulation with cold fluid rising and hot fluid falling resulting in an anticlockwise rotating vortex. The second dominant vortex ahead of the phase change frout occurs at the bottom left hand corner of the liquid. Here the temperature is below $\tilde{T}_{lc}$ and the cool fluid is rising from the lower boundary and the hot descending, resulting in a clockwise rotating vortex. Finally the the remaining positive vortex is formed in quite a central location where the temperature of the fluid is close to or below $\tilde{T}_{lc}$. As the fluid cools in this part of the liquid region it begins to rise towards th upper boundary resulting in a clockwise rotating vortex. In both figures 4.16 and 4.19 the boundary layers occurring at the top and bottom of the liquid region can be clearly seen.

The long term behaviour of the vortices in this case is the same as in the

previous example, for which $T_{l0} = 0.4$ ($4\,^{\circ}C$). That is, once the fluid ahead of the phase change front is cooled below the critical temperature $\tilde{T}_{lc}$ everywhere, a single clockwise rotating vortex is formed and this vortex will dominate until freezing is complete. This is achieved much more rapidly when the initial temperature T_{l0} is close to the critical temperature $\tilde{T}_{lc}$ since less heat needs to be removed from the liquid phase before the single vortex is formed.

The temperature profiles both ahead of and behind the phase change front are shown at times $t = 30.0$ (60.35 secs) and $t = 60.0$ (120.70 secs) in figures 4.17 and 4.20 respectively. Again a three point smoothing routine has been applied at the interface of the solid and liquid phases to eliminate the ragged mesh points there. The initial condition in this case is larger that the critical temperature $\tilde{T}_{lc}$ and therefore we expect that for most of liquid region (i.e. except near the phase change front) the hot fluid to rise and the cold fluid to descend initially. This distribution of hot and cold fluid in the liquid phase is shown in figure 4.17. The twisting of contours that is occurring in the corners of the liquid region shows the effect convection is having on the temperature distribution. In contrast figure 4.20 shows the fluid motion 30 time units later and the temperature distribution is quite different. In this case the temperature of the fluid is rapidly approaching the critical temperature $\tilde{T}_{lc}$ everywhere, with only a small area in the centre of the liquid region which is above this value. The fluid in the half region $0 \leq x \leq 1$, $-1 \leq z \leq 1$ is being cooled on three of its boundaries and therefore it is these three sides of the liquid region which will cool most rapidly. The resulting distribution which has a pocket of warmer fluid residing in the centre of the region is therefore expected. Furthermore, in the bottom left hand corner of the liquid region in figure 4.20 a small vertical plume of cold fluid can be seen rising from the lower boundary. The fluid motion around the region of hot fluid and the rising plume of cold fluid can be seen in the vorticity and streamfunction plots as two vortices.

Figures 4.18 and 4.21 show the streamfunction profiles at times $t = 30.0$ (60.35 secs) and $t = 60.0$ (120.70 secs) respectively. The orientation of the surface plot is again different to the contour plots to enable the details to be seen more clearly. In figure 4.18 four vortices are shown; two positive with clockwise rotation and two negative with anticlockwise rotation. As time increases the liquid region continues to cool down, resulting in the temperature approaching $\tilde{T}_{lc}$ everywhere. Figure 4.21 shows the streamfunction 30 time steps later and three vortices can be seen, two positive with clockwise rotation and the other negative with anticlockwise rotation. At subsequent time steps the temperature in the liquid region will be below $\tilde{T}_{lc}$ everywhere, resulting in the formation of a single anticlockwise rotating vortex that will remain until the whole region freezes.

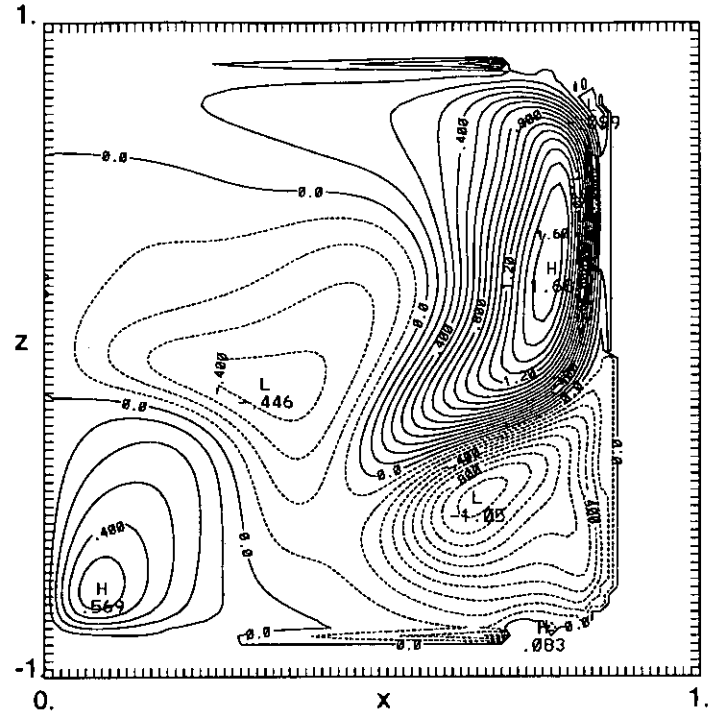

(a) Contours of the vorticity ω from -1.0 to 1.6 at intervals 0.10

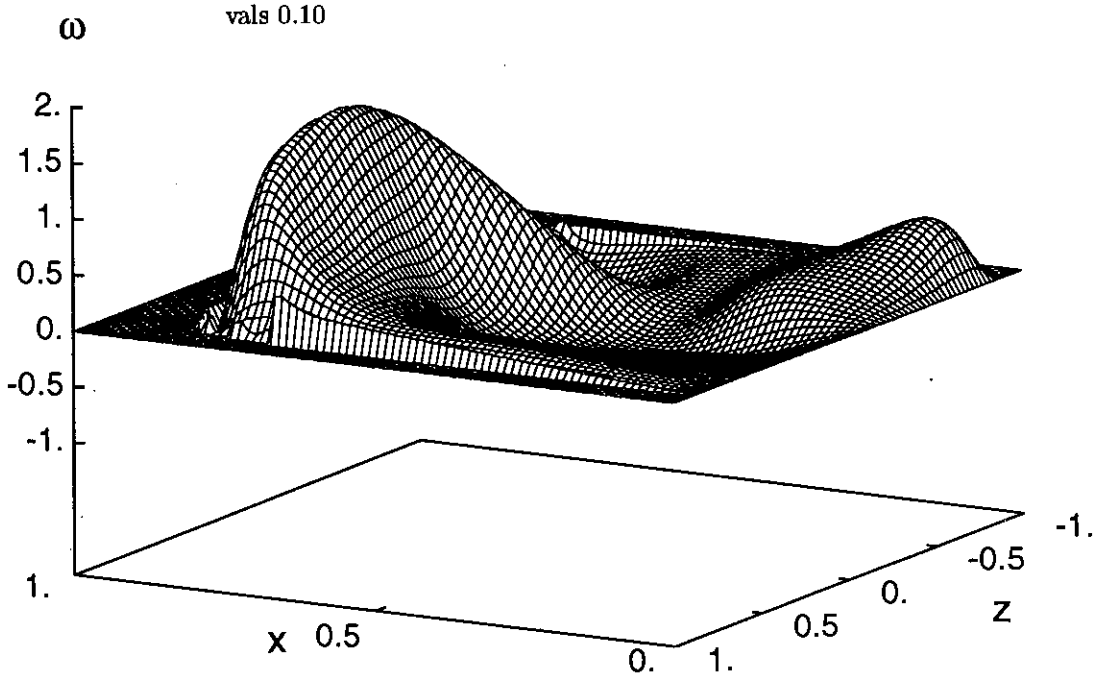

(b) Surface plot of vorticity ω at alternate each alternate row of mesh

Figure 4.16: Vorticity distribution at time $t = 30.0$ with initial conditions $T_{l0} = 0.75$ and $\omega_0 = 5.0 \times 10^{-3}$. The spatial and time steps for the solid and liquid regions are $\Delta s_s = 5.0 \times 10^{-2}$, $\Delta s_l = 1.25 \times 10^{-2}$, $\Delta t_s = 15.0$ and $\Delta t_l = 6.0 \times 10^{-3}$ respectively. The dimensionless constants for water are given in table 4.1

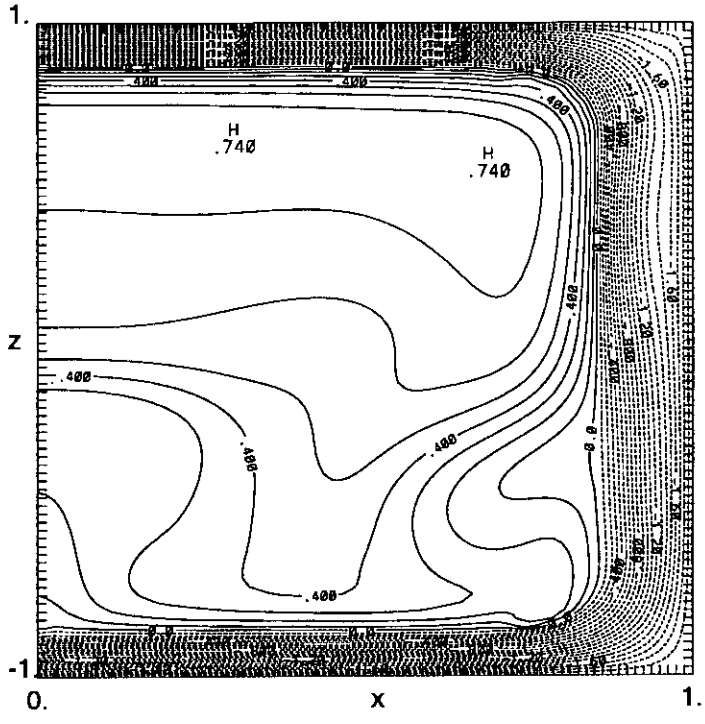

(a) Isotherms from -2.0 to 0.70 at intervals of 0.10

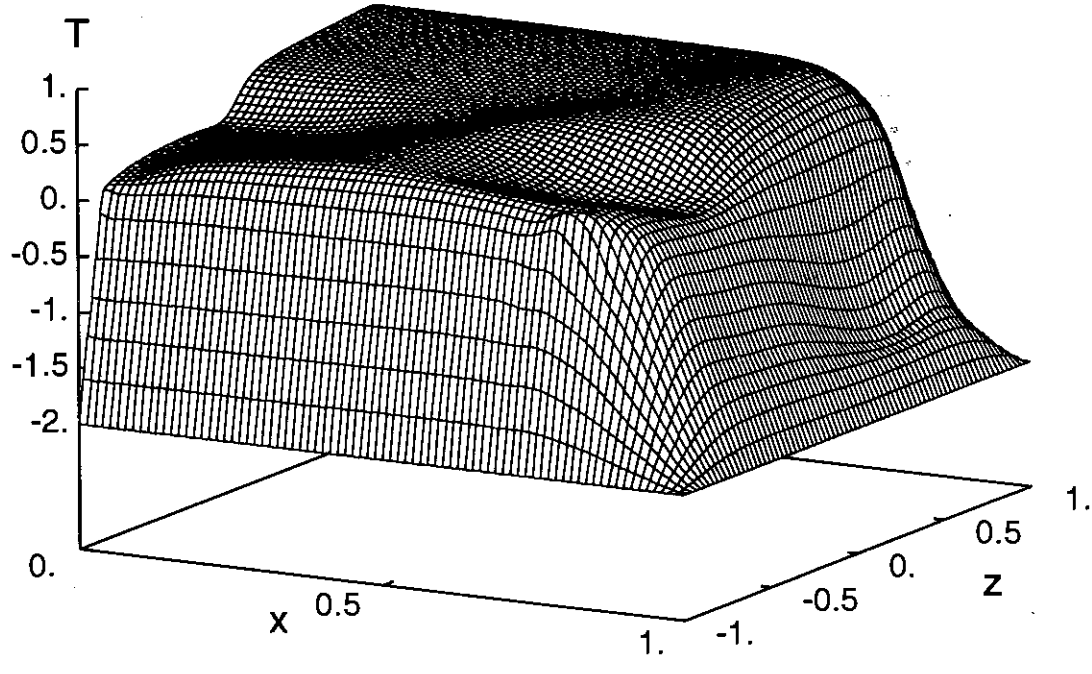

(b) Surface plot of temperature T at alternate each alternate row of mesh

Figure 4.17: Temperature distribution at time $t = 30.0$ with initial conditions $T_{l0} = 0.75$ and $\omega_0 = 5.0 \times 10^{-3}$. The spatial and time steps for the solid and liquid regions are $\Delta s_s = 5.0 \times 10^{-2}$, $\Delta s_l = 1.25 \times 10^{-2}$, $\Delta t_s = 15.0$ and $\Delta t_l = 6.0 \times 10^{-3}$ respectively. The dimensionless constants for water are given in table 4.1

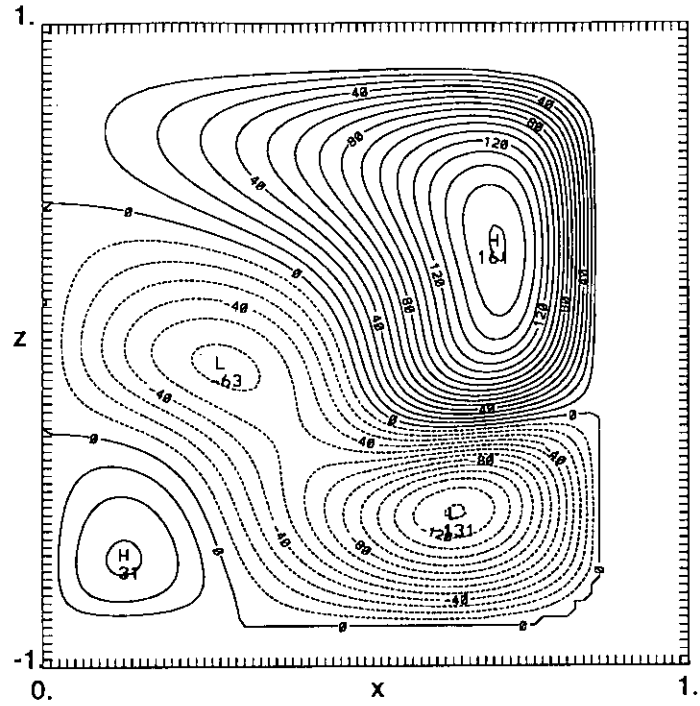

(a) Streamlines: contours of the streamfunction ψ from -1.3×10^{-2} to 1.6×10^{-2} at intervals of 1.0×10^{-3}. (Scaled by 10^4)

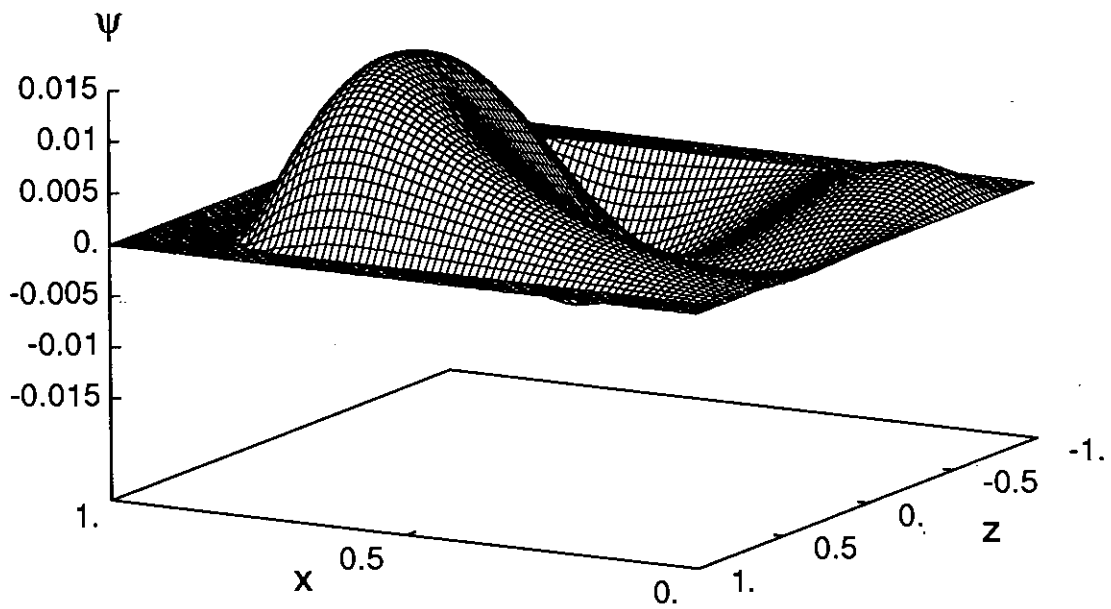

(b) Surface plot of streamfunction ψ at alternate each alternate row of mesh

Figure 4.18: Streamfunction distribution at time $t = 30.0$ with initial conditions $T_{l0} = 0.75$ and $\omega_0 = 5.0 \times 10^{-3}$. The spatial and time steps for the solid and liquid regions are $\Delta s_s = 5.0 \times 10^{-2}$, $\Delta s_l = 1.25 \times 10^{-2}$, $\Delta t_s = 15.0$ and $\Delta t_l = 6.0 \times 10^{-3}$ respectively. The dimensionless constants for water are given in table 4.1

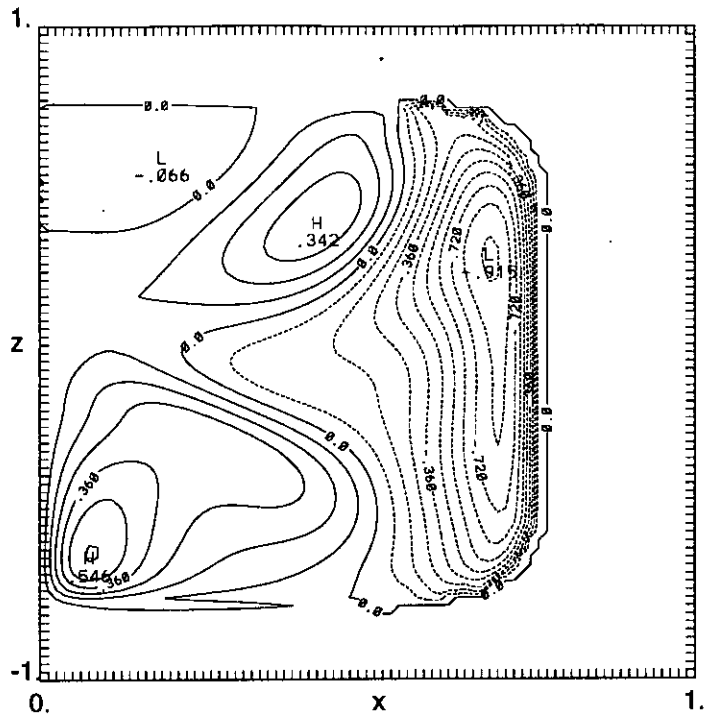

(a) Contours of the vorticity ω from -0.90 to 0.54 at intervals 0.09

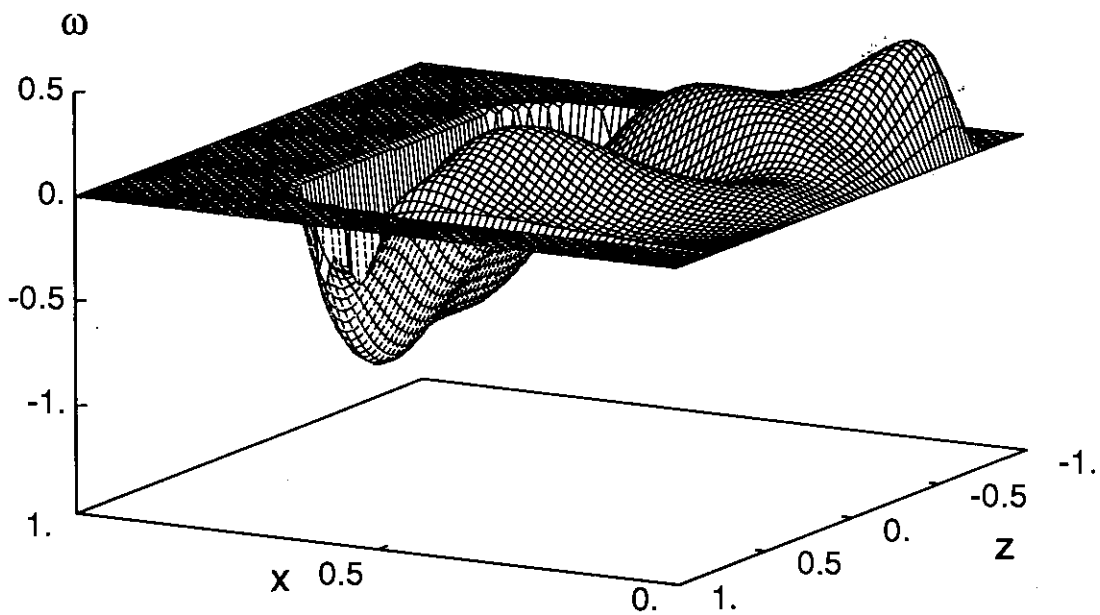

(b) Surface plot of vorticity ω at alternate each alternate row of mesh

Figure 4.19: Vorticity distribution at time $t = 60.0$ with initial conditions $T_{l0} = 0.75$ and $\omega_0 = 5.0 \times 10^{-3}$. The spatial and time steps for the solid and liquid regions are $\Delta s_s = 5.0 \times 10^{-2}$, $\Delta s_l = 1.25 \times 10^{-2}$, $\Delta t_s = 15.0$ and $\Delta t_l = 6.0 \times 10^{-3}$ respectively. The dimensionless constants for water are given in table 4.1

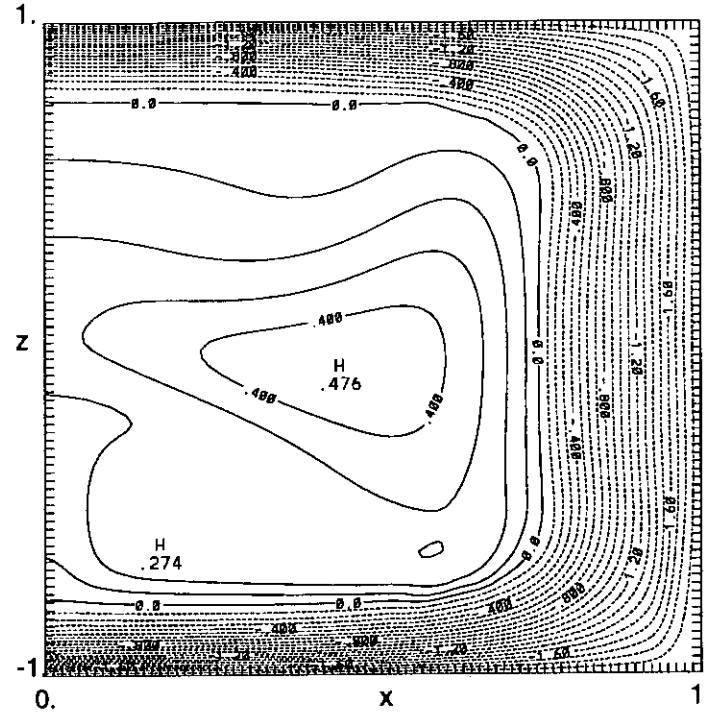

(a) Isotherms from -2.0 to 0.40 at intervals of 0.10

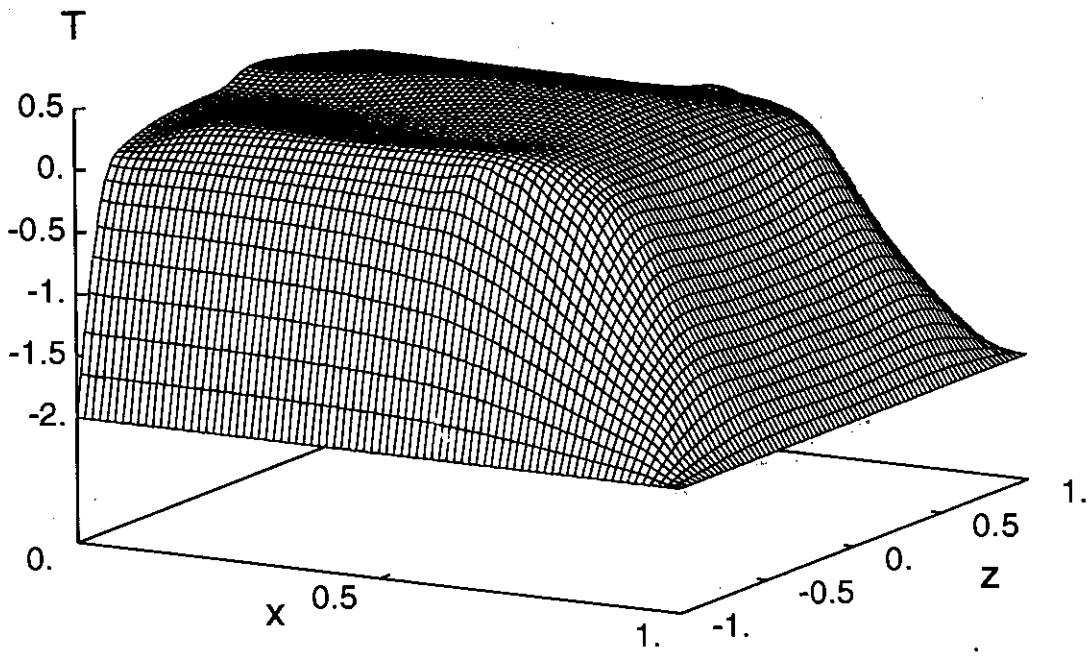

(b) Surface plot of temperature T at alternate each alternate row of mesh

Figure 4.20: Temperature distribution at time $t = 60.0$ with initial conditions $T_{l0} = 0.75$ and $\omega_0 = 5.0 \times 10^{-3}$. The spatial and time steps for the solid and liquid regions are $\Delta s_s = 5.0 \times 10^{-2}$, $\Delta s_l = 1.25 \times 10^{-2}$, $\Delta t_s = 15.0$ and $\Delta t_l = 6.0 \times 10^{-3}$ respectively. The dimensionless constants for water are given in table 4.1

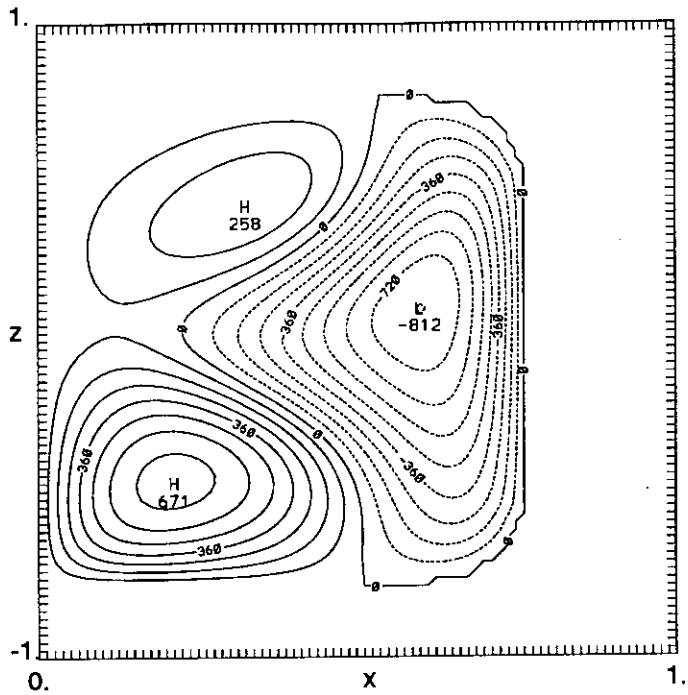

(a) Streamlines: contours of the streamfunction ψ from -8.1×10^{-3} to 6.3×10^{-3} at intervals of 9.0×10^{-4}. (Scaled by 10^5)

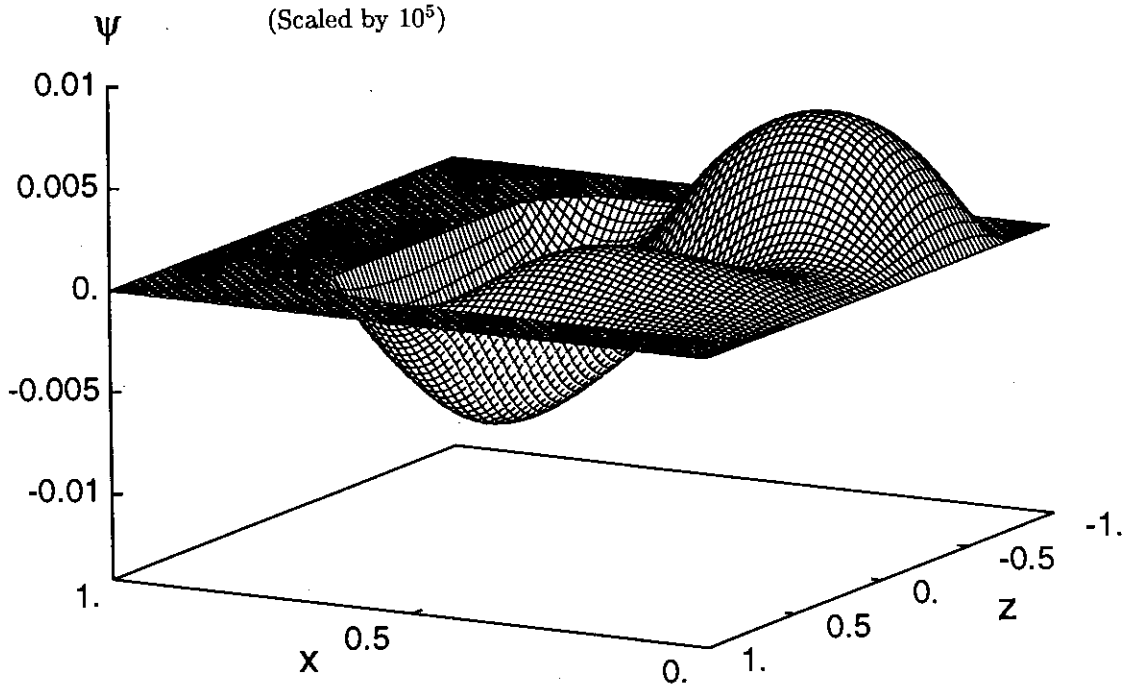

(b) Surface plot of streamfunction ψ at alternate each alternate row of mesh

Figure 4.21: Streamfunction distribution at time $t = 60.0$ with initial conditions $T_{l0} = 0.75$ and $\omega_0 = 5.0 \times 10^{-3}$. The spatial and time steps for the solid and liquid regions are $\Delta s_s = 5.0 \times 10^{-2}$, $\Delta s_l = 1.25 \times 10^{-2}$, $\Delta t_s = 15.0$ and $\Delta t_l = 6.0 \times 10^{-3}$ respectively. The dimensionless constants for water are given in table 4.1

Finally, an initial temperature condition of $T_{l0} = 1.50$ $(15\,^{\circ}C)$ was considered. The other parameters for this simulation were taken to be the same as those given for the initial condition $T_{l0} = 0.40$ $(4\,^{\circ}C)$, except that the time steps for the solid and liquid phase calculation were taken to be $\Delta t_s = 18.0$ and $\Delta t_l = 9.0 \times 10^{-3}$ respectively.

In this case the initial temperature was chosen to be considerably larger than the critical temperature $\tilde{T}_{lc} = 3.55\,^{\circ}C$ to allow the fluid to circulate for a longer period of time. As the fluid is cooled the fluid flow behaviour exhibited in this case is similar to that of the previous simulations for $T_{l0} = 0.40$ $(4\,^{\circ}C)$ and $T_{l0} = 0.75$ $(7.5\,^{\circ}C)$. Here, as in the previous examples, a single vortex is not expected to form initially since the fluid close to the phase change front will be cooled to below $\tilde{T}_{lc}$ almost immediately. This forces the fluid there to form vortices that are counter rotating to the bulk of the hotter fluid in the centre of the region. Figures 4.22 to 4.30 show contour and surface plots of vorticity, temperature and streamfunction at non-dimensional times $t = 36.0$ (72.42 secs), $t = 54.0$ (108.63 secs) and $t = 90.0$ (181.06 secs) for an initial condition of $T_{l0} = 1.50$ $(15\,^{\circ}C)$.

The vorticity profiles at times $t = 36.0$ (72.42 secs), $t = 54.0$ (108.63 secs) and $t = 90.0$ (181.06 secs) are shown in figures 4.22, 4.25 and 4.28 respectively. The surface plots have again been orientated differently to the contour plots to enable the features of these plots to be seen more clearly. In figure 4.22 there are six distinct vortices; three positive with clockwise rotation and three negative with anticlockwise rotation. The more dominant of these vortices can be seen more clearly in the associated streamfunction plots in figure 4.24. Freezing the region for a further 18.0 time units results in the number of vortices in the liquid region being reduced to four, which can be seen in figure 4.25. Here there are two negative vortices with anticlockwise rotation and two positive vortices with clockwise rotation. The freezing of the right hand boundary of the liquid region forces the temperature there down below the critical temperature $\tilde{T}_{lc}$ very rapidly. Consequently an anticlockwise rotating vortex is formed there that dominates the flow. As the temperature of the region decreases, the anticlockwise rotating vortex formed from cold water increases in size and the clockwise vortices formed from warm water disappear. The distribution of vortices in this case is similar to that at time $\tilde{t} = 120.70$ secs for an initial condition of $T_{l0} = 0.75$ $(7.5\,^{\circ}C)$ shown in figure 4.19. Furthermore the small clockwise rotating vortex occurring in the bottom left hand corner of the liquid region in figure 4.25 also appears as a significant feature in figure 4.19. Figure 4.28 shows the vorticity profiles after a further 36.0 time units. In this case there are only two vortices; one negative with anticlockwise rotation and one positive with clockwise rotation. At this time the

temperature distribution is below the critical temperature $\tilde{T}_{lc}$ everywhere in the liquid region. This results in the vorticity distribution approaching that of figure 4.10 at time $\tilde{t} = 80.47$ secs with the exception of the clockwise rotating vortex in the bottom left hand corner of the liquid region in figure 4.28. This second vortex is rapidly decreasing in size as the liquid cools. Furthermore the small positive vortex occurring in figure 4.10 is also present in figure 4.28 however, its presence is dominated by the larger positive vortices occurring in the liquid region.

The temperature profiles both ahead of and behind the phase change front at times $t = 36.0$ (72.42 secs), $t = 54.0$ (108.63 secs) and $t = 90.0$ (181.06 secs) are shown in figures 4.23, 4.26 and 4.29 respectively. Again a three point smoothing routine has been applied at the interface of the solid and liquid phases to eliminate the ragged mesh points there. Since the initial condition is larger than the critical temperature $\tilde{T}_{lc}$ we expect the bulk of the hot fluid to rise and the cold fluid to descend, except at the phase change front where the temperature is less than T_{lc}. This distribution of hot and cold fluid in the liquid phase is shown in 4.23. A similar distribution is shown at time $\tilde{t} = 60.35$ secs in figure 4.17 for an initial condition of $T_{l0} = 0.75$ $(7.5\,^{\circ}C)$. The distribution of temperature in the region is shown after a further 18.0 time units in figure 4.26. In this case a small area of fluid with temperature greater than the critical temperature $\tilde{T}_{lc}$ is located in the top left hand corner of the liquid region. This pocket of hotter fluid has been forced to this region by the cold fluid, which is below the critical temperature $\tilde{T}_{lc}$ and on the right hand side of the region and is rising towards the upper boundary. Furthermore in the bottom left hand corner of the liquid region a small plume of cold fluid is rising with a clockwise rotation from the lower boundary to buoy up the pocket of hot fluid. Figure 4.29 shows the temperature distribution after a further 36.0 time steps. At this time the entire fluid is below the critical temperature $\tilde{T}_{lc}$. Thus the cold fluid is rising and the hotter fluid is descending towards the bottom of the liquid region. The small plume of cold fluid that was rising from the lower boundary in the bottom left hand corner of the liquid region in figures 4.23 and 4.26 can still be seen in figure 4.29. However the size of this pool of fluid has decreased. This is because the warmest part of the liquid region is to be found just above the lower boundary and the cold plume need not penetrate too far upwards into the region to be warmed itself and descend.

The streamfunction profiles at times $t = 36.0$ (72.42 secs), $t = 54.0$ (108.63 secs) and $t = 90.0$ (181.06 secs) are shown in figures 4.24, 4.27 and 4.30 respectively. The surface plots have again been orientated differently to the contour plots to enable the features of these plots to be seen more clearly. In figure 4.24

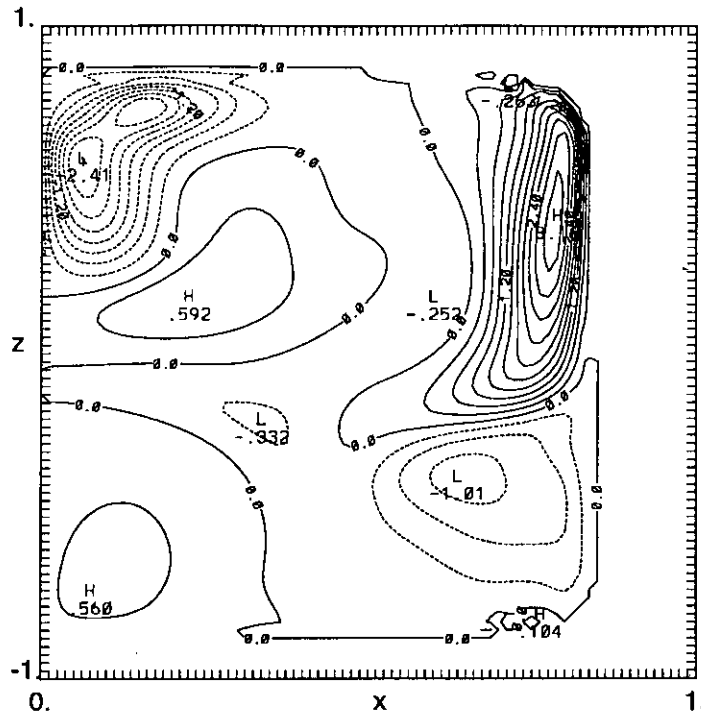

(a) Contours of the vorticity ω from -2.4 to 3.0 at intervals 0.30

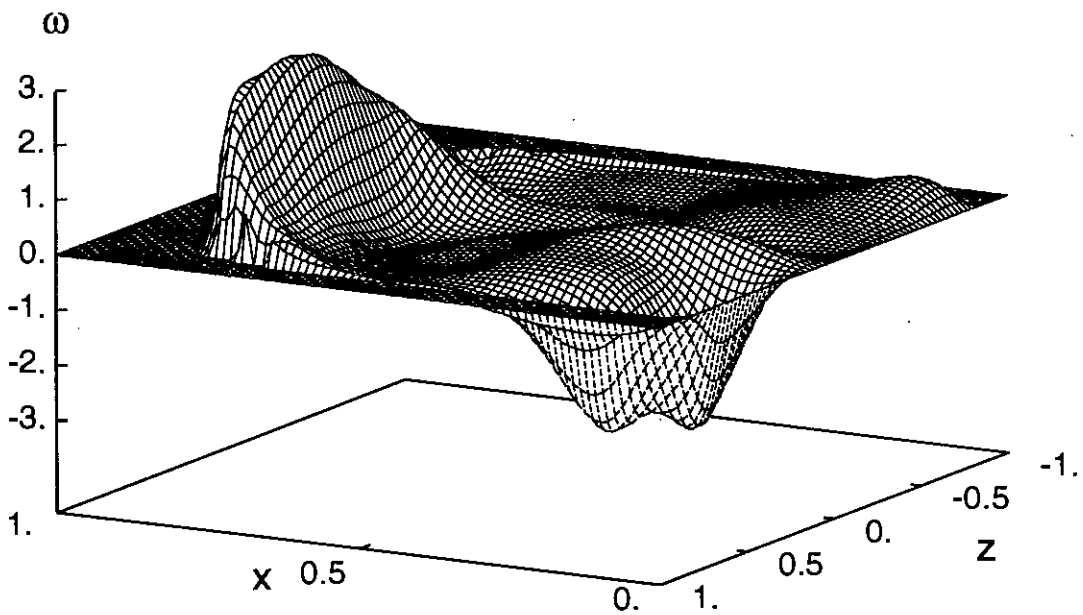

(b) Surface plot of vorticity ω at alternate each alternate row of mesh

Figure 4.22: Vorticity distribution at time $t = 36.0$ with initial conditions $T_{l0} = 1.50$ and $\omega_0 = 5.0 \times 10^{-3}$. The spatial and time steps for the solid and liquid regions are $\Delta s_s = 5.0 \times 10^{-2}$, $\Delta s_l = 1.25 \times 10^{-2}$, $\Delta t_s = 18.0$ and $\Delta t_l = 9.0 \times 10^{-3}$ respectively. The dimensionless constants for water are given in table 4.1

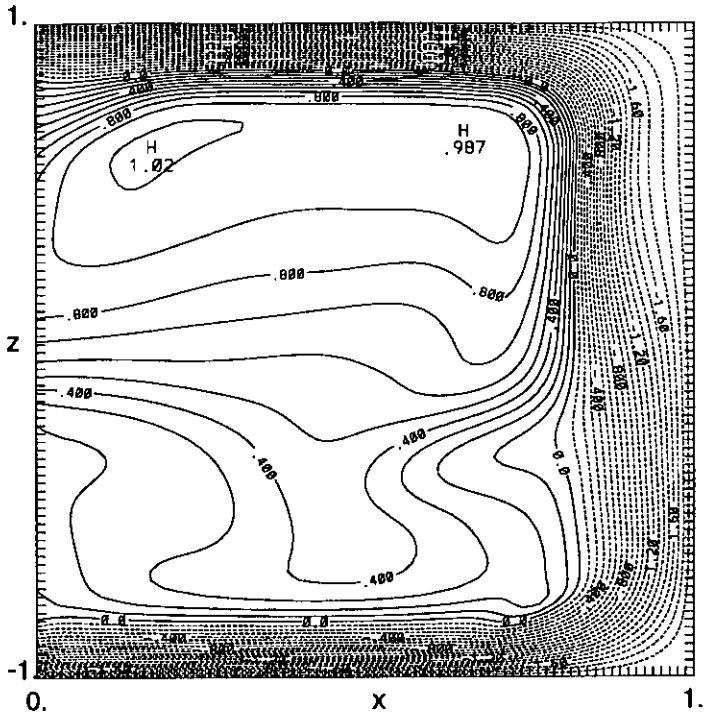

(a) Isotherms from -2.0 to 1.0 at intervals of 0.10

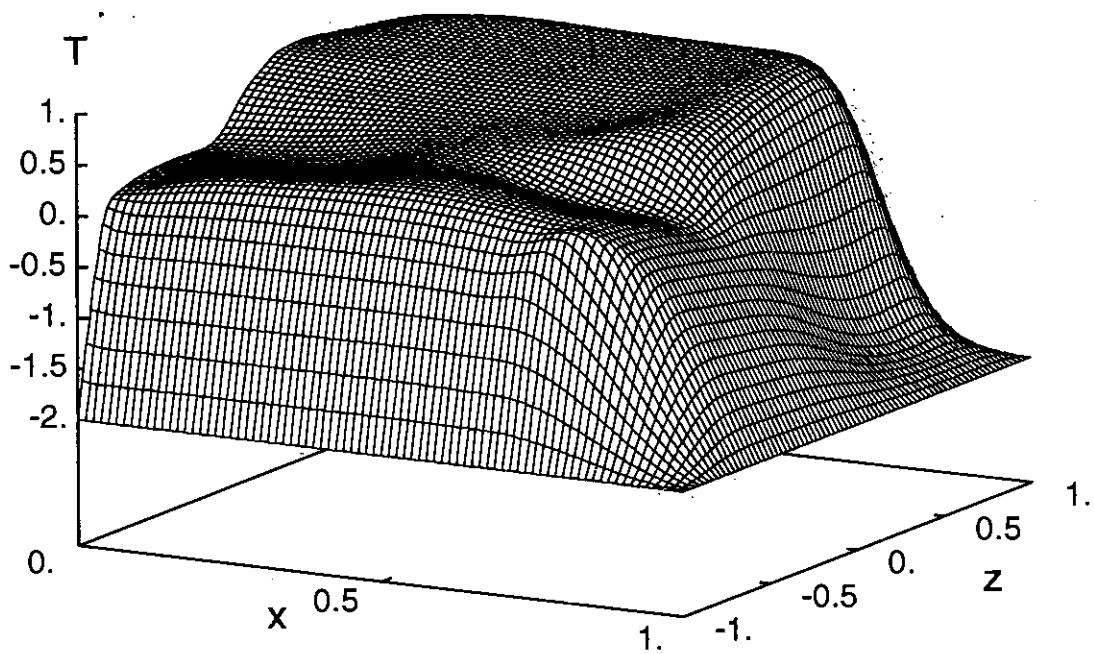

(b) Surface plot of temperature T at alternate each alternate row of mesh

Figure 4.23: Temperature distribution at time $t = 36.0$ with initial conditions $T_{l0} = 1.50$ and $\omega_0 = 5.0 \times 10^{-3}$. The spatial and time steps for the solid and liquid regions are $\Delta s_s = 5.0 \times 10^{-2}$, $\Delta s_l = 1.25 \times 10^{-2}$, $\Delta t_s = 18.0$ and $\Delta t_l = 9.0 \times 10^{-3}$ respectively. The dimensionless constants for water are given in table 4.1

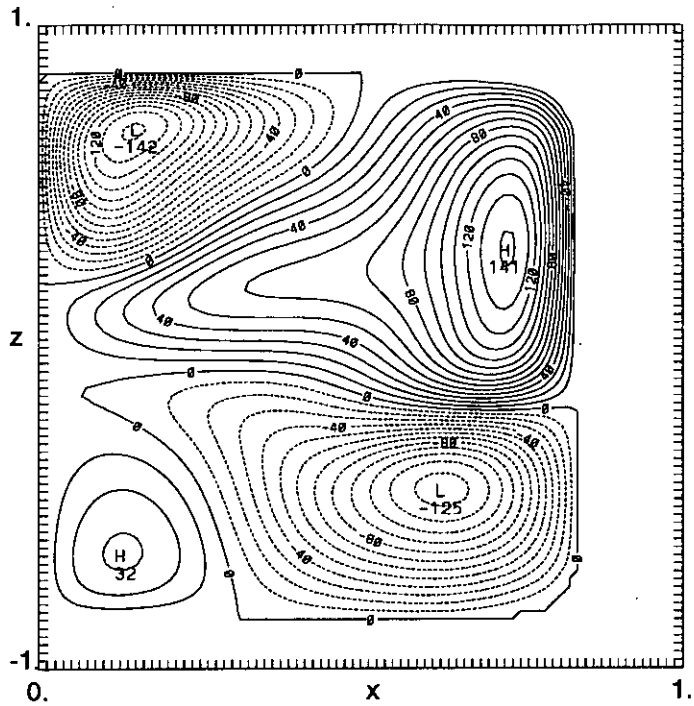

(a) Streamlines: contours of the streamfunction ψ from -1.4×10^{-2} to 1.4×10^{-2} at intervals of 1.0×10^{-3}. (Scaled by 10^4)

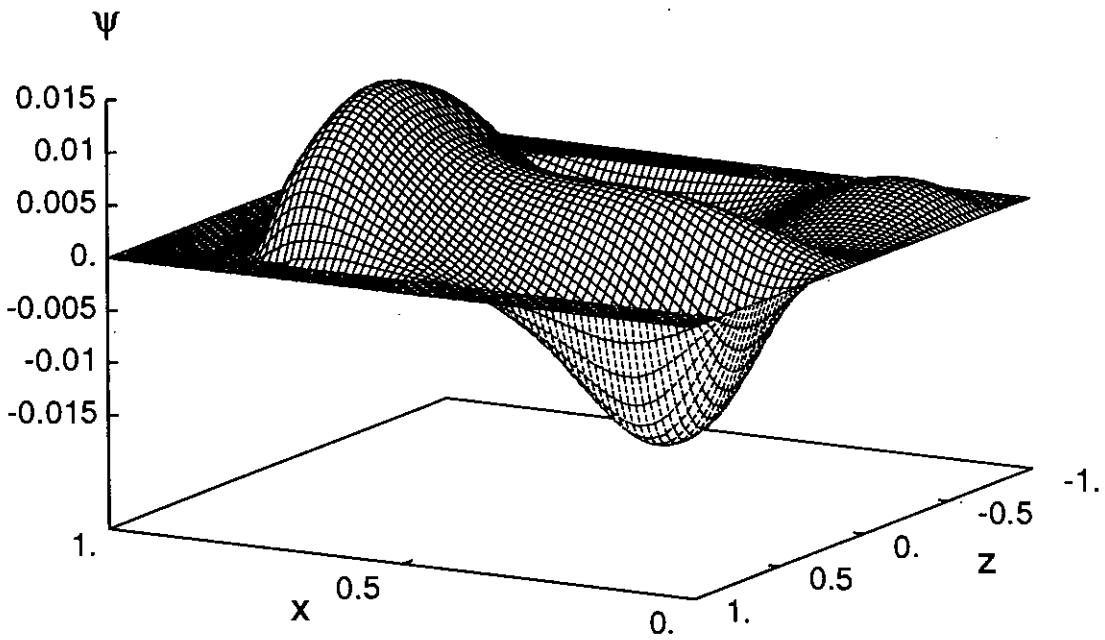

(b) Surface plot of streamfunction ψ at alternate each alternate row of mesh

Figure 4.24: Streamfunction distribution at time $t = 36.0$ with initial conditions $T_{l0} = 1.50$ and $\omega_0 = 5.0 \times 10^{-3}$. The spatial and time steps for the solid and liquid regions are $\Delta s_s = 5.0 \times 10^{-2}$, $\Delta s_l = 1.25 \times 10^{-2}$, $\Delta t_s = 18.0$ and $\Delta t_l = 9.0 \times 10^{-3}$ respectively. The dimensionless constants for water are given in table 4.1

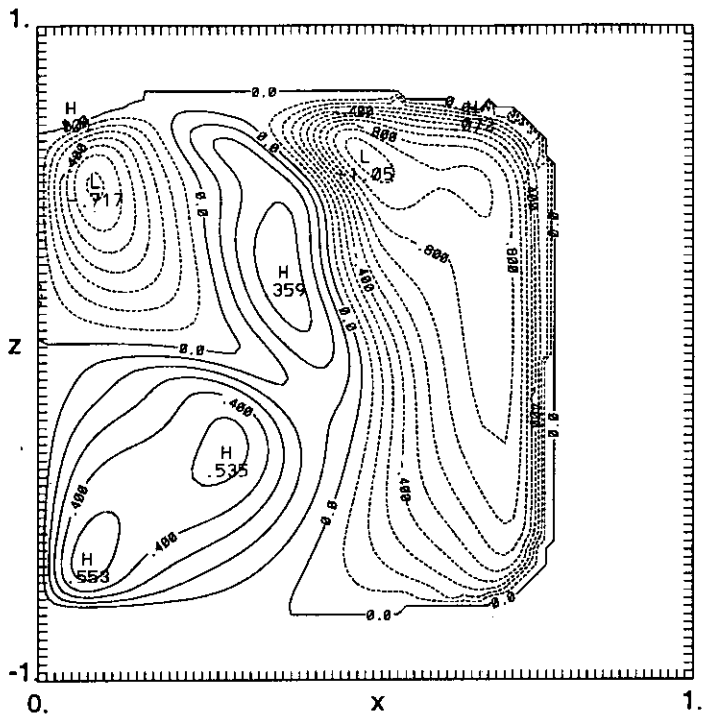

(a) Contours of the vorticity ω from -1.0 to 0.5 at intervals 0.10

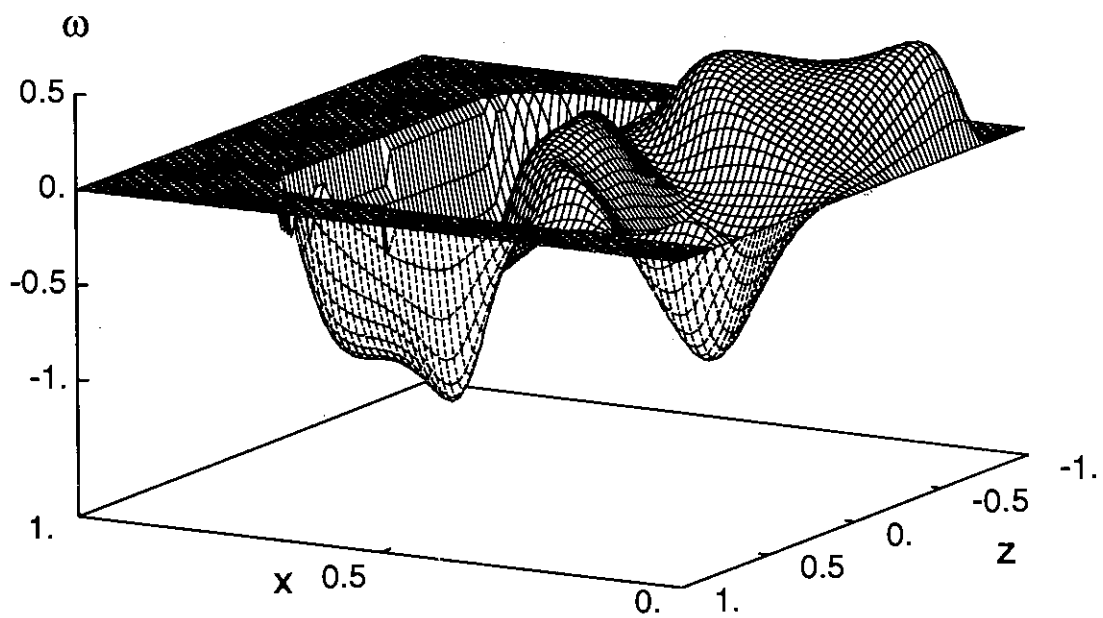

(b) Surface plot of vorticity ω at alternate each alternate row of mesh

Figure 4.25: Vorticity distribution at time $t = 54.0$ with initial conditions $T_{l0} = 1.50$ and $\omega_0 = 5.0 \times 10^{-3}$. The spatial and time steps for the solid and liquid regions are $\Delta s_s = 5.0 \times 10^{-2}$, $\Delta s_l = 1.25 \times 10^{-2}$, $\Delta t_s = 18.0$ and $\Delta t_l = 9.0 \times 10^{-3}$ respectively. The dimensionless constants for water are given in table 4.1

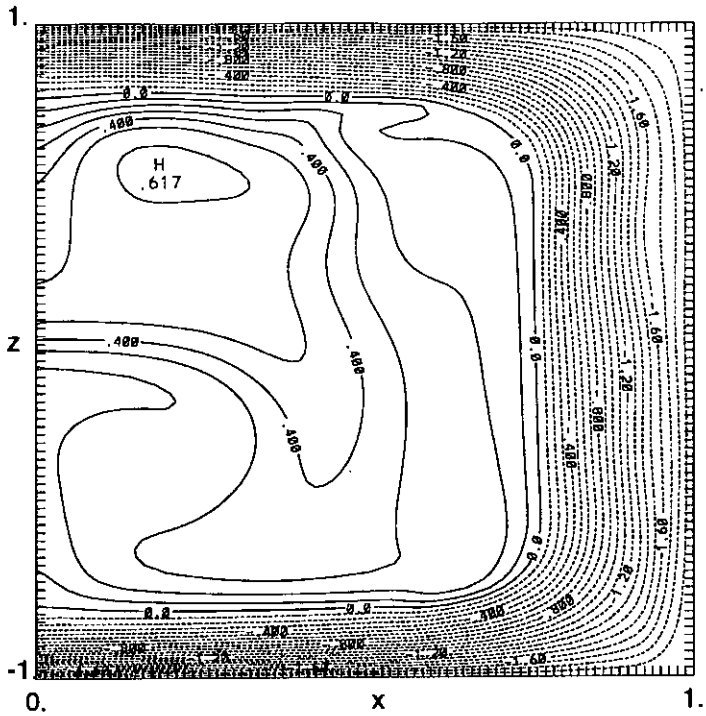

(a) Isotherms from -2.0 to 0.60 at intervals of 0.10

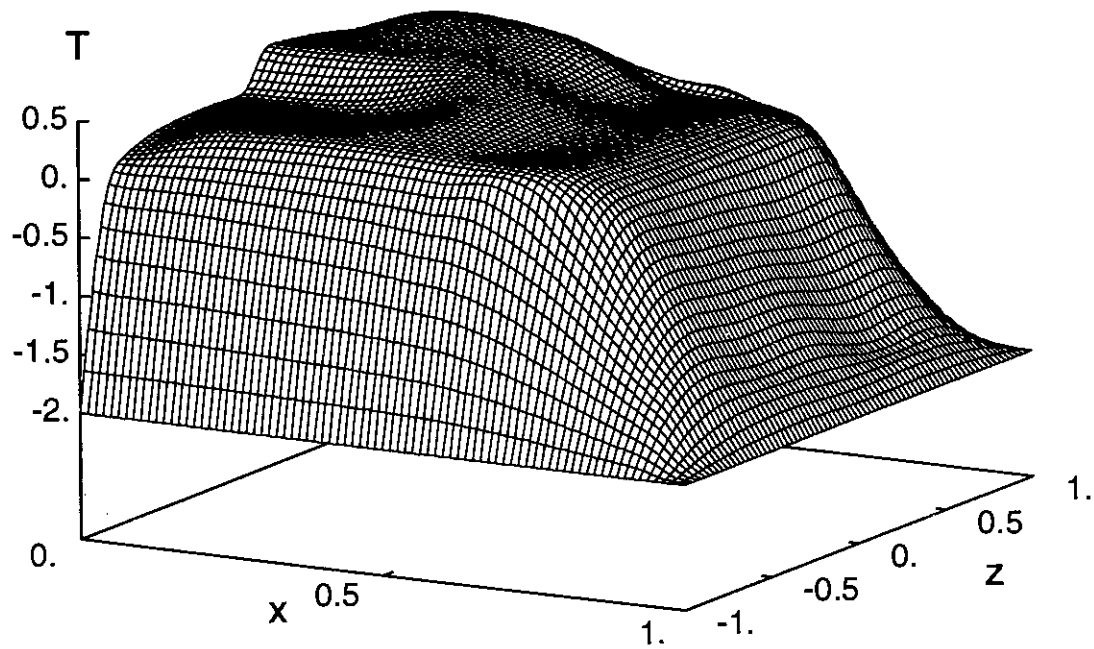

(b) Surface plot of temperature T at alternate each alternate row of mesh

Figure 4.26: Temperature distribution at time $t = 54.0$ with initial conditions $T_{l0} = 1.50$ and $\omega_0 = 5.0 \times 10^{-3}$. The spatial and time steps for the solid and liquid regions are $\Delta s_s = 5.0 \times 10^{-2}$, $\Delta s_l = 1.25 \times 10^{-2}$, $\Delta t_s = 18.0$ and $\Delta t_l = 9.0 \times 10^{-3}$ respectively. The dimensionless constants for water are given in table 4.1

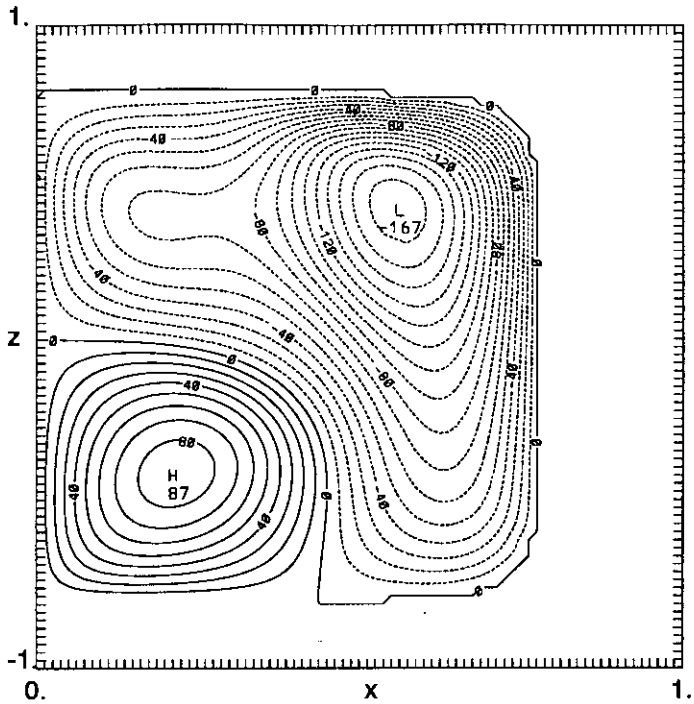

(a) Streamlines: contours of the streamfunction ψ from -1.6×10^{-2} to 8.0×10^{-3} at intervals of 1.0×10^{-3}. (Scaled by 10^4)

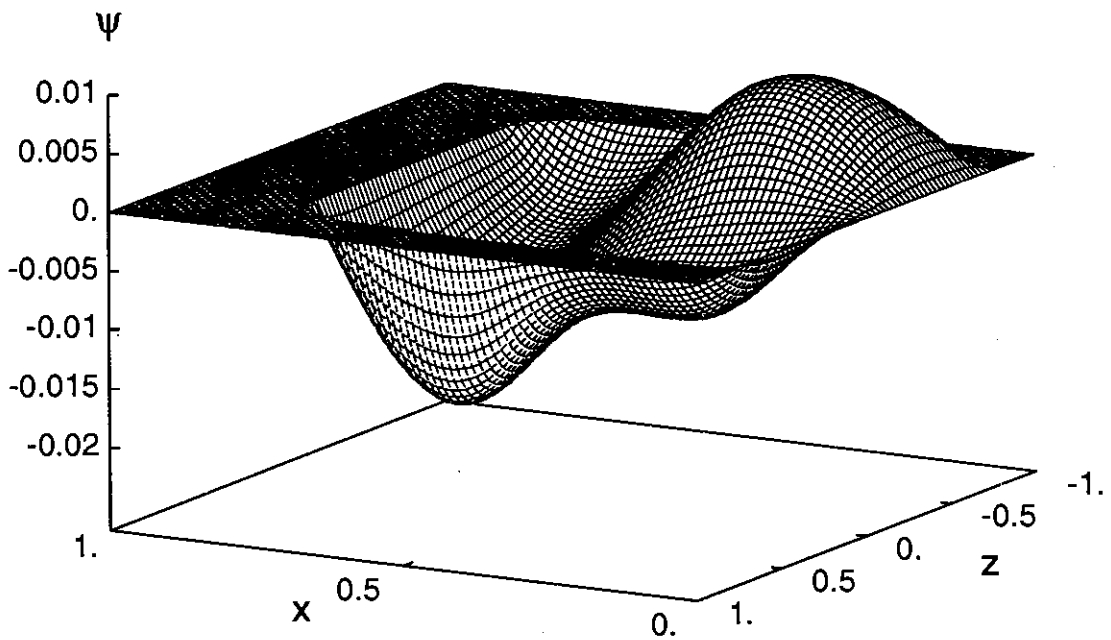

(b) Surface plot of streamfunction ψ at alternate each alternate row of mesh

Figure 4.27: Streamfunction distribution at time $t = 54.0$ with initial conditions $T_{l0} = 1.50$ and $\omega_0 = 5.0 \times 10^{-3}$. The spatial and time steps for the solid and liquid regions are $\Delta s_s = 5.0 \times 10^{-2}$, $\Delta s_l = 1.25 \times 10^{-2}$, $\Delta t_s = 18.0$ and $\Delta t_l = 9.0 \times 10^{-3}$ respectively. The dimensionless constants for water are given in table 4.1

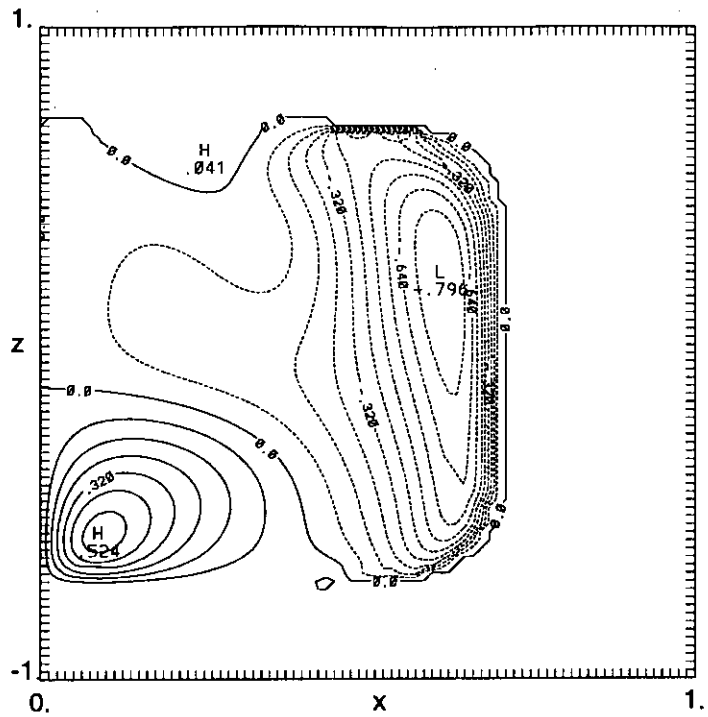

(a) Contours of the vorticity ω from -0.72 to 0.49 at intervals 0.08

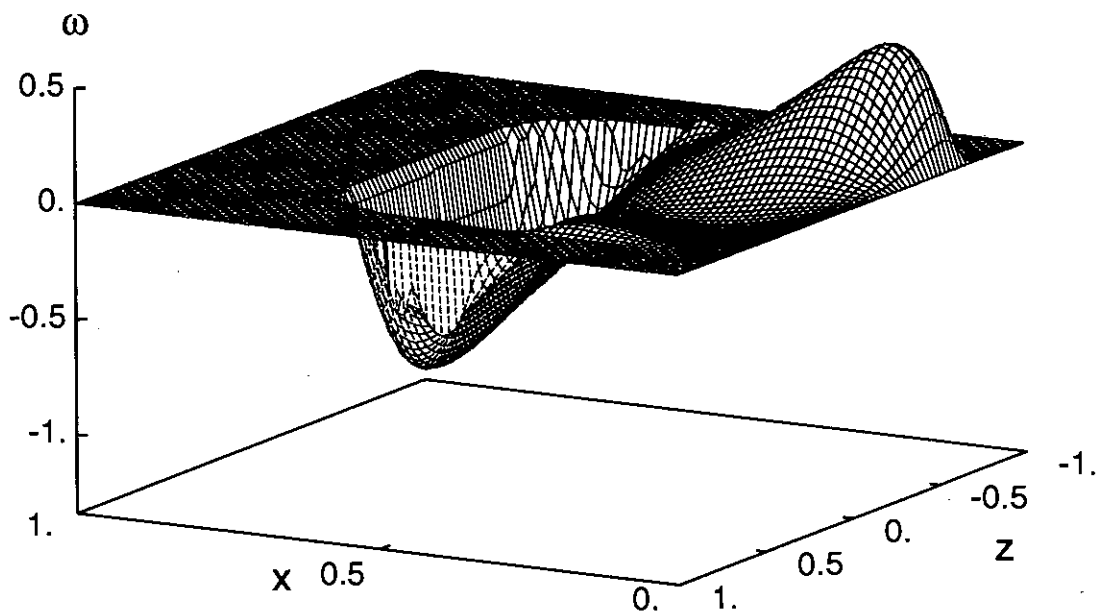

(b) Surface plot of vorticity ω at alternate each alternate row of mesh

Figure 4.28: Vorticity distribution at time $t = 90.0$ with initial conditions $T_{l0} = 1.50$ and $\omega_0 = 5.0 \times 10^{-3}$. The spatial and time steps for the solid and liquid regions are $\Delta s_s = 5.0 \times 10^{-2}$, $\Delta s_l = 1.25 \times 10^{-2}$, $\Delta t_s = 18.0$ and $\Delta t_l = 9.0 \times 10^{-3}$ respectively. The dimensionless constants for water are given in table 4.1

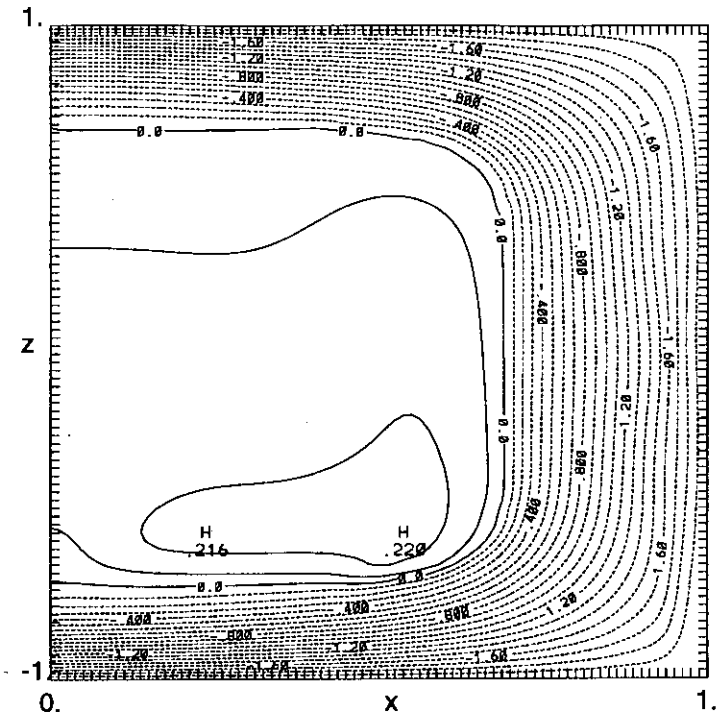

(a) Isotherms from -2.0 to 0.20 at intervals of 0.10

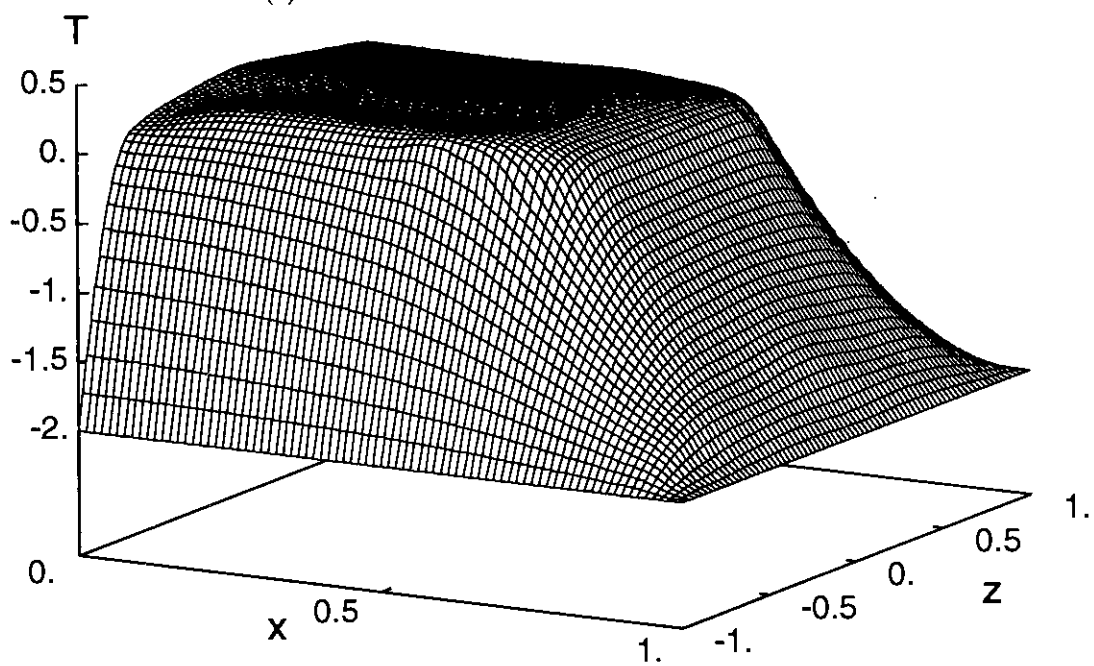

(b) Surface plot of temperature T at alternate each alternate row of mesh

Figure 4.29: Temperature distribution at time $t = 90.0$ with initial conditions $T_{l0} = 1.50$ and $\omega_0 = 5.0 \times 10^{-3}$. The spatial and time steps for the solid and liquid regions are $\Delta s_s = 5.0 \times 10^{-2}$, $\Delta s_l = 1.25 \times 10^{-2}$, $\Delta t_s = 18.0$ and $\Delta t_l = 9.0 \times 10^{-3}$ respectively. The dimensionless constants for water are given in table 4.1

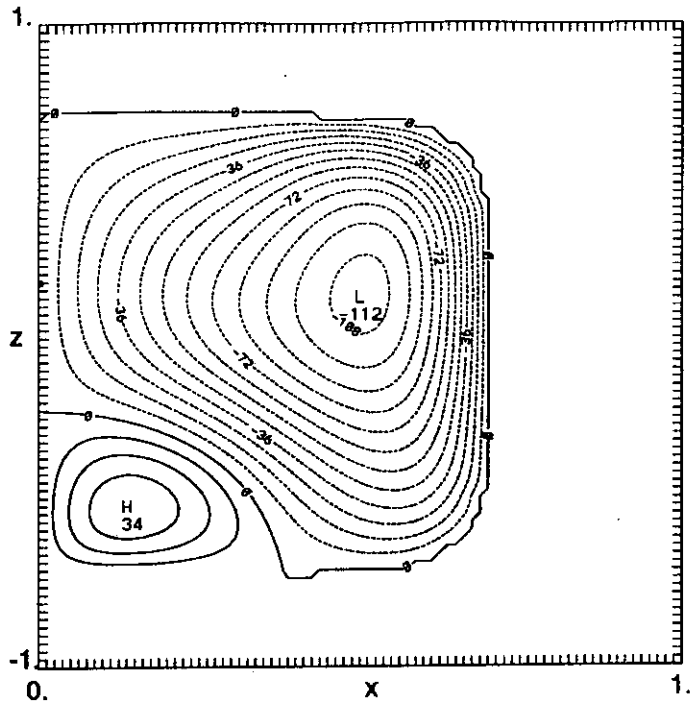

(a) Streamlines: contours of the streamfunction ψ from -1.08×10^{-2} to 2.7×10^{-3} at intervals of 9.0×10^{-4}. (Scaled by 10^4)

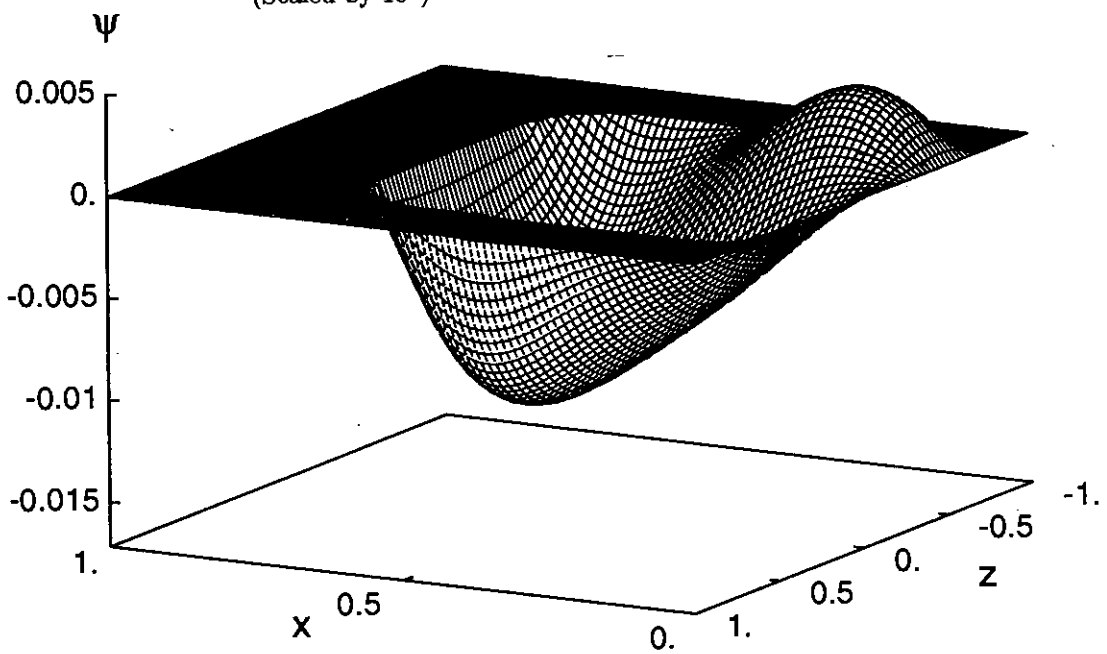

(b) Surface plot of streamfunction ψ at alternate each alternate row of mesh

Figure 4.30: Streamfunction distribution at time $t = 90.0$ with initial conditions $T_{l0} = 1.50$ and $\omega_0 = 5.0 \times 10^{-3}$. The spatial and time steps for the solid and liquid regions are $\Delta s_s = 5.0 \times 10^{-2}$, $\Delta s_l = 1.25 \times 10^{-2}$, $\Delta t_s = 18.0$ and $\Delta t_l = 9.0 \times 10^{-3}$ respectively. The dimensionless constants for water are given in table 4.1

Quantity	Symbol	Value
Thermal diffusivity (liquid)	D_l	1.513486×10^{-4}
Thermal diffusivity (solid)	D_s	1.356830×10^{-3}
Thermal conductivity	K	4.151624
Prandtl number	Pr	7.519227
Rayleigh number	Ra	5.805997×10^{6}
Stefan number	S_t	4.721908×10^{4}
Kinematic viscosity	v_l	1.138024×10^{-3}

Table 4.2: Values of non-dimensional parameters for water generated with length scale $\tilde{d}_a$; see Appendix A : table A.1

four vortices are shown; two positive with clockwise rotation and two negative with anticlockwise rotation. After a further 18.0 time units the temperature in the liquid region has cooled down further, resulting in a reduction in the number of vortices to only the two shown in figure 4.27. In this case there is a dominant negative vortex with anticlockwise rotation, corresponding to fluid below the critical temperature $\tilde{T}_{lc}$ on the right hand side of the liquid region, and a positive vortex with clockwise rotation, corresponding to the cold fluid also below $\tilde{T}_{lc}$ rising from the lower boundary. Finally figure 4.30 shows that after a further 36.0 time units the two vortices have persisted. In this case the temperature everywhere in the region is below the critical temperature $\tilde{T}_{lc}$. The negative vortex continues to dominate the flow with the positive vortex being reduced in size. Figure 4.21 shows the streamfunction plot for an initial condition of $T_{l0} = 0.75$ $(7.5\,^{\circ}C)$ at time $\tilde{t} = 120.70$ secs. In this case there is a similar pair of vortices to those of figures 4.27 and 4.30 with an additional positive vortex which is rapidly diminishing in size. The magnitude of the vortices in figures 4.27 ($\tilde{t} = 108.63$ secs) and 4.30 ($\tilde{t} = 181.06$ secs) are slightly larger than those shown in figure 4.21 ($\tilde{t} = 120.70$ secs). However of these vortices are rapidly approaching the magnitude of those shown in figure 4.30 and at subsequent times the only real difference being the position of the phase change front.

For each of the three different initial conditions the previous simulations were repeated with a refined mesh to confirm that the number of vortices occurring in each case was not scaling with the size of the grid. It was found that in each case on the refined mesh the problem yielded exactly the same numerical results with the only difference being an improvement in the definition of the phase change fronts in each of the vorticity, temperature and streamfunction plots.

The numerical method for two-phase Stefan problems with convection was applied for different values of the initial temperature $\tilde{T}_{l0}$, in the range $0\,^{\circ}C$ to

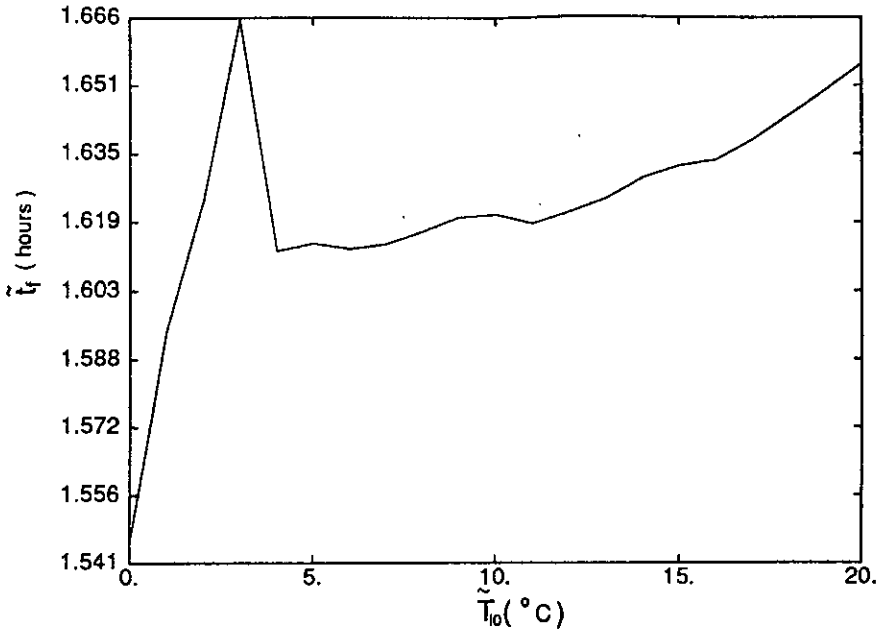

Figure 4.31: Plot of freezing time $\tilde{t}_f$ as a function of the initial temperature $\tilde{T}_{l0}$ for a square region of non-dimensional side length 2.0. The boundary temperature is $T_{sb} = -2.0$ $(-20\,^{\circ}C)$ and the non-dimensional parameters for water are given in table 4.2

$20\,^{\circ}C$, in order to determine the effect convection has on the freezing time. The computational region was a square of non-dimensional side length 2.0 which was then reduced by symmetry to a rectangle of length 1.0 in the x direction and height 2.0 in the z direction (see sub-section 4.1.2). The boundary condition was taken to be $T_{sb} = -2.0$ $(-20\,^{\circ}C)$ and the initial vorticity was taken as $\omega_0 = 5.0 \times 10^{-3}$. The region was discretised with spatial steps for the solid and liquid regions of $\Delta s_s = 0.05$ and $\Delta s_l = 1/60$ respectively. The time steps in the solid and liquid phases were $\Delta t_s = 15.0$ and $\Delta t_l = 7.5 \times 10^{-3}$ respectively. The dimensional parameters for water are shown in Appendix A, table A.1 and the non-dimensional parameters are given in table 4.2.

Figure 4.31 shows the variation of the freezing time $\tilde{t}_f$ (in hours) as a function of the initial temperature $\tilde{T}_{l0}$ (in $^{\circ}C$). For $\tilde{T}_{l0}$ between $0\,^{\circ}C$ and $3\,^{\circ}C$ we see a steady increase in the freezing time $\tilde{t}_f$ as in figure 3.12, which shows the freezing time when fluid motion is neglected. This is because for initial temperatures in the range $0\,^{\circ}C$ to $3\,^{\circ}C$ there is little motion of the freezing fluid. Above $T_{l0} = 0.3$ $(3\,^{\circ}C)$ fluid motion effects are starting to have a stronger influence on the freezing time $\tilde{t}_f$. This was demonstrated in previous simulations for $\tilde{T}_{l0} = 4\,^{\circ}C$, $\tilde{T}_{l0} = 7.5\,^{\circ}C$ and $\tilde{T}_{l0} = 15\,^{\circ}C$ (see figures 4.10 to 4.30). For initial temperatures in the range $4\,^{\circ}C$ to $20\,^{\circ}C$ the freezing time shows an incensing trend with initial temperature. At the low temperature end of this interval there is a considerable drop in the freezing time from that of the initial interval from $0\,^{\circ}C$ to $3\,^{\circ}C$. This is

associated with the convection starting to make a sizeable difference to the front motion and because of this the liquid phase is starting to lose heat more quickly, leading to the decrease in freezing time shown in figure 4.31. The bumpy nature of figure 4.31 for initial temperatures above $\tilde{T}_{l0} = 3\,^{\circ}C$ is associated with the numerical difficulties in exactly locating the final front position before freezing. Close to the centre of the region the movement of the phase change front between each time step is small. The numerical difficulties in dealing with the front just before complete freezing are resolved by stopping the numerical integration when the phase change front is a distance ε from the centre of the region. The time to completely freeze is then estimated by extrapolating from the previous two front positions to the centre of the region. The freezing time is therefore calculated by adding this extrapolated time to obtain the final estimate of the freezing time $\tilde{t}_f$ for the region. The size of the small bumps in figure 4.31 are of the order of the error of this extrapolation.

The mean ice crystal sizes that are obtained from the complete freezing of the region for initial temperatures in the range $0\,^{\circ}C \leq \tilde{T}_{l0} \leq 20\,^{\circ}C$ are presented in the next sub-section.

4.3.1 Crystal Formation

The numerical method (for two-phase Stefan problems with convection in the liquid phase) given in the previous sections 4.2 to 4.2.3 can be used with a simple model of crystal growth to predict the sizes of crystals formed when a liquid freezes. The model employed here is the same as that described in section 3.5. In modelling terms the inclusion of convection simply introduces new scalings into the crystal growth model.

To recap, if the growth of an individual crystal is assumed to be radially symmetric, then the size of the crystal formed when a liquid freezes is given in dimensional units by

$$\tilde{S} = \sqrt{\frac{2\,\tilde{K}_l\,(\tilde{T}_{lf} - \tilde{T}_\infty)\,\tilde{t}}{\tilde{\rho}\,\tilde{L}}}\,; \tag{4.65}$$

see Frank [27] and Coriell & McFadden [15]. Here $\tilde{K}_l$ is the thermal conductivity of the liquid, $\tilde{L}$ is the latent heat, $\tilde{T}_{lf}$ is the freezing temperature of the liquid and $\tilde{T}_\infty$ is the temperature far ahead of the growing crystal. This expression applies only to a single crystal which has been growing for a time $\tilde{t}$. To apply it to the freezing of a region, as in the numerical solutions of the last section, this expression must be applied to each individual crystal that is formed i.e. at each point of the region. Each crystal at a given point is then formed when the moving phase change front passes through that point.

The strategy adopted here is to replace the time $\tilde{t}$ in the size expression by the velocity of the phase change front. This is in agreement with models of microstructure formation, for which the crystal size is primarily determined by the front velocity [44, 45]. The time and temperature scales have been non-dimensionalised using

$$t = \sqrt{\frac{\tilde{g}\,\tilde{\alpha}_q \tilde{T}_t^2}{\tilde{d}}}\,\tilde{t} = \frac{\tilde{t}}{\tilde{\theta}_q} \quad \text{and} \quad T_l = \frac{\tilde{T}_l - \tilde{T}_{lf}}{\tilde{T}_t}, \tag{4.66}$$

where $\tilde{g}$ is the gravitational acceleration, $\tilde{\alpha}_q$ is the coefficient of thermal expansion, $\tilde{T}_t$ is a typical temperature of the liquid phase and $\tilde{d}$ is a typical length scale for the region. Non-dimensionalising the time and temperature scales allows the values calculated by the numerical procedure of the previous section to be used directly without having to transform them to dimensional form.

Expressing quantities in non-dimensional variables using (4.66) and replacing the time t by the front velocity V in the crystal size expression (4.65), (see section 3.5), the alternative crystal growth expression is given in dimensional variables as

$$\tilde{S} = \frac{\gamma}{V}\sqrt{\frac{\tilde{K}_l\,\tilde{\theta}_q\,\tilde{T}_t\,(T_{lf} - T_\infty)}{2\,\tilde{\rho}\,\tilde{L}}}. \tag{4.67}$$

Here γ is the root of the transcendental equation (2.10), V is the non-dimensional velocity of the phase change front, T_{lf} is the non-dimensional fusion temperature of the liquid and T_∞ is the non-dimensional temperature far ahead of the growing crystal. It is this form of the crystal size expression that will be used in the present work to calculate the sizes of crystals formed from the freezing of a two-dimensional region.

The crystal sizes are then calculated in the same manner as that described in section 3.5, except that the numerical procedure used to solve the governing equations will be that previously described for two-phase Stefan problems with convection.

Figure 4.32 shows the mean crystal size $\bar{S}$ (in mm) as a function of the initial condition $\tilde{T}_{l0}$ (in $^\circ C$) with and without the inclusion of fluid motion ahead of the phase change front. The solid line shows the crystal size when convection in the liquid phase is included and is obtained using the numerical techniques given in this chapter. The dashed line is for the same example when no convection effects are included and is obtained using the double boundary integral method (BIM) of Chapter 3. The non-dimensional parameters for water in the BIM example are $D_s = 8.9649, D_l = 1.0, S_t = 3.5732$ and $K = 4.1516$ for $\tilde{T}_t = 20\,^\circ C$ with boundary condition $T_{sb} = -1.0$ $(-20\,^\circ C)$. The non-dimensional parameters for

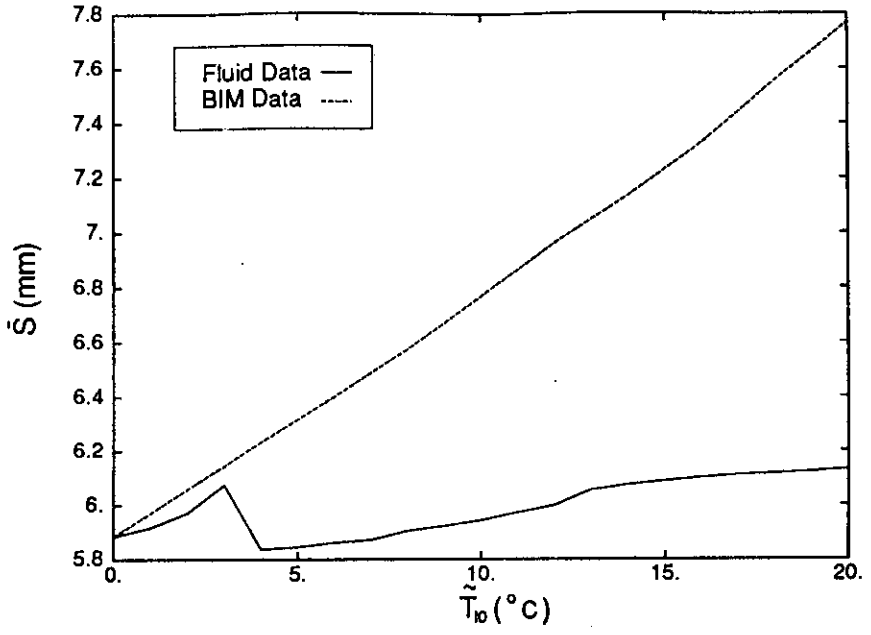

Figure 4.32: Plot of the mean crystal size $\bar{S}$ as a function of the initial temperature $\tilde{T}_{l0}$ for the freezing of water. For a square region of non-dimensional side length 2.0 with boundary temperature $\tilde{T}_{sb} = -20\,°C$

the fluid data are given in table 4.2 for $\tilde{T}_t = 10\,°C$ with boundary condition $T_{sb} = -2.0$ $(-20\,°C)$. The length scale for both these examples is $\tilde{d} = 5.0\,cm$.

In figure 4.32 the boundary integral data shows a strong positive linear relationship between mean crystal size $\bar{S}$ and initial condition $\tilde{T}_{l0}$ with ice crystal sizes in the range $5.88\,\text{mm} \leq \bar{S} \leq 7.77\,\text{mm}$. A plot of the freezing time t_f as a function of the mean crystal size $\bar{S}$ is shown in figure 3.13 for the same parameter values. In that case, the mean crystal size increases almost linearly with t_f except near $t_f = 0.34$ (corresponding to an initial condition of $\tilde{T}_{l0} = 20\,°C$) where there is a sharp increase in the size; see section 3.5. Including convection in the liquid phase clearly reduces the sizes of the ice crystals formed. When convection is included the mean ice crystal sizes lie in the range $5.88\,\text{mm} \leq \bar{S} \leq 6.13\,\text{mm}$. Initially there is a steady increase in the crystal size when $\tilde{T}_{l0}$ is between $0\,°C$ and $3\,°C$ with a drop between $3\,°C$ and $4\,°C$. Thereafter however, the crystal size shows a steady increase up to an initial temperature of $20\,°C$. This is because for initial temperatures in the range $0\,°C$ to $3\,°C$ there is little motion in the freezing fluid. Above $4\,°C$ however, the convection effects are starting to make a difference to the front motion and hence to the overall mean crystal sizes. The liquid phase is starting to lose heat more quickly due to convection, leading to lower freezing times (see figure 4.31). Consequently the crystal sizes are in turn reduced.

As the phase change front moves into the region it slows down and moves very slowly when it is near the centre of the region. Hence the crystal sizes are

relatively small near the boundary of the region and relatively large near the centre of the region (see figures 4.33 and 4.34). However as the larger crystal sizes are in a small sub-section of the region near its centre, they will not have a large effect on the average crystal size.

A plot of the dimensional crystal size $\tilde{S}$ (mm) over the region is shown in figures 4.33 and 4.34. The non-dimensional parameters for water used in this example are given in table 4.2 and the crystal sizes have been calculated with fluid motion ahead of the phase change front. The boundary condition was taken to be $\tilde{T}_{sb} = -20\,^{o}C$ and the initial condition was $\tilde{T}_{l0} = 15\,^{o}C$. The crystal size $\tilde{S}$ was evaluated using as before equation (4.67). However rather than applying the formula over each mesh box (see section 3.5) the crystal size was simply calculated at each point of the computational mesh.

It is expected that the largest crystals will be formed in those areas of the region where the phase change front is moving slowest. Conversely the smallest crystals will be located where the phase change front is moving fastest. It can be seen from figure 4.34 that initially the largest crystals are located at the sides of the region and the smallest crystals at the corners. This distribution of crystal size makes physical sense since initially the corners of the phase change front are moving faster than the sides, resulting in the humped distribution of crystal sizes shown in figure 4.34. As the region continues to freeze the phase change front becomes circular, which results in more uniform freezing rates and consequently crystal sizes in conformity with the results shown in figures 4.33 and 4.34.

The rippling effects that can be seen in both figure 4.33 and 4.34 are caused by numerical errors, these errors being of the order of the mesh box size used in the boundary integral solution.

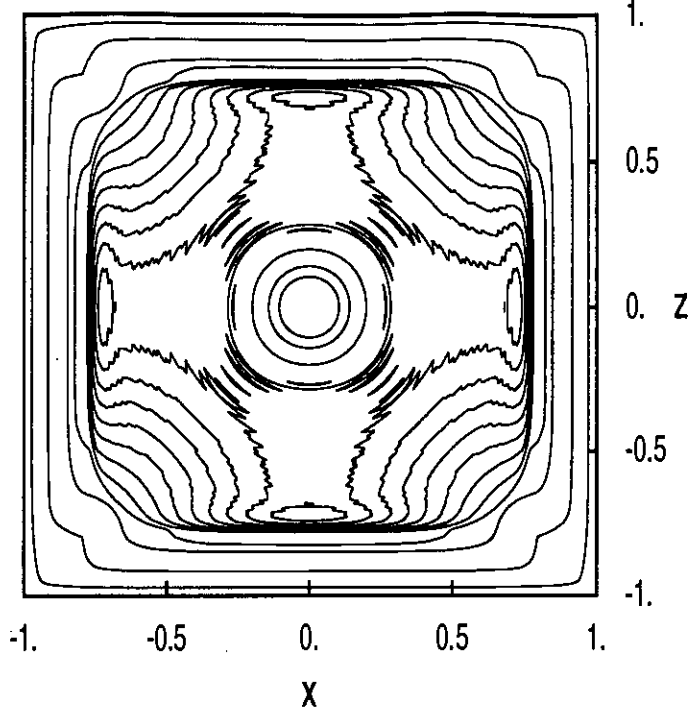

Figure 4.33: Contour plot of the crystal size $\tilde{S}$ (mm) in a square region of non-dimensional side length 2.0 for the freezing of water. Contour lines begin at 0.5 and finish at 11.0 with an increment of 1.0 between each contour. The initial temperature is $\tilde{T}_{l0} = 15\,^{o}C$ and the boundary temperature is $\tilde{T}_{sb} = -20\,^{o}C$

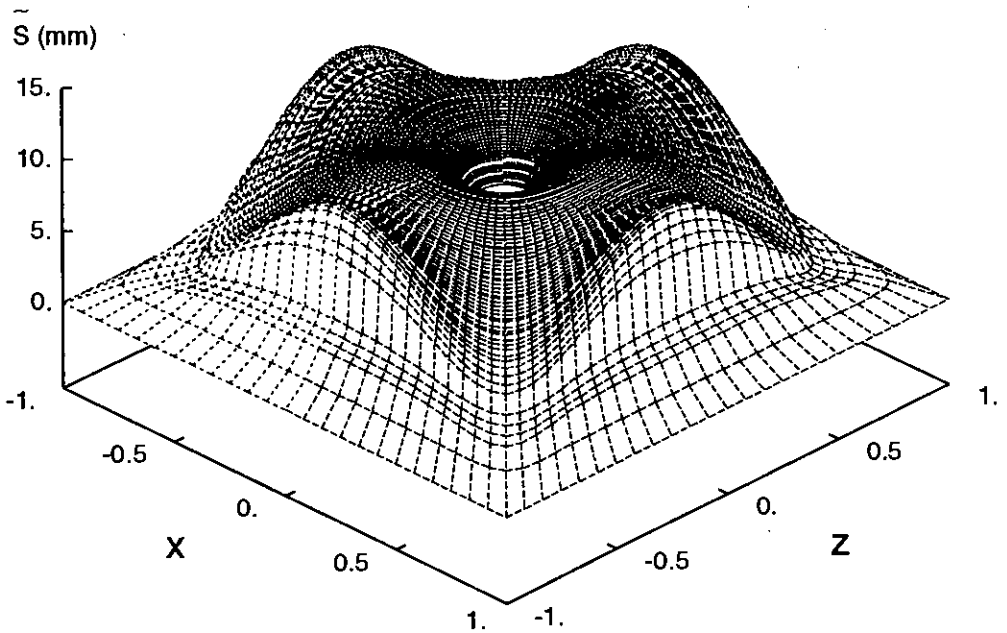

Figure 4.34: Surface plot of the crystal sizes $\tilde{S}$ (mm) in a square region of non-dimensional side length 2.0 for the freezing of water. The initial temperature is $\tilde{T}_{l0} = 15\,^{o}C$ and the boundary temperature is $\tilde{T}_{sb} = -20\,^{o}C$

Chapter 5

Conclusions and Further Work

5.1 Double Boundary Integral Method

It has been shown in Chapter 3 that a boundary integral method can be used to find a numerical solution of the Stefan problem when heat flow both ahead of and behind the phase change front is taken into account. This forms an extension of the work of Coleman [12] which considered heat flow behind the phase change front only. It was found that this boundary integral method formulation of the Stefan problem has the advantages of (i) being a fast numerical method which yields accurate solutions and (ii) that it can easily incorporate non-rectangular boundaries. Furthermore when parameter values appropriate for water were used, it was found that the standard method for determining the front position, based on Newton's method, was unstable and so a new method for determining the front position, based on the bisection method, was developed.

Points (i) and (ii) in the previous paragraph are in some sense related. One of the reasons that the boundary integral method is fast computationally is that the dimension of the integral equations to be solved is one dimension less than the dimension of the region itself. For example, in Chapter 3 the phase change problems considered were two-dimensional, but the resulting integral equations were solved as two one-dimensional problems on two curves; namely the fixed boundary and the phase change front. Upon assuming appropriate boundary conditions on these curves, the equations can be discretised on a mesh that is one dimension less than that of the region itself. This results not only in a reduction in computational effort but since the boundaries can be discretised in a simple and straight forward manner, the method can accommodate complex geometries with relative ease.

Another feature of the boundary integral method is that it provides a great saving in computation time and computer storage due to the structure of the linear system for the unknown boundary data on the fixed boundary B_f (see

section 3.3). The block structure of the coefficient matrix in this case dictates that at each time step it is the same set of block elements in the coefficient matrix that requires inversion. Consequently only one matrix inversion is carried out per solution simulation. Furthermore the coefficient matrix has the same set of block matrices repeated in each block column and so the computer storage requirements are greatly reduced by requiring only the first column of blocks of the coefficient matrix to be stored. The savings made in solving the linear system in this case are a consequence of the presence of a fixed boundary for the region.

The boundary integral method does however have the drawback that it can only be applied to well-posed Stefan problems and not to heat problems for which there is supercooling. In the following sub-section we briefly outline what is meant by supercooled problems and the implications of this for numerical solutions.

5.1.1 Mushy Regions

There is a class of heat conduction problems which the heat needed to produce melting comes from heat sources distributed throughout the material rather than from heat input from the boundaries of the region. An example is the Joule heating associated with electric currents within a conduction. In such cases the melting does not need to occur at an interface as in the classical Stefan problem. Instead an extended region can occur which is at the melting temperature of the material and in which the solid and liquid phases both coexist. This region is sometimes refered to as a mushy zone. A further example for which a mushy region occurs is that of alloy solidification in which case the change of phase occurs over a range of temperatures, leading to the formation of a mushy region with coexisting phases. Typically the formation of these regions is also associated with the superheating or supercooling of a particular part of the phase. A supercooled fluid is one which still exists in its liquid state when its temperature is lowered below its freezing temperature e.g. water that exists as a liquid below $0\,^{\circ}C$. Conversely a superheated fluid exists in its solid state when it is above its melting temperature. Hence for well-posed Stefan problems there exists distinct solid and liquid phases separated by a distinct front which persists until the phase change is complete.

For supercooled (or superheated) problems however the phase change region is less distinct and can exist as a mixture of solid and liquid phases and is bounded by a not necessarily smooth or continuous interface. A review of the modelling of mushy zones is given in the paper by Crowley and Ockendon [14] and in the book by Elliott and Ockendon [23].

The classical Stefan problem model in one dimension given in Chapter 2, and

in two dimensions, given in Chapter 3, are incapable of including regions of mixed phases [14]. Inherent in the formulation of these models is the assumption that the material to be frozen is pure and that it can exist in either the solid or liquid phase, but not both at the same temperature. In other words once the material is above the freezing temperature, the liquid phase is obtained, and below, the solid phase is obtained. Should the boundary integral method of Chapter 3 be applied to problems that are capable, of yielding a mushy zone some additional modelling and numerical formulation would be required to deal with the formation of such a region.

5.1.2 Crystal Growth Modelling

Using a simple model for the growth of a crystal from a freezing liquid, the numerical method of Chapter 3 was extended to predict the sizes of the crystals in the crystalline microstructure formed when a liquid region freezes. The predictions of this model were found to be in qualitative agreement with experimental results. While this method for predicting crystal sizes was developed in the context of water, it can easily be applied to other areas in which the prediction of crystal sizes is important, for example the growing of silicon crystals for the computer industry. The crystal growth model used was basic. While there exists improved models for crystal growth (see [15, 25, 27]), it is not clear that the increased complexity resulting from them is justified by the crude experimental results for crystal sizes formed from a freezing liquid.

5.2 Inclusion of Fluid Motion

In Chapter 4 was shown that the boundary integral method and the equations of fluid motion can be combined to obtain the numerical solution of two-phase Stefan problems with fluid motion in the liquid phase. This further extends the work of Chapter 3 and that of Coleman [12] for which no fluid motion effects were included. It was found that inclusion of the fluid motion results in a reduction in freezing time and, furthermore, the crystal growth model predicted a reduction in crystal sizes from that of similar examples without fluid motion in Chapter 3. The sizes of the crystals are then in accord with experimental data [37]. The bisection method for determining the front position employed in the numerical procedure of Chapter 3 was again retained and employed when the standard method, based on Newton's method, was found to be unstable.

The numerical method for Stefan problems with fluid motion given in Chapter 4 was found to be accurate, but computationally quite slow for the fine meshes re-

quired for proper inclusion of the boundary layer. The method still exploited some of the computationally useful features of the boundary integral method; namely the reduced dimensionality of the integral equations and the block coefficient matrix structure of their numerical approximation. The reduction in computation time is due to these features is outweighed by the increase in computation time due to the fine mesh required to adequately approximate the boundary layer.

In order to capture the boundary layers for the problems considered in Chapter 4 the minimum number of mesh points is of the order of $1/\sqrt{\nu_l}$, where ν_l is the non-dimensional kinematic viscosity. Choosing a uniform space step of an order required to capture the boundary layer leads to large systems of equations to be solved and long computation times. A non-uniform mesh which is fine near the boundaries to capture the boundary layer and course away form the boundaries would reduce system size and hence computation times, as explained in the next sub-section.

5.2.1 Meshing Strategy

In the numerical procedure of Chapter 4 for solving Stefan problems with fluid flow in the liquid phase the meshing strategy for the governing equations of fluid motion was found to be effective for the problems considered, but resulted in rather large computation times due to the large number of grid points. The mesh points were distributed evenly throughout the liquid region, except near the phase change front where, if necessary, the mesh was extended to include points on the phase change front itself (see section 4.2). Close to the phase change front the density of the mesh points was required to be high so as to capture the dynamics of the boundary layers occurring there. Therefore the equally spaced distribution of mesh points throughout the region resulted in a large number of grid points. In the interior of the liquid region however, away from the phase change front, the density of mesh points need not be as great and a courser mesh would suffice. Figure 5.1 shows a possible boundary layer fitted distribution of mesh points for the liquid region in the first quadrant of the (x, z) plane. In this case denser bands of mesh points can be seen at a distance δ from the phase change front, where δ is a measure of the boundary layer thickness, with the courser mesh occurring in the interior of the liquid region. The grid close to the phase change front in this case is known as a boundary fitted mesh [49]. In order to obtained this mesh structure near the phase change front a regular two-dimensional mesh was deformed in some way such that the mesh cells conform with the shape of the front. The obvious advantage of this is that the mesh will conform with the geometry of the phase change front more accurately and, furthermore, any boundary data there

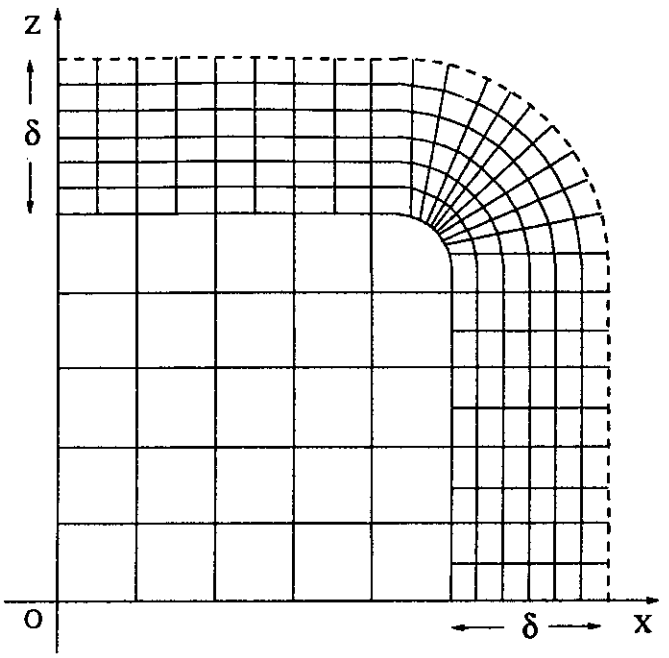

Figure 5.1: Plot of boundary fitted mesh in first quadrant of the (x, z) plane ahead of the phase change front at time $t > 0$

will be better approximated. Some interpolation of the quantities T_l, ω and ψ between the boundary layer and interior mesh will be required [48].

If the boundary fitted mesh strategy outlined above is employed the mesh will no longer have to be extended to include points on the phase change front. However since there is a non-uniform mesh in the x direction (see section 4.2) the Taylor series expansion, given in section 4.2, of

$$f(x - \Delta x, z) \text{ now becomes } f(x - \varepsilon_1 \Delta x, z)$$

where $\varepsilon_1 \in [0, 1)$. This results in different forms for the finite difference approximations of the equations of fluid motion. Otherwise the numerical procedure will be the same as that given in Chapter 4 for two phase Stefan problems with fluid motion.

As an alternative to applying a remeshing procedure to the fluid motion equations, a transformation of the liquid region to a fixed rectangular domain could be employed. For instance if we consider the liquid region in the (x, z) plane the Schwarz-Christoffel transformation (see [10]) allows a n sided polygon, namely the phase change front, to be mapped to the real axis of the complex plane, whilst its interior is mapped to the upper half plane. The upper half plane can be mapped to a rectangular domain using a standard conformal mapping. The equations of fluid motion could then be solved in this rectangular domain, with the solution being returned to the physical domain by an inverse mapping. However as a

new conformal mapping needs to be determined at each time step, this mapping technique for solving the fluid equations on a simpler domain may be less efficient than the boundary fitted mesh technique.

5.2.2 Parallelisation

The existing computer programme for solving two-phase Stefan problems with fluid motion was written in serial code using the Fortran 77 language. The programme was found to be effective for the problems considered in Chapter 4 but the computation time was quite long for fine meshes. A further possibility for increasing the efficiency of the numerical procedure and for decreasing the computation time is to parallelise the computer programme. This parallel code could be written using High Performance Fortran [34] or F^{--}, a parallel extension of Fortran (see [41]). One obvious area in which parallelisation could be used is to separate out the fluid motion programme and the boundary integral programme, thereby allowing each of them to be executed freely with as few communications between them as possible. Indeed, only the normal temperature derivatives at the phase change front need be communicated. Within each of these two programmes there are further areas where parallelisation may be applicable e.g. LU decomposition and Jacobi iteration. In each of these numerical routines, particularly those that form part of the fluid motion programme, the routines are accessed repeatedly at each time step. Therefore any resulting speed up in calculation time would have a significant effect on the overall computation time for a freezing simulation.

Appendix A

Dimensional Parameters for Water

Quantity	Symbol	Value	Units
Specific heat (liquid)	$\tilde{c}_l$	2106.0	$J\,kg^{-1}\,{}^{o}K^{-1}$]
Specific heat (solid)	$\tilde{c}_s$	4174.0	$J\,kg^{-1}\,{}^{o}K^{-1}$
Length scale (a)	$\tilde{d}_a$	0.050	m
Length scale (b)	$\tilde{d}_b$	0.025	m
Thermal diffusivity (liquid)	$\tilde{D}_l$	1.3299×10^{-5}	$m^2\,s^{-1}$
Thermal diffusivity (solid)	$\tilde{D}_s$	1.1923×10^{-4}	$m^2\,s^{-1}$
Gravitational acceleration	$\tilde{g}$	9.81	$m\,s^{-2}$
Thermal conductivity (liquid)	$\tilde{K}_l$	0.554	$W\,m^{-1}\,{}^{o}K^{-1}$
Thermal conductivity (solid)	$\tilde{K}_s$	2.30	$W\,m^{-1}\,{}^{o}K^{-1}$
Latent heat	$\tilde{L}$	3.25×10^5	$J\,kg^{-1}$
Freezing temperature	$\tilde{T}_{lf}$	0.0	${}^{o}C$
Temperature scale	$\tilde{T}_t$	10.0	${}^{o}C$
Thermal expansion coefficient	$\tilde{\alpha}_l$	1.177202×10^{-4}	${}^{o}K^{-1}$
Thermal expansion coefficient	$\tilde{\alpha}_q$	6.296770×10^{-6}	${}^{o}K^{-2}$
Density (solid & liquid)	$\tilde{\rho}$	916.0	$kg\,m^{-3}$
Kinematic viscosity	$\tilde{\nu}_l$	10^{-6}	$m^2\,s^{-1}$

Table A.1: Values of the dimensional parameters for water

Bibliography

[1] Abramowitz, M. and Stegun, I., *Handbook of Mathematical Functions*, Dover Publications Inc., New York, USA, 1972.

[2] Acheson, D.J., *Elementary Fluid Dynamics*, Oxford Applied Mathematics and Computing Science Series, Clarendon Press, Oxford, UK, 1994.

[3] Batchelor, G.K., *An Introduction to Fluid Dynamics*, Cambridge University Press, Cambridge, UK, 1967.

[4] Bénard, H., "Les tourbillons cellulaires dans une nappe liquide," *Revue Gén. Sci. Pur. Appl.*, 1900, **11**, pp. 1261–1271 and pp. 1309–1328.

[5] Brent, A.D., Voller, V.R. and Reid, K.J., "Enthalpy-porosity technique for modeling convection-diffusion phase change: Application to the melting of a pure metal," *Num. Heat Trans.*, 1988, **13**, pp.297–318.

[6] Burden, R.L., Faires, J.D. and Reynolds, A.C., *Numerical Analysis*, 2nd Ed. Prindle, Weber & Schmidt Publishers, Boston, Massachusetts, USA, 1981.

[7] Carslaw, H.S. and Jaeger, J.C., *Conduction of Heat in Solids*, 2nd Ed. Clarendon Press, Oxford, UK, 1959.

[8] Chang, C.J. and Brown, R.A., "Natural convection in steady solidification: finite element analysis of a two-phase Rayleigh-Bénard problem," *J. Comp. Phys.*, 1984, **53**, pp. 1–27.

[9] Chow, P. and Cross, M., "An enthalpy control-volume-unstructured-mesh (CV-UM) algorithm for solidification by conduction only," *Int. J. Num. Method. Engin.*, 1992, **35**, pp. 1849–1870.

[10] Churchill, R.V. and Brown, J.W., *Complex Variables and Applications*, 5th Ed. McGraw-Hill Co., Singapore, 1990.

[11] Claire, F., Kennison, D. and Lackman, B., *N.C.A.R. Graphics: User's Guide, Version 2.0*, Scientific Computing Division, National Center for Atmospheric Research, Boulder, Colorado, USA, 1987.

[12] Coleman, C.J., "A boundary integral formulation of the Stefan problem," *Appl. Math. Modelling,* 1986, **10**, pp. 445–449.

[13] Coleman, C.J., "A boundary integral approach to the solidification of dilute alloys," *Int. J. Heat Mass Transfer,* 1987, **30**, pp. 1727–1732.

[14] Crowley, A.B. and Ockendon, J.R., "Modelling mushy regions," *Applied Scientific Research,* 1987, **44**, pp. 1–7.

[15] Coriell, S.R. and McFadden, G.B., "Morphological Stability," pp. 785–857, in *Handbook of Crystal Growth 1b, Fundamentals, Part B: Transport and Stability,* D.T.J. Hurle Ed., North-Holland, 1993.

[16] Crank, J., *Free and Moving Boundary Problems*, Clarendon Press, Oxford, UK, 1984.

[17] *CRC Handbook of Chemistry and Physics*, 74th Edition, David R. Lide, editor in chief, Chemical Rubber Publishing Company, Boca Raton, Florida, USA, 1993.

[18] Dahlquist, G., Björk, Å. and Anderson, N., *Numerical Methods*, Prentice-Hall Inc., New Jersey, USA, 1974.

[19] Dantzig, J.A., "Modelling liquid-solid phase changes with melt convection," *Int. J. Num. Method. Engin.,* 1989, **28**, pp. 1769–1785.

[20] de Vahl Davis, G., "Finite difference methods for natural and mixed convections in enclosures," pp. 101–109, in *Vol. 1, Proceedings 8th Int. Conf. Heat Trans.,* San Francisco, USA, 1986.

[21] de Vahl Davis, G., Leonardi, E., Wong, P.H. and Yeoh, G.H., "Natural convection in a solidifying liquid," *Num. Meth. Thermal Problems,* 1986, **6**, pp. 410–420.

[22] Drazin, P.G. and Reid, W.H., *Hydrodynamic Stability*, Cambridge University Press, London, UK, 1981.

[23] Elliott, C.M. and Ockendon, J.R., *Weak and variational methods for moving boundary problems, Res. Notes Math.,* Pitman Advanced Publishing Program, **59**, 1982.

[24] Finlayson, B.A., *Numerical Methods for Problems with Moving Fronts*, Ravenna Park Publishing, Inc., Seattle, Washington, U.S.A., 1992.

[25] Fletcher, N.H., *The Chemical Physics of Ice*, Cambridge University Press, London, UK, 1970.

[26] Fox, L., "The Stefan Problem: moving boundaries in parabolic equations" in *A Survey of Numerical Methods for Partial Differential Equations* (eds. Gladwell, I. and Wait, R.), Clarendon Press, Oxford, 1979.

[27] Frank, F.C., "Radially symmetric phase growth controlled by diffusion," *Proc. Roy. Soc. Lond. A,* 1950, **201**, pp. 586–599.

[28] Galloway, S.J. and Smyth, N.F., "A numerical method for predicting crystal micro–structure," *Appl. Math. Modelling,* 1997, **21**, pp. 569–578.

[29] Henshaw, W.D., Smyth, N.F. and Schwendeman, D.W., "Numerical shock propagation using geometrical shock dynamics," *J. Fluid Mech.,* 1986, **171**, pp. 519–545.

[30] Hill, J.M. and Dewynne, J.N., *Heat Conduction*, Blackwell Scientific Publications, Oxford, UK, 1987.

[31] Hill, J.M., *One-dimensional Stefan Problems: An Introduction*, Longman Scientific & Technical, Harlow, UK, 1987.

[32] Hirasaki, G.J. and Hellums, J.D., "A general formulation of the boundary conditions on the vector potential in three-dimensional hydrodynamics," *Q. Appl. Math.,* 1967, **26**, pp. 331-342.

[33] Jackson, C.P. and Winters, K.H., "A finite-element study of the Bénard problem using parameter stepping and bifurcation search," Int. J. Num. Meth. Fluids, 1984, **4**, pp. 127–145.

[34] Koebel, C.H., Loveman, D.B., Schreiber, R.S., Steele, G.L. and Zoesl, M.E., *The High Performance Fortran Handbook (Scientific and Engineering Computation)*, MIT Press, Cambridge, Massachusetts, USA, 1994.

[35] Langer, J.S., "Instabilities and pattern formation in crystal growth," *Rev. Mod. Phys.,* 1980, **52(1)**, pp. 1–28.

[36] Lynch, D.R., "Unified approach to simulation on deforming elements with application to phase change problems," *J. Comp. Phys.,* 1982, **47**, pp. 387–411.

[37] Miyawaki, O., Abe, T. and Yano, T., "Freezing and ice structure formed in protein gels," *Biosci. Biotech. Biochem.,* 1992, **56(6)**, pp. 953–957.

[38] Moore, D.R., Peckover, R.S. and Weiss, N.O., "Difference methods for time-dependent two-dimensional convection," *Computer Physics Communications,* 1973, **6**, pp. 198–220.

[39] Moore, D.R. and Weiss, N.O., "Two-dimensional Rayleigh-Bénard convection," *J. Fluid Mech.,* 1973, **58**, pp. 289–312.

[40] Moore, D.R. and Weiss, N.O., "Nonlinear penetrative convection," *J. Fluid Mech.,* 1973, **61**, pp. 553–581.

[41] Numrich, R.W. and Steidel, J.L., "F^{--}: A simple parallel extension to Fortran 90," *SIAM News,* 1997, **30(7)**, pp. 1,6–8.

[42] Oosthuizen, P.H. and Paul, J.T., "A numerical study of the steady state freezing of water in an open rectangular cavity," *Int. J. Meth. Heat Fluid Flow.,* 1996, **6(5)**, pp. 3–16.

[43] Ostrach, S., "Natural convection in enclosures," *Trans. ASME J. Heat Transfer,* 1988, **110**, pp. 1175–1190.

[44] Rappaz, M., "Modelling of microstructure formation in solidification processes," *Int. Materials Rev.,* 1989, **34(3)**, pp. 93–123.

[45] Rappaz, M., Carrupt, B., Zimmermann, M. and Kurz, W., "Numerical-Simulation of eutectic solidification in the laser treatment of materials," *Helv. Phys. Acta,* 1987, **60**, pp. 924–936.

[46] Rayleigh, Lord, "On convection currents in a horizontal layer of fluid, when the higher temperature is on the underside," *Phil. Mag.,* 1916, **32 (6)**, pp. 529–546.

[47] Roberts, K.V. and Weiss, N.O., "Convective difference schemes," *Math. Comp.,* 1966, **20**, pp. 272–299.

[48] Roos, H.-G., Stynes, M. and Tobiska, L., *Numerical Methods for Singularly Perturbed Differential Equations*, Springer-Verlag, New York, USA, 1996.

[49] Shyy, W., Udaykumar, H.S., Rao, M.M. and Smith, R.W., *Computational Fluid Dynamics with Moving Boundaries*, Series in Computational and Physical Processes in Mechanics and Thermal Sciences, Taylor & Francis Ltd., Washington D.C., USA, 1996.

[50] Sienko, M.J. and Plane, R.A., *Chemical Principles and Properties*, International Student Edition, 2nd Ed, McGraw-Hill Kogakusha Ltd., London, UK, 1974.

[51] Smith, G.D., *Numerical Solution of Partial Differential Equations: Finite Difference Methods*, Oxford Applied Mathematics and Computing Science Series, Clarendon Press, Oxford, UK, 1978.

[52] Stefan, J., "Über einige probleme der theorie der wärmeleitung," S. -B. *Akad. Math. Natur,* 1898, **98**, pp. 473–484.

[53] Van Dyke, M., *An Album of Fluid Motion*, Parabolic Press, Stanford, California, USA, 1982.

[54] Voller, V.R. and Cross, M., "Accurate solutions of moving boundary problems using the enthalpy method," *Int. J. Heat Mass Transfer,* 1981, **24**, pp. 545–556.

[55] Voller, V.R., Swaminathan, C.R. and Thomas, B.G., "Fixed grid techniques for phase change problems: a review," *Int. J. Num. Method. Engin.,* 1990, **30**, pp. 875–898.

[56] Woods, L.C., "A note on the numerical solution of fourth order differential equations," *Aero. Quart.,* 1954, **5**, pp. 176–184.

[57] Yeoh, G.H., Behnia, M., de Vahl Davis, G. and Leonardi, E., "A numerical study of three-dimensional natural convection during freezing of water," *Int. J. Num. Method. Engin.,* 1990, **30**, pp. 899–914.

[58] Yih, C.-S., *Fluid Mechanics*, West River Press, Michigan, USA, 1979.

Gallaway, S.J.
Ph.D 1998

UNIVERSITY OF EDINBURGH THESIS

Author (surname, initials): Galloway, S.J. Degree: Ph.D Year: 1998

This thesis is an unpublished typescript and the copyright is held by the author. *All persons consulting this thesis, or having copies made, must sign the Copyright Declaration below.*

Copying regulations:

(1) This thesis may be copied in whole or in part for the use of individuals and for libraries wishing to add this thesis to their stock. *Copying must be done by Edinburgh University Library.*

(2) This thesis must not be copied, either in whole or in part, without the applicant obtaining the author's written permission. *If permission is granted, then copying must be done by Edinburgh University Library.* (The bibliography/list of works consulted may be copied without the author's permission, provided the copying is done by Edinburgh University Library.)

(3) This thesis may be copied only in so far as the copying does not contravene the 1956 Copyright Act. *Copying must be done by Edinburgh University Library.*

Copyright Declaration: I undertake fully to observe the author's copyright in this thesis, not to publish the whole or any part of it without the author's written permission, and not to allow any other person to use any copy made for me.

Date	Name and Address (BLOCK CAPITALS)	Signature	Pages copied (if any)
2/11/00	JASON J BEECH-BRANDT JCMB, KB, ROOM 5603